Dept. of Math. University of Oslo
Mechanics and Applied Mathematics No. 1
ISSN 0809–4403 February 2008

Documentation of a global Boussinesq solver

G. Pedersen[1,2] & F. Løvholt[2,3]
[1] Department of Mathematics, University of Oslo, PO box 1053, 0316 Oslo, Norway
[2] International Centre for Geohazards
[3] Norwegian geotechnical institute

February 15, 2008

Abstract

This report is the documentation of a new model for large scale solution of the Boussinesq equations. The equations are briefly presented with emphasis on the inclusion of spherical coordinates and the Coriolis force. We have chosen to start with the standard Boussinesq formulation, but have modified it to achieve improved dispersion properties for moderately short waves. This formulation is put into the context of Boussinesq equations in general in an appendix. Describing first the discretization in detail, we then design higher order numerical differences, analyse dispersion, stability and the convergence rate of the iteration scheme used at each time step. The performance of the present model is also compared to state of the art models (FUNWAVE/COULWAVE).

A selection of tests are performed to validate the code and assess the applicability and accuracy of the method. The tests include eigenoscillations in basins, solitary wave propagation, comparison with pre-existing models, diffraction of incident solitary waves by a vertical cylinder and trans-Atlantic propagation of a hypothetical tsunami from the La Palma island. The latter case is pursued further in a companion paper. All tests indicate that the model is correctly coded, efficient and robust.

Contents

1 Introduction

Shallow water models dominate operational ocean and tsunami modeling. The equations are simple, well suited for explicit time stepping and special phenomena like bores and inundation may be included. For most aspects of tsunami modeling shallow water theory is probably the best option in view of efficiency, software implementation and performance combined. However, tsunamis from non-seismic sources, such as gravity mass flows, are often substantially influenced by dispersion. In particular may the accumulated effect of dispersion during long distance propagation be important. In addition, specific wave forms, such as undular bores, that sometimes evolves also for seismic tsunamis require a dispersive description. The more general dispersive equations, like those of Navier-Stokes and full potential theory, are still too demanding for large scale modeling of tsunamis or other oceanic waves. Hence, we are referred to dispersive long wave equations, such as the Boussinesq type equations.

The Boussinesq equations come in great diversity; the standard formulation, Serre's equation, Green-Nadgi and many more. Since the mid nineties Boussinesq equations with improved dispersion[1] properties [23] and full nonlinearity [6, 14, 21, 22] have been incorporated in general purpose models. Excellent examples are the FUNWAVE [15, 40] and COULWAVE [20] models that are freely available and widely used. These models are useful also for tsunami modeling, but they may be somewhat heavy for large scale computation. In addition their strength, the full non-linearity, is mainly useful in very shallow water. Here the waves rapidly break and it is doubtful that the Boussinesq models then are as good, or robust at least, as NLSW models with bore capturing facilities. The model presented in this report is not an general alternative to models such as FUNWAVE/COULWAVE, but a simpler one with emphasis on efficiency and only standard nonlinear terms. It is descending from other Boussinesq models employed from 1987 and forward [36, 26, 17, 3] to problems in hydrodynamic wave theory [39, 27, 29, 31] and recently also to wave propagation from an oceanic asteroid impact on the continental shelf [9]. The models were bases on velocities or velocity potential, with a preference for the latter due to efficiency. Like most other early Boussinesq solvers [37, 1, 47] only the standard types of dispersion and nonlinearity were included. The current revitalization of the dispersive modelling is motivated by a study of the trans-Atlantic propagation from the hypothetical La-Palma tsunami [42]. In such a case geographical coordinates and the Coriolis effects must the be included, while standard dispersion properties suffice. The latter is probably general for tsunamis; the key question is whether dispersion is important at all and not what kind of dispersion that is needed. Still, we will modify the standard Boussinesq equations to obtain improved dispersion, in a similar manner as [2]. Moreover, a fourth order representation of the leading order (LSW) terms will be invoked, in analogy with the FUNWAVE/COULWAVE model.

We prefer the standard, velocity based, Boussinesq formulations because

1. The standard equations are infallibly stable regarding depth gradients, unlike all other Boussinesq formulations that the present authors have investigated. See section 3.7 and the reference [41].

2. It is simple to discretize with staircase boundaries. Some other formulations, in particular those with potentials as primary unknowns, requires fictitious values at the boundary when discretized with a FDM technique. Naturally, sloping beaches or boundaries situated in

---

[1] This is overlooked by many researchers who are hung up on the notion "fully nonlinear". We believe that improved dispersion is at least as important (see appendix).

very shallow water cannot anyhow be included without special treatment. Still, we will show later that staircase boundaries may work well in linear applications, and even in nonlinear ones provided the boundary is situated in water of some depth.

3. A simple correction term [2], may be included as to yield the same favourable dispersion that has been found for the Nwogu formulation.
4. Even with the correction term, the standard model is somewhat simpler than Nwogu's model. In particular concerning the equation of continuity.
5. Boussinesq equations with potentials as primary unknowns are are applicable to non-rotational flow, which render them less useful for a number of applications.

Subsequently, the equations, the discretization an tests will be presented. In addition we attempt a thorough documentation also in terms of analysis of the discrete properties of the model. This includes

- Numerical dispersion relations and stability. Those are surprisingly often omitted, or incompletely discussed, even in articles on wave modeling as such.
- Discussion of accuracy, also in view of correct representation of weakly dispersive effects.
- Derivation of numerical correction terms and their properties.
- Convergence and stability of iteration methods for the coupled equations sets at each time step.
- Eigenoscillations in rectangular basins. Numerical dispersion relations then provides an exact numerical solution for validation of the code.

2 Formulation

2.1 Transformation

In our equations we include the Coriolis effect and the modification on arc lengths by the curvature of the Earth. On the other hand, the deformation of the geoid and change of gravity as well as centripetal accelerations are left out. In addition also some minor corrections to the convective acceleration are neglected. Latitude and longitude, in radians, are denoted by ϕ and ψ respectively and the radii of the Earth is R.

The key points in the transformation of the improved standard Boussinesq equations, (83) and (91), are the geographical equivalents of a few differential operators. The gradient is

$$\nabla = \frac{1}{Rc_\phi}\vec{\imath}_\psi\frac{\partial}{\partial\psi} + \frac{1}{R}\frac{\partial}{\partial\phi}, \tag{1}$$

where $c_\phi = \cos\phi$ and $\vec{\imath}_\psi$, $\vec{\imath}_\phi$ are the unit tangent vectors in longitudinal and lateral direction, respectively. Letting $\vec{v} = u\vec{\imath}_\psi + v\vec{\imath}_\phi$ be the velocity, or another vector field in geographical coordinates, the divergence becomes

$$\nabla\cdot\vec{v} = \frac{1}{Rc_\phi}\left[\frac{\partial u}{\partial\psi} + \frac{\partial}{\partial\phi}(c_\phi v).\right] \tag{2}$$

One important quantity is the second order differential

$$\begin{aligned} \nabla\cdot\nabla\vec{v} &= \tfrac{1}{R^2c_\phi^2}\tfrac{\partial}{\partial\psi}\left[\tfrac{\partial u}{\partial\psi}+\tfrac{\partial(c_\phi v)}{\partial\phi}\right]\vec{\imath}_\psi \\ &\quad+\tfrac{1}{R^2}\tfrac{\partial}{\partial\phi}\left[\tfrac{1}{c_\phi}\tfrac{\partial u}{\partial\psi}+\tfrac{1}{c_\phi}\tfrac{\partial(c_\phi v)}{\partial\phi}\right]\vec{\imath}_\phi, \end{aligned} \tag{3}$$

and another is the Laplace operator

$$\nabla^2\eta=\frac{1}{R^2c_\phi}\left[\frac{\partial}{\partial\psi}\left(\frac{1}{c_\phi}\frac{\partial\eta}{\partial\psi}\right)+\frac{\partial}{\partial\phi}\left(c_\phi\frac{\partial\eta}{\partial\phi}\right)\right], \tag{4}$$

where η is the surface elevation, or any other scalar quantity. The convective term becomes

$$\begin{aligned} \vec{v}\cdot\nabla\vec{v} &= \left(\tfrac{u}{Rc_\phi}\tfrac{\partial u}{\partial\psi}+\tfrac{v}{Rc_\phi}\tfrac{\partial(c_\phi u)}{\partial\phi}\right)\vec{\imath}_\psi \\ &\quad\left(\tfrac{u}{Rc_\phi}\tfrac{\partial v}{\partial\psi}+\tfrac{v}{R}\tfrac{\partial v}{\partial\phi}+\tfrac{u^2\sin\phi}{Rc_\phi}\right)\vec{\imath}_\phi. \end{aligned} \tag{5}$$

In addition there is a centripetal acceleration directed against the center of the Earth that is left out. The last contribution in the second line may be important only at very high latitudes and will be left out together with some terms related to the spatial variation of the map factor c_ϕ.

Finally we spell out the vorticity, even though that quantity does not appear explicitly in the Boussinesq equations

$$\nabla\times\vec{v}=\frac{1}{Rc_\phi}\left\{\frac{\partial v}{\partial\psi}-\frac{\partial(c_\phi u)}{\partial\phi}\right\}\vec{\imath}_R+\frac{u}{R}\vec{\imath}_\phi-\frac{v}{r}\vec{\imath}_\psi, \tag{6}$$

where $\vec{\imath}_R$ is the unit vector that is normal to the surface of the Earth.

2.2 Scaling in geographical coordinates

We introduce dimensionless variables according to

$$\begin{aligned} &(\psi,\phi)=\Theta(x,y), && t=\tfrac{R\Theta}{\sqrt{gh_0}} \\ &(u,v)=\epsilon\sqrt{gh_0}(\hat{u},\hat{v}) && h=h_0\hat{h}\quad \eta=\epsilon h_0\hat{\eta} \end{aligned} \tag{7}$$

where the hats indicate dimensionless variables, g is the constant of gravity, h_0 is a characteristic depth and ϵ is an amplitude factor. The characteristic horizontal length (wave length) now becomes $L_c = R\Theta$, which may determine Θ, and the “long wave parameter” is accordingly recognized as

$$\mu^2=\frac{h_0^2}{R^2\Theta^2}. \tag{8}$$

For the physical constants we substitute

$$g=9.81\frac{\mathrm{m}}{\mathrm{s}^2},\qquad R=6378135\,\mathrm{m}. \tag{9}$$

It is emphasized that these quantities are not constant, but their variation is neglected along with other small effects of rotation and the curvature of the Earth, and that the value for R is the equatorial one.

Rotational effects are included simply by adding the Coriolis term to the momentum equation. According to the length and time scale inherent in (7) we the obtain a non-dimensional Coriolis parameter

$$f = \frac{2\Omega R \sin\phi \Theta}{\sqrt{gh_0}}, \tag{10}$$

where Ω is the angular frequency of the Earth.

2.3 Equations and Cartesian scaling

By omission of the hats the dimensionless equation of continuity in geographical coordinates reads

$$c_\phi \frac{\partial \eta}{\partial t} = -\frac{\partial}{\partial x}\{(h+\epsilon\eta)u\} - \frac{\partial}{\partial y}\{c_\phi(h+\epsilon\eta)v\}, \tag{11}$$

where $c_\phi = \cos\phi$ (as before), u and v are the depth-averaged velocity components in the longitudinal and latitudinal directions respectively, h is the equilibrium depth and η is the surface elevation. We observe that the equation (11) is written in conservative form with an area factor at the left hand side.

The momentum equations are obtained by transforming (83), (91) and adding the Coriolis term

$$\begin{aligned}
\tfrac{\partial u}{\partial t} + \epsilon\left(\tfrac{u}{c_\phi}\tfrac{\partial u}{\partial x} + v\tfrac{\partial u}{\partial y}\right) &= -\tfrac{1}{c_\phi}\tfrac{\partial \eta}{\partial x} + fv - \gamma\mu^2 h^2 \tfrac{1}{c_\phi}\tfrac{\partial D_\eta}{\partial x} \\
&\quad + \tfrac{\mu^2}{2}\tfrac{h}{c_\phi^2}\tfrac{\partial}{\partial x}\left[\tfrac{\partial}{\partial x}\left(h\tfrac{\partial u}{\partial t}\right) + \tfrac{\partial}{\partial y}\left(c_\phi h\tfrac{\partial v}{\partial t}\right)\right] \\
&\quad - \mu^2(\tfrac{1}{6}+\gamma)\tfrac{h^2}{c_\phi^2}\tfrac{\partial}{\partial x}\left[\tfrac{\partial}{\partial x}\left(\tfrac{\partial u}{\partial t}\right) + \tfrac{\partial}{\partial y}\left(c_\phi\tfrac{\partial v}{\partial t}\right)\right], \\
\tfrac{\partial v}{\partial t} + \epsilon\left(\tfrac{u}{c_\phi}\tfrac{\partial v}{\partial x} + v\tfrac{\partial v}{\partial y}\right) &= -\tfrac{\partial \eta}{\partial y} - fu - \gamma\mu^2 h^2 \tfrac{\partial D_\eta}{\partial y} \\
&\quad + \tfrac{\mu^2}{2} h \tfrac{\partial}{\partial y}\left[\tfrac{1}{c_\phi}\tfrac{\partial}{\partial x}\left(h\tfrac{\partial u}{\partial t}\right) + \tfrac{1}{c_\phi}\tfrac{\partial}{\partial y}\left(c_\phi h\tfrac{\partial v}{\partial t}\right)\right] \\
&\quad - \mu^2(\tfrac{1}{6}+\gamma) h^2 \tfrac{\partial}{\partial y}\left[\tfrac{1}{c_\phi}\tfrac{\partial}{\partial x}\left(\tfrac{\partial u}{\partial t}\right) + \tfrac{1}{c_\phi}\tfrac{\partial}{\partial y}\left(c_\phi\tfrac{\partial v}{\partial t}\right)\right],
\end{aligned} \tag{12}$$

where $D\eta$ is the dimensionless Laplacian of η which is obtained by replacing R, ψ, ϕ by $1, x, y$ in (4). The optimal factor in the correction term is $\gamma = -0.057$. For a local simulation, in the sense that propagation distances are much smaller than the radii of the earth, we may invoke a constant value for c_ϕ. We observe that the reciprocal of c_ϕ then always combines with $\partial/\partial x$. Transforming the longitudinal coordinate by $\hat{x} = c_\phi x$ we then obtain the Cartesian counterparts to (11) and (12), with no explicit map factors and equal arc-length factors in the two coordinate directions.

While the different choices for horizontal and vertical length scales are useful for presenting the equations with the small terms immediately recognizable they obscure the discussion of simulation results. Hence, unless otherwise is indicated, dimensionless computed results are presented with typical depth h_0 as both vertical and horizontal length scales and no amplitude factor extracted[2]. In the Cartesian equations corresponding to (11) and (12) the small parameters μ and ϵ are then replaced by unity. The new time unit corresponds to the time needed to cover a horizontal distance equal to h_0 with the shallow water speed.

---

[2] Sometimes this scaling is naively accused of being wrong. However, a scaling may be useful, or not, for a given purpose. It is never wrong as long as the content of the equations has not been altered!

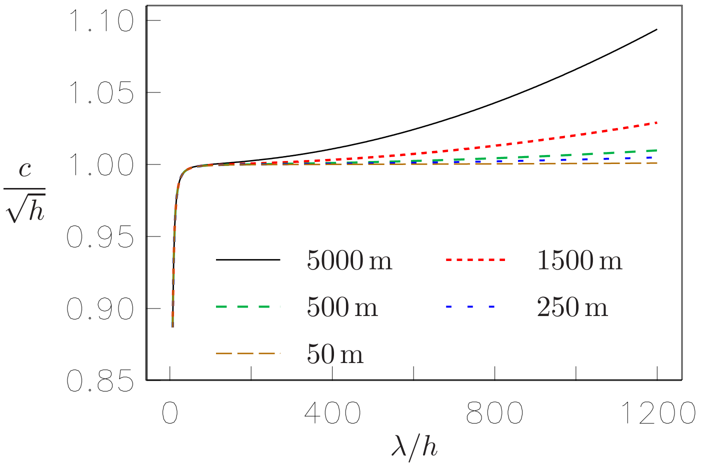

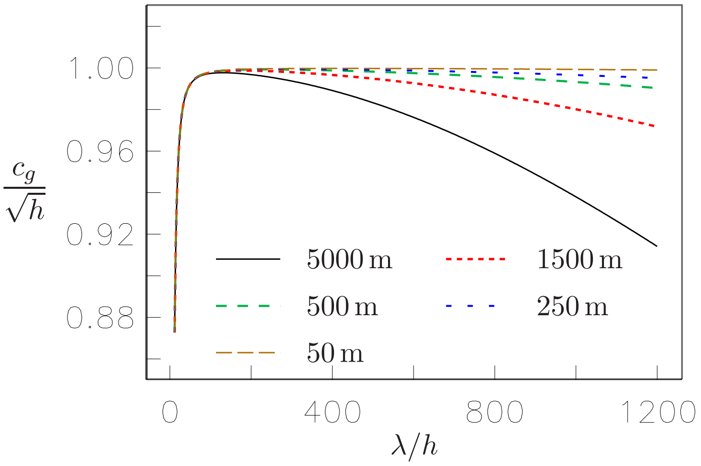

Figure 1: Analytic phase (upper panel) and group velocity (lower panel) for the optimized Boussinesq equations, with the Coriolis effect, and latitude $\phi = 45°$. The curves are labelled by the depth in meters.

2.4 Effects of rotation and curvature

In figure 1 the phase and group velocities are depicted for different depths. Details on the dispersion relation with rotation is found in section 3.4. Naturally, the rotation is important only for longer waves and for the same wavelength-to-depth ratio it is most significant in deep water. However, for $h = 5000\,\text{m}$ the dispersive regime and the rotational regime are still separated, even though rotational effects becomes noticeable for wavelengths larger than 500 km, say. In shallower water the regimes are even more distinctly separated. We may state that a tsunami in a shallow sea may be very long, in the sense of a large wavelength to depth ratio, and that the rotation of the Earth thus may have a certain influence. However, from the perspective of modeling dispersive tsunamis rotation probably means no more than a small modification on the wave pattern over very long propagation distances, like the traversing of the major oceans.

3 Numerical method

From its predecessors our new technique inherits the staggered grid, the temporal representation of the convective terms and the iteration scheme for the implicit equations to be solved at each time step.

For spatial discretization the C-grid is used. This is employed also in the Boussinesq type models of FUNWAVE 2 [40] and that of Beji and Nadaoka [2], in addition to a number of related and unrelated models[3]. However, unlike the cited models the present one also retains a staggered temporal grid. This is used frequently in hydrostatic ocean models, generally under cover of, or interpreted as, a forward/backward time stepping, but is uncommon for Boussinesq models. The staggered time stepping allows a complete decoupling of the implicitness in the continuity equation from that of the momentum equations, which is an advantage. The FUNWAVE/COULWAVE models employ a rather complicated, iterative, Adam-Bashforth predictor-corrector method. Beji and Nadaoka's method, that otherwise has much in common with the present one, utilizes a true leap frog time stepping, where temporal differences at $i\Delta t$ are formed by means of values at $(i+1)\Delta t$ and $(i-1)\Delta t$, say, passing the middle node[4] at $i\Delta t$. While this allows for an explicit treatment of the equation of continuity it effectively doubles the time step, thereby reducing the efficiency of the method. A true leap-frog discretization is also more vulnerable to noise.

In the preceding formulations [36, 26] the implicit momentum equations are solved by a line by line ADI iteration. For the standard Boussinesq equations (12), which has a slightly different structure in the dispersion terms compared to the formulations in those references, this scheme simplifies substantially while the convergence properties are retained. The method then becomes similar to the one employed in [2].

Geographical coordinates and the Coriolis effect are not incorporated in any of the quoted articles on Boussinesq models. However, these features are added to, for instance, the FUNWAVE 2 and their integration in a Boussinesq solver imply no principal difficulties.

3.1 Formalism and grid

To make the descriptions of the numerical details simple and concise we adopt the formalism used in preceding papers [27, 32], which is also similar to that of [19]. The approximation to a quantity f at a grid-point with coordinates $(\beta\Delta x,\ \gamma\Delta y,\ \kappa\Delta t)$ where Δx, Δy and Δt are the grid increments, is denoted by $f^{(\kappa)}_{\beta,\gamma}$. To make the difference equations more compact and legible we introduce the symmetric difference and average operators, δ_x and $\overline{}^{x}$ by

$$\delta_x f^{(\kappa)}_{\beta,\gamma} = \frac{1}{\Delta x}\left(f^{(\kappa)}_{\beta+\frac{1}{2},\gamma} - f^{(\kappa)}_{\beta-\frac{1}{2},\gamma}\right), \quad \left(\overline{f}^{x}\right)^{(\kappa)}_{\beta,\gamma} = \frac{1}{2}\left(f^{(\kappa)}_{\beta+\frac{1}{2},\gamma} + f^{(\kappa)}_{\beta-\frac{1}{2},\gamma}\right). \tag{13}$$

We note that the differences and averages are defined at intermediate grid locations as compared to f. Difference and average operators with respect to the other coordinates y and t are defined correspondingly. It is easily shown that these operators are commutative in all combinations. To abbreviate the expressions further we also group terms of identical indices inside square brackets, leaving the super- and subscripts outside the right bracket. In nonlinear terms it is

---

[3] An example to the latter is the traditional FDM Navier-Stokes model.

[4] This is a *true* leap-frog method. Unfortunately the term is sometimes confused with staggered grids.

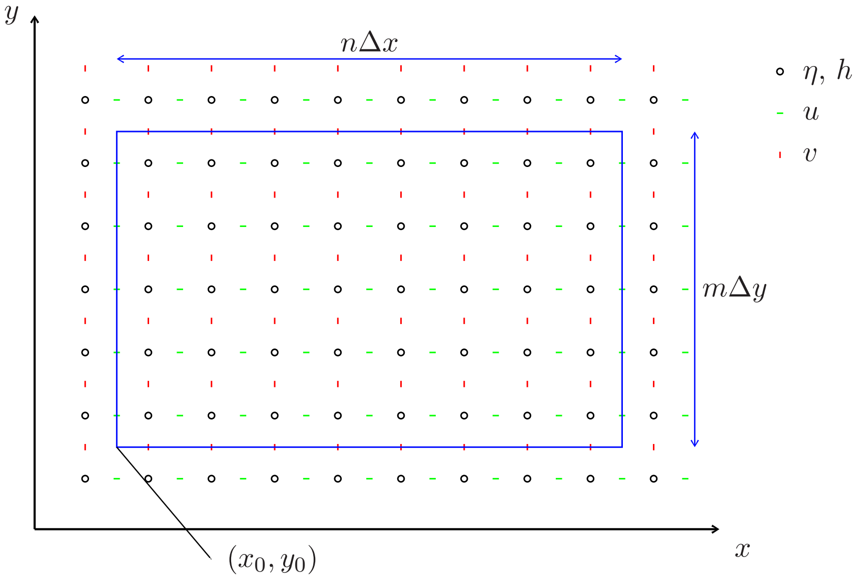

Figure 2: The grid with computational domain (rectangle) and additional points. We observe that the η nodes are symmetrically distributed relative to the computational domain, in contrast to the velocity nodes.

convenient to introduce a special notation for the squared temporal geometrical means

$$\begin{array}{rcl}[f^{(*2)}]^{(k)} & \equiv & f^{(k+\frac{1}{2})}f^{(k-\frac{1}{2})},\\ [f*g]^{(k)} & \equiv & \frac{1}{2}\left(f^{(k+\frac{1}{2})}g^{(k-\frac{1}{2})}+f^{(k-\frac{1}{2})}g^{(k+\frac{1}{2})}\right),\end{array} \tag{14}$$

where the common subscripts are omitted for brevity.

The equations are discretized on a C-grid and our method is thus closely related to, for instance, the standard tsunami models TUNAMI [11, 12] and COMCOT[5], as well as those cited before. Figure 2 displays the definition of the global grid. We observe that fictitious nodes are surrounding the computational domain in a somewhat asymmetric fashion in order to have $(0, n+1) \times (0, m+1)$ matrices for all primary unknowns, as well as the depth. The discrete quantities thus become

$$u^{(k+\frac{1}{2})}_{i,j+\frac{1}{2}}, \quad v^{(k+\frac{1}{2})}_{i+\frac{1}{2},j}, \quad \eta^{(k)}_{i+\frac{1}{2},j+\frac{1}{2}}. \tag{15}$$

3.2 The discrete Boussinesq equations

One of the key points in the C-grid methods is the natural form of conservation of discrete volume in the cell depicted in figure 3. The discrete equation of continuity becomes

$$\left[\delta_t\eta = -r_y\left(\delta_x\{(\overline{h}^x+\epsilon\overline{\eta}^{xt})u\}+\delta_y\{c_v(\overline{h}^y+\epsilon\overline{\eta}^{yt})v\}\right)+\mathcal{A}\right]^{(k+\frac{1}{2})}_{i+\frac{1}{2},j+\frac{1}{2}}, \tag{16}$$

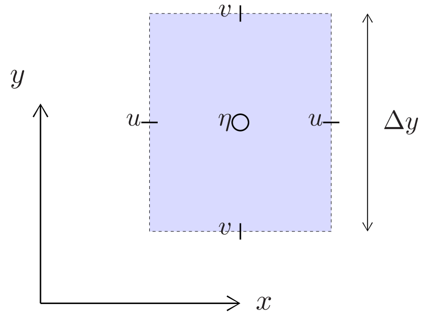

Figure 3: Control cell for volume in the C-grid.

where $\mathcal{A}$ is a numerical correction term to be discussed later, $r_y = 1/c_\phi$ is defined at the η nodes, while $c_v = c_\phi$ is defined at the v nodes. The introduction of both of these stretch factors is convenient for subsequent use and they may both be presented by 1D arrays. Hence, the extra use of memory is insignificant. The equation (16) is exactly volume conserving in the sense that the sum of volume in a cluster of grid cells

$$V^{(k)} = \sum_{i,j} \left[\frac{1}{r_y} \eta \right]^{(k)}_{i+\frac{1}{2},j+\frac{1}{2}},$$

changes only due to a net flux through the external boundary of this cluster.

When all quantities up to (and including) $t = (k+\frac{1}{2})\Delta t$ are computed (16) provides explicit expressions for $\eta^{(n)}_{i,j}$ in the linear case ($\epsilon \to 0$) and a linear, banded set of equations otherwise. For moderately non-linear cases this set is strongly diagonal-dominant and is thus well suited for iterative solution. The iteration procedure is described subsequently and is, among other things, designed as not to violate the volume conservation.

The $x-$component of the momentum equation is discretized according to

$$\begin{aligned}
[\delta_t u + \epsilon T_x \quad = \quad & -\overline{r_y}^x \delta_x \eta + \mathcal{B} + f_u \overline{v}^{xyt} - \gamma \mu^2 (\overline{h}^x)^2 \overline{r_y}^x \tfrac{\partial D_\eta}{\partial x} \\
& + \tfrac{\mu^2}{2} \overline{h}^x (\overline{r_y}^x)^2 \delta_x \{ \delta_x (\overline{h}^x \delta_t u) + \delta_y (c_v \overline{h}^y \delta_t v) \} \\
& - \mu^2 (\tfrac{1}{6} + \gamma)(\overline{h}^x)^2 (\overline{r_y}^x)^2 \delta_x \{ \delta_x \delta_t u + \delta_y (c_v \delta_t v) \}]^{(k)}_{i,j+\frac{1}{2}},
\end{aligned} \tag{17}$$

where $\mathcal{B}$ is a numerical correction term, f_u is the Coriolis parameter evaluated at u-nodes and the nonlinear term is discretized according to

$$\left[T_x = \frac{1}{2} \overline{r_y}^x \delta_x \{ (\overline{u}^x)^{(*2)} \} + \overline{\overline{v}^x * \delta_y u}^y \right]^{(k)}_{i,j+\frac{1}{2}}. \tag{18}$$

This representation is designed from three requirements

(i) The equation set for $u^{(k+\frac{1}{2})}_{i,j+\frac{1}{2}}$ should be linear.

(ii) Numerical dissipation is avoided through the use of symmetric differences and averages.

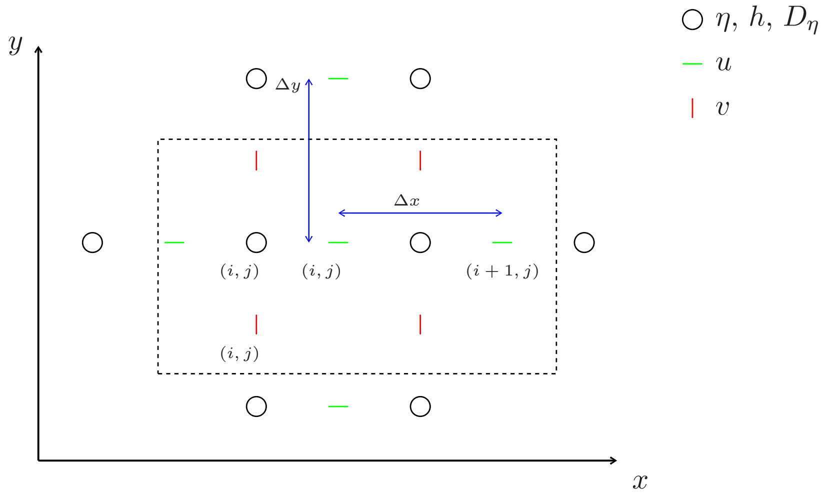

Figure 4: Computational molecule, centered at point (i,j), for the x-component of the momentum equation. In the linear case without corrected dispersion only the nodes within the dashed box are involved. The u and η nodes outside the box enter through the non-linear term and D_η, respectively.

(iii) Fictitious values outside an impermeable boundary do not enter the discrete momentum equation since they are always multiplied with a zero normal velocity.

The formula (18) is well suited for long distance propagation of moderately nonlinear waves, but is presumably not the best choice if run-up on sloping beaches or wave breaking should be considered.

The combination of (17) and (18) yields the computational molecule in figure 4. The y-component is discretized in a similar fashion, but differs slightly due to the latitude-dependent factors and the sign of the Coriolis term. Subsequently we will express the two components of the momentum equations in a single generic form (section 3.8). Provided everything is known for $t \leq k\Delta t$ (17) and its y-component counterpart define a coupled, linear and banded equation system for the new velocities[5]. For non-zero μ the solution of this system is more demanding than the system from the continuity equation since the third order differences in the dispersion terms cause large off-diagonal entries in the matrices, due to the cubic reciprocals of grid increments.

In general no smoothing or filtering is applied to the discrete equations. However, an optional number of five point filtering may be applied to D_η and the correction flux components in $\mathcal{A}$, which are described in section 3.5.

3.3 Boundary conditions

Every boundary of a volume cell (see figure 3) may represent a piece of a no-flux boundary. In a staircase fashion a boundary of any shape may then be approximated, even though the

---

[5] Actually we solve the equations for $\delta_t u$ and $\delta_t v$.

accuracy may be poor and spurious effects must sometimes be expected. The code will be designed as to assure no influence on the solution from any points outside a no-flux boundary, except for the dispersion optimization term D_η in (12). Linear extrapolation along the grid lines from the adjacent points to the boundary was attempted, but produced instabilities. Instead the invocation, in this term alone, of a symmetry condition for η seems to work well. As an alternative to no-flux boundaries we may have boundaries (straight or staircase) beyond which the computation is simply switched off. These may then be input boundaries in, for instance, a nested model or when several grids are combined in domain decomposition approach. Run-up techniques may probably be adopted from related C-grid models, at least when the dispersion terms are renounced close to the shoreline.

At open boundaries a simple sponge layer is implemented as a separate step where all the primary unknowns are relaxed according to a simple formula

$$[\eta = \nu\tilde{\eta}]^{(k)}_{i+\frac{1}{2},j+\frac{1}{2}},$$

where the tilde marks values that are found from stepping forward with the discrete equations. The parameter ν is less than unity in a layer, of width L_s, close to one of the global boundaries

$$\nu = \begin{cases} 0, & \text{when } \frac{s}{L_s} \geq 1, \\ \sin^2\left(\frac{\pi s}{2L_s}\right), & \text{when } \frac{s}{L_s}, < 1 \end{cases}$$

where s is the distance from the boundary. Also other shape functions, such as exponential ones, have been tested. All reasonable choices for shape functions and widths have yielded efficient absorbing layers for waves propagating toward the boundary, but much less so for waves with very oblique incidence on the boundary.

The temporally staggered grid is a little awkward in relation to initial conditions. If the surface elevation and the velocities are given at $t = 0$, say, we make a first order error by substituting the velocity directly into $u_{\cdot\cdot}^{-\frac{1}{2}}$ and $v_{\cdot\cdot}^{-\frac{1}{2}}$. This is the case even if the initial velocities are zero. For many applications, such as most tsunami simulations, this is naturally of little consequence. However, for academic applications and code testing this $O(\Delta t)$ error source may be annoying. Hence, it is removed by employing the discrete momentum equations at $t = 0$ with time step[6] $-\frac{1}{2}\Delta t$. In fact, the same approach is applied when the initial velocities are specified at some $t_u = O(\Delta t)$ rather than at $t = 0$. This is useful for importing initial conditions from other models with staggered temporal grids.

3.4 Numerical dispersion relations and stability

To obtain simple wave modes as solutions of the differential equations, (11) and (12), or difference equations, (16) and (17) etc., we have to assume vanishing amplitudes ($\epsilon \longrightarrow 0$), constant depth and constant latitude. The latter then implies that the Coriolis parameter as well as the map factor c_ϕ, and thereby r_y and c_v, are constant. It is then convenient to employ $\hat{x} = c_\phi x$ as longitudinal coordinate and write

$$\begin{pmatrix} \eta(\hat{x}, y, t) \\ u(\hat{x}, y, t) \\ v(\hat{x}, y, t) \end{pmatrix} = \begin{pmatrix} A \\ A_u \\ A_v \end{pmatrix} e^{i(k\hat{x}+\ell y-\omega t)}.$$

---

[6] Actually the accelerations are computed and then $-\frac{1}{2}\Delta t$ times the accelerations are added to the velocities.

We note that the discrete equations in (x, y) transform to discrete equations in $(\hat{x}, y)$ with map factors replaced by unity and Δx replaced by $\Delta\hat{x} = c_\phi \Delta x$. Moreover, we set the numerical correction terms, $\mathcal{A}, \mathcal{B}, \mathcal{C}$ (in the y component of the momentum equation), to zero. Substitution into the discrete equations now yields the dispersion relation

$$\tilde{\omega}^2 = \frac{h(\tilde{k}^2 + \tilde{\ell}^2)\{1 - \gamma\mu^2 h^2(\tilde{k}^2 + \tilde{\ell}^2)\} + \tilde{c}_x^2 \tilde{c}_y^2 \tilde{c}_t^2 f^2}{1 + (\frac{1}{3} - \gamma)\mu^2 h^2 (\tilde{k}^2 + \tilde{\ell}^2)}, \tag{19}$$

where

$$\begin{aligned} \tilde{k} &\equiv \tfrac{2}{\Delta\hat{x}} \sin(\tfrac{1}{2} k\Delta\hat{x}), & \tilde{\ell} &\equiv \tfrac{2}{\Delta y}\sin(\tfrac{1}{2}\ell\Delta y), & \tilde{\omega} &\equiv \tfrac{2}{\Delta t}\sin(\tfrac{1}{2}\omega\Delta t), \\ \tilde{c}_x &\equiv \cos(\tfrac{1}{2}k\Delta\hat{x}), & \tilde{c}_y &\equiv \cos(\tfrac{1}{2}\ell\Delta y), & \tilde{c}_t &\equiv \cos(\tfrac{1}{2}\omega\Delta t). \end{aligned} \tag{20}$$

The analytic dispersion relation corresponds to $\tilde{k} \to k$, $\tilde{\ell} \to \ell$, $\tilde{\omega} \to \omega$ and $\tilde{c}_x, \tilde{c}_y, \tilde{c}_t \to 1$. From (20) we immediately realize that this is obtained in the limit $\Delta\hat{x}, \Delta y, \Delta t \to 0$.

In the analytic, non-rotational case, $f = 0$, the properties of the dispersion is discussed in appendix A. For $f \neq 0$ and finite grid increments (19) becomes an implicit expression for ω that may be written

$$\tilde{\omega}^2 = \frac{B_1 + f^2\tilde{c}_x^2\tilde{c}_y^2\tilde{c}_t^2}{B_2},$$

where B_1 and B_2 are the chunks of (19) that are independent of f and ω. The above relation can swiftly be reorganized into

$$\left(\frac{4B_2}{\Delta t^2} + f^2\tilde{c}_x^2\tilde{c}_y^2\right)\sin^2(\frac{1}{2}\omega\Delta t) = B_1 + f^2\tilde{c}_x^2\tilde{c}_y^2.$$

Stability now requires

$$\left(\frac{4B_2}{\Delta t^2} + f^2\tilde{c}_x^2\tilde{c}_y^2\right) \geq B_1 + f^2\tilde{c}_x^2\tilde{c}_y^2,$$

or

$$\frac{4B_2}{\Delta t^2} \geq B_1,$$

which implies that the stability criterion is independent of f. We then obtain

$$h\Delta t^2 \leq \frac{1 + 4(\frac{1}{3} - \gamma)\mu^2 h^2\left(\frac{1}{\Delta\hat{x}^2} + \frac{1}{\Delta y^2}\right)}{\left(\frac{1}{\Delta\hat{x}^2} + \frac{1}{\Delta y^2}\right)\left(1 - 4\gamma\mu^2\left(\frac{1}{\Delta\hat{x}^2} + \frac{1}{\Delta y^2}\right)\right)}, \tag{21}$$

which is markedly more liberal than the standard CFL criterion.

The group velocity is defined as

$$\vec{c}_g = (c_g^{(x)}, c_g^{(y)}) = \left(\frac{\partial\omega}{\partial k}, \frac{\partial\omega}{\partial\ell}\right).$$

Observing that $\partial\tilde{k}/\partial k = \tilde{c}_x$ etc. we differentiate (19) to obtain

$$\begin{aligned} c_g^{(x)} &= (2\tilde{\omega}\tilde{c}_t B_2)^{-1} && \{2(h - 2\gamma h^3(\tilde{k}^2 + \tilde{\ell}^2)) - \tfrac{\Delta x^2}{2} f^2 \tilde{c}_y^2) \\ & && -\tilde{\omega}^2(2(\tfrac{1}{3} - \gamma)h^2 - \tfrac{\Delta t^2 \Delta x^2}{8} f^2\tilde{c}_y^2)\}\tilde{c}_x\tilde{k} \\ c_g^{(y)} &= (2\tilde{\omega}\tilde{c}_t B_2)^{-1} && \{2(h - 2\gamma h^3(\tilde{k}^2 + \tilde{\ell}^2)) - \tfrac{\Delta y^2}{2} f^2 \tilde{c}_x^2) \\ & && -\tilde{\omega}^2(2(\tfrac{1}{3} - \gamma)h^2 - \tfrac{\Delta t^2 \Delta y^2}{8} f^2\tilde{c}_x^2)\}\tilde{c}_y\tilde{\ell} \end{aligned} \tag{22}$$

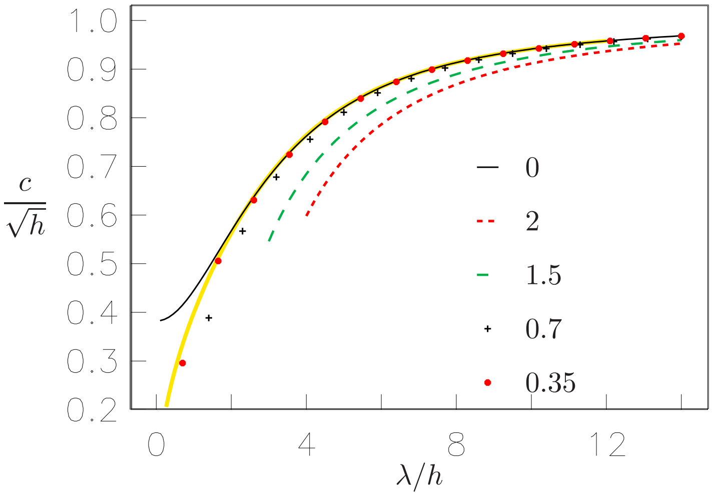

Figure 5: Phase velocities for the Boussinesq equations with $\gamma = -0.057$ and direction of wave advance $\theta = 0°$. The curves are labelled by $\Delta\hat{x}/h$, apart from the bold yellow line that corresponds to full potential theory. The other grid increments are $\Delta y = \Delta\hat{x}$ and $\Delta t = \frac{1}{2}h^{-\frac{1}{2}}\Delta\hat{x}$.

Some examples of phase velocities are shown in figures 5 and 6, while the corresponding group velocities are found in figures 7 and 8. We observe that the numerical dispersion relation is somewhat closer to its analytic counterpart for the standard model. However, this barely an interesting feature since the difference is largest for the shorter waves, for which only the optimized model yield an accurate description. Moreover, we also see that the group velocity becomes zero for the shortest possible waves that may be present in the grid. It is easily realized that this is general property, with a few exceptions only ($\mu = \ell = 0$, $\sqrt{h}\Delta t = \Delta\hat{x}$ or $\mu = k = 0$, $\sqrt{h}\Delta t = \Delta y$). As a consequence, noise on the grid level will remain close to its origin, which means close to the generation region in a tsunami simulation. In the figures 5 through 8 we have also included the wave celerities from the full potential theory for comparison. For the optimized equations ($\gamma = -0.057$) we observe that the numerical solution for $\Delta\hat{x}/h = 0.35$ follows the full potential theory much longer than the analytic one ($\Delta\hat{x} = 0$), the numerical wave celerities decrease monotonically as λ decreases. This is a reminder that there may be no gain in requiring higher accuracy in a numerical technique than what is inherent in the differential equations in the first place.

For small wave numbers and grid increments we may expand the relation (19) in powers of wave numbers and grid increments. Defining the wave number vector as $(k, \ell) = |\mathbf{k}|(\cos\theta, \sin\theta)$, where θ is the direction of wave advance, and neglecting rotational effects we obtain

$$\omega = \sqrt{h}|\mathbf{k}|\left\{1 - \beta|\mathbf{k}|^2 + O(|\mathbf{k}|^4\Delta\hat{x}^2, \Delta\hat{x}^4 ...)\right\}, \tag{23}$$

where

$$\beta = \frac{\mu^2 h^2}{6} + \frac{1}{24}(\Delta\hat{x}^2\cos^4\theta + \Delta y^2\sin^4\theta - h\Delta t^2). \tag{24}$$

It is noteworthy that the error term in β vanish for $\theta = 0, \pi$, $\sqrt{h}\Delta t = \Delta\hat{x}$ or $\theta = \frac{\pi}{2}, \frac{3\pi}{2}$, $\sqrt{h}\Delta t = \Delta y$, which correspond to propagation parallel to one of the axes and then an unitary

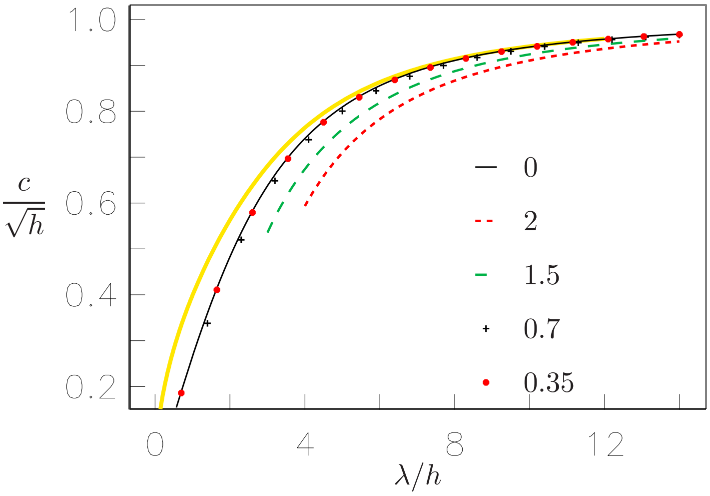

Figure 6: Phase velocities for the Boussinesq equations with $\gamma = 0.0$ and direction of wave advance $\theta = 0°$. The curves are labelled by $\Delta\hat{x}/h$, apart from the bold yellow line that corresponds to full potential theory. The other grid increments are $\Delta y = \Delta\hat{x}$ and $\Delta t = \frac{1}{2}h^{-\frac{1}{2}}\Delta\hat{x}$.

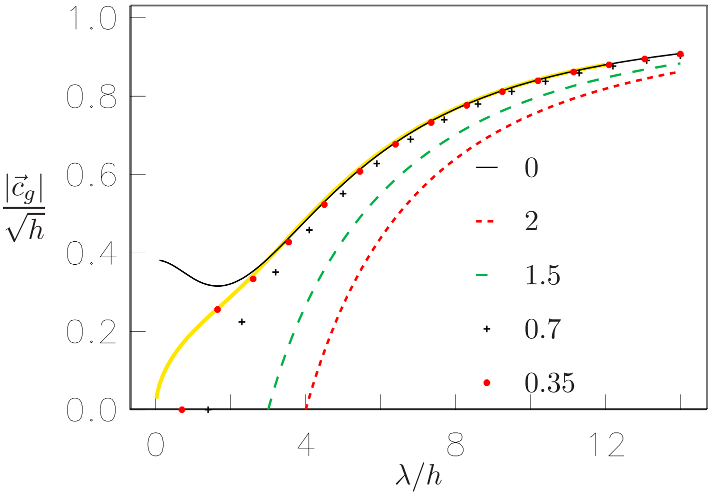

Figure 7: Group speed for the Boussinesq equations with $\gamma = -0.057$ and direction of wave advance $\theta = 0°$. The curves are labelled by $\Delta\hat{x}/h$, apart from the bold yellow line that corresponds to full potential theory. The other grid increments are $\Delta y = \Delta\hat{x}$ and $\Delta t = \frac{1}{2}h^{-\frac{1}{2}}\Delta\hat{x}$.

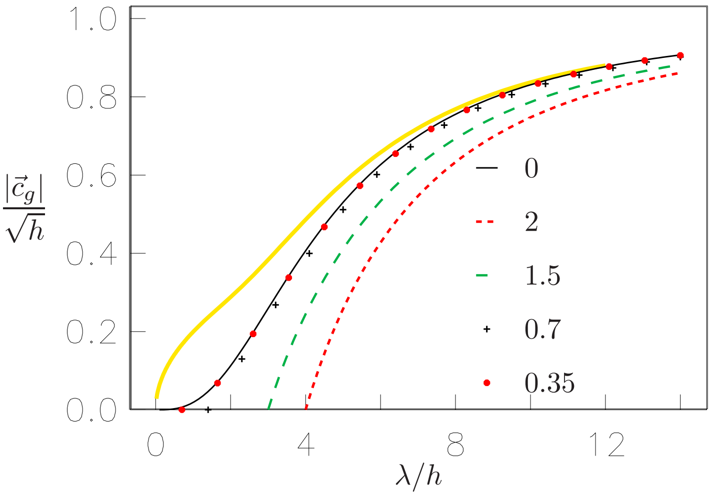

Figure 8: Group speed for the Boussinesq equations with $\gamma = 0.0$ and direction of wave advance $\theta = 0°$. The curves are labelled by $\Delta\hat{x}/h$, apart from the bold yellow line that corresponds to full potential theory. The other grid increments are $\Delta y = \Delta\hat{x}$ and $\Delta t = \frac{1}{2}h^{-\frac{1}{2}}\Delta\hat{x}$.

Courant number. Under the same conditions we have an exact solution for $\mu = 0$. We observe that while a good approximation of the wave celerity requires that the grid increments are small compared to the wavelengths, the increments have to be small compared to the depth to reproduce dispersion effects properly (give an accurate β). This is relevant for weakly dispersive tsunamis crossing an ocean. For instance, if we assume a $2'$ grid, that a long wave travels $\frac{1}{2}\Delta\hat{x}$ in the time step Δt and a depth of 5 km and northward wave propagation we find $\beta/(h^2/6) = 1.1$. This resolution is typical for the simulation trans-oceanic propagation that can be completed within some hours on a single CPU. While the qualitative dispersive features are probably well retained this motivates the inclusion of numerical correction terms. A further analysis on the significance of the numerical dispersion (error in β) is presented in section 4.1.

The numerical part of β has the same form as the analytical one. Hence, for, for example, wave propagation parallel to the x-axis we may reproduce the correct value of β with $\mu = 0$ and $\sqrt{\Delta\hat{x}^2 - h\Delta t^2} = 2\mu h$, meaning that we have a course grid with an increment that is somewhat larger than twice the depth. This implies that we would obtain correct leading order dispersion by simulating the LSW equations with grid increments fulfilling the relation given, even though optimized dispersion properties are harder to obtain. At first glance this looks like an egg of Columbus. However, there are a series of problems related to turning this observation into a useful computational strategy. First, four our model we will obtain the correct dispersion only for a single depth, unless we employ an adaptive grid. In one horizontal direction (1HD) this is rather straightforward, but it is hardly achievable in 2HD. Moreover, the anisotropy of the numeric dispersion will anyhow prevent an exact reproduction of β. Using other methods [45, 46] these problems may be amended, but the problem of coarse grids remain. Firstly, moderately short waves where an improved Boussinesq model, such as that of Nwogu, is still good can hardly be resolved at all. Secondly, and most important, the grids are to coarse to allow a proper representation of bathymetric effects and nonlinearity.

3.5 Numerical correction terms

In the preceding section the numerical errors surface in the leading dispersion as given by the β in (23). To obtain the correct long term properties in the evolution of a weakly dispersive wave train it is crucial that β should be close to its analytical value of $h^2/6$. For the uncorrected FDM method this will in general require grid increments that are small compared to h, even though $\frac{1}{2}h$ may be regarded as fairly small in this context. In the COULWAVE [20] and FUNWAVE [16, 15] models fourth order spatial representations are used for the linear, $O(\mu^0)$ terms (inherent in the LSW parts of the equations), while second order differences are used for the $O(\mu^2)$ terms. When this is combined with a fourth order temporal method the numerical errors will disappear altogether from β as defined above. An alternative to such a procedure is the inclusion of terms that improve the accuracy of the discrete solution, either completely or only concerning certain aspects, and not of the individual terms. To this end we apply a similar procedure to those found in [36, 27]. In these references simple terms were designed as to correct the dispersion, while other properties, such as the relation between the surface elevation and the velocity in harmonic modes, were not corrected. For the present equation set we have not found this strategy of partially fourth order method for the LSW terms fruitful. Hence, we aim at slightly more complex correction terms that remove the $O(\Delta x^2..)$ errors from the continuity and momentum equations independently, leaving us with numerical errors of order $(\Delta x^4, \mu^2\Delta x^2...)$.

3.5.1 Outline

Since we only aim at removing errors in the leading order terms we may analyze the discrete equations in the form

$$\left[\delta_t\eta = -r_y\left(\delta_x(h^{(u)}u) + \delta_y(c_v h^{(v)}v)\right) + \mathcal{A}\right]^{(k+\frac{1}{2})}_{i+\frac{1}{2},j+\frac{1}{2}}, \tag{25}$$

$$[\delta_t u = -\overline{r_y}^x\delta_x\eta + \mathcal{B}]^{(k)}_{i,j+\frac{1}{2}}, \tag{26}$$

$$[\delta_t v = -\delta_y\eta + \mathcal{C}]^{(k)}_{i+\frac{1}{2},j}, \tag{27}$$

where the correction terms, $\mathcal{A}$, $\mathcal{B}$, $\mathcal{C}$, must be determined. We have already replaced the averaged expressions for the depths by presumably improved values[7].

The relation between a derivative and a centered difference reads

$$\delta_t u = \frac{\partial u}{\partial t} + \frac{1}{24}\Delta t^2\frac{\partial^3 u}{\partial t^3} + O(\Delta t^4). \tag{28}$$

Inserting such expressions into (25) through (27) we obtain difference/differential equations

$$\eta_t + r_y\{(hu)_x + (c_v hv)_y\} = -\frac{\Delta t^2}{24}\eta_{ttt} - r_y\{\frac{\Delta x^2}{24}(hu)_{xxx} + c_v\frac{\Delta y^2}{24}(hv)_{yyy}\} + \mathcal{A} + ..., \tag{29}$$

$$u_t + r_y\eta_x = -\frac{\Delta t^2}{24}u_{ttt} - r_y\frac{\Delta x^2}{24}\eta_{xxx} + \mathcal{B} + ..., \tag{30}$$

$$v_t + \eta_y = -\frac{\Delta t^2}{24}v_{ttt} - \frac{\Delta y^2}{24}\eta_{yyy} + \mathcal{C} + ..., \tag{31}$$

---

[7] Such values may not be available in digitized bathymetries, but the corrections of other discrete errors may still be useful.

where the implicit errors are of fourth order in the grid increments and errors from discretization of map factors have been neglected. Indices are now used for differentiations to abbreviate the expressions. Due to the implicit fourth order errors we may regard the correction factors ($\mathcal{A}$ etc.) as consisting of either derivatives or corresponding second order finite difference expressions. Expanding the correction terms according to

$$\begin{aligned}
\mathcal{A} &= \tfrac{\Delta t^2}{24}\mathcal{A}^{(t)} + \tfrac{\Delta x^2}{24}\mathcal{A}^{(x)} + \tfrac{\Delta y^2}{24}\mathcal{A}^{(y)}, \\
\mathcal{B} &= \tfrac{\Delta t^2}{24}\mathcal{B}^{(t)} + \tfrac{\Delta x^2}{24}\mathcal{B}^{(x)} + \tfrac{\Delta y^2}{24}\mathcal{B}^{(y)}, \\
\mathcal{C} &= \tfrac{\Delta t^2}{24}\mathcal{C}^{(t)} + \tfrac{\Delta x^2}{24}\mathcal{C}^{(x)} + \tfrac{\Delta y^2}{24}\mathcal{C}^{(y)},
\end{aligned} \tag{32}$$

we obtain a fourth order representation of the leading balance of the equations provided

$$\begin{array}{lll}
\mathcal{A}^{(t)} = \eta_{ttt} + \text{so}, & \mathcal{A}^{(x)} = r_y(hu)_{xxx} + \text{so}, & \mathcal{A}^{(y)} = r_y c_v (hv)_{yyy} + \text{so}, \\
\mathcal{B}^{(t)} = u_{ttt} + \text{so}, & \mathcal{B}^{(x)} = r_y \eta_{xxx} + \text{so}, & \mathcal{B}^{(y)} = \text{so}, \\
\mathcal{C}^{(t)} = v_{ttt} + \text{so}, & \mathcal{C}^{(x)} = \text{so}, & \mathcal{C}^{(y)} = \eta_{yyy} + \text{so},
\end{array} \tag{33}$$

where so $= O(\Delta x^2, \Delta y^2, \Delta t^2)$. Now, discrete versions of the derivatives on the right hand sides in these expressions are not all suitable options for the correction terms. The third order temporal derivatives, in particular, will then violate the structure of the discrete equations and render them less useful[8]. Instead the right hand sides must be rewritten using the leading order balances of (29) through (31), which simply reduce to the LSW equations. From these we may also derive second order relations on the form

$$\begin{aligned}
\eta_{tt} &= r_y^2 (h\eta_x)_x + (h\eta_y)_y, \\
u_{tt} &= r_y^2 (hu)_{xx} + r_y (hv)_{xy}, \\
v_{tt} &= r_y (hu)_{xy} + (hv)_{yy}.
\end{aligned} \tag{34}$$

In these expressions we have assumed constant map factors in accordance with the neglect of discretization errors in the map factors in the first place. Below these factors are allowed to slip inside and outside of differential and difference operators as we see fit.

3.5.2 Corrected methods

From the first equalities in (33) and (34) we have

$$\begin{aligned}
\mathcal{A}^{(t)} &= \eta_{ttt} + \text{so} = r_y^2 (h\eta_x)_{xt} + (h\eta_y)_{yt} + \text{so} \\
&= -r_y^3 (h\{(hu)_x + (c_v hv)_y\}_x)_x - r_y (h\{(hu)_x + (c_v hv)_y\}_y)_y + \text{so} \\
&= -r_y^3 \delta_x(\overline{h}^x \delta_x\{\delta_x(\overline{h}^x u) + \delta_y(c_v \overline{h}^y v)\}) - r_y \delta_y(\overline{h}^y \delta_y\{\delta_x(\overline{h}^x u) + \delta_y(c_v \overline{h}^y v)\}) + \text{so}.
\end{aligned} \tag{35}$$

While the triple temporal derivative is awkward, the rightmost expression in the first line can be used in an implicit formulation of the equation of continuity. However, also the last line

---

[8] Asymmetric second order representations, invoking values from at least three preceding time steps can be contemplated. This will be reminiscent of the time stepping in FUNWAVE/COULWAVE. However, extra memory is required and the resulting method will not be neutrally stable.

possesses some desirable features (see below), in spite of the lengthy appearance. For the other components of $\mathcal{A}$ we may simply use

$$\mathcal{A}^{(x)} = r_y \delta_x^3 (\overline{h}^x u) + \text{so}, \quad \mathcal{A}^{(y)} = r_y \delta_y^3 (c_v \overline{h}^y v) + \text{so}. \tag{36}$$

Now, in conservative form, the corrected discrete equation of continuity should be written according to

$$\delta_t \eta = -r_y \left(\delta_x \{ (\overline{h}^x + \epsilon \overline{\eta}^{xt}) u + Q^{(x)} \} + \delta_y \{ c_v (\overline{h}^y + \epsilon \overline{\eta}^{yt}) v + Q^{(y)} \} \right).$$

When the expressions on the first line of (35) is used the correction fluxes takes on the form

$$\begin{aligned} Q^{(x)} &= -\tfrac{1}{24} (\Delta t^2 r_y \overline{h}^x \delta_x \delta_t \eta + \Delta x^2 \delta_x \mathcal{D}^{(x)}), \\ Q^{(y)} &= -\tfrac{1}{24} (\Delta t^2 c_\phi \overline{h}^y \delta_y \delta_t \eta + \Delta y^2 \delta_y \mathcal{D}^{(y)}), \end{aligned} \tag{37}$$

where $\mathcal{D}^{(x)}$ and $\mathcal{D}^{(y)}$ are the linear divergence contributions $\delta_x(\overline{h}^x u)$ and $\delta_y(c_\phi \overline{h}^y v)$, respectively. Employing the last line of (35) we obtain the purely explicit correction terms

$$\begin{aligned} Q^{(x)} &= \tfrac{1}{24} (\overline{r_y}^{x\,2} \overline{h}^x \Delta t^2 - \Delta x^2) \delta_x \mathcal{D}^{(x)} + \tfrac{\overline{r_y}^{x\,2} \overline{h}^x \Delta t^2}{24} \delta_x \mathcal{D}^{(y)}, \\ Q^{(y)} &= \tfrac{1}{24} (\overline{h}^y \Delta t^2 - \Delta y^2) \delta_y \mathcal{D}^{(y)} + \tfrac{\overline{h}^y \Delta t^2}{24} \delta_y \mathcal{D}^{(x)}, \end{aligned} \tag{38}$$

We observe that $\mathcal{D}^{(x)}$ and $\mathcal{D}^{(y)}$ anyhow must be computed due to the leading order divergence term, even though that may be difficult to exploit in an efficient manner, and that the extra computations required by the correction is limited. In addition the corrections does not affect the iteration. One might have been concerned about the combination of the corrections terms and irregular staircase boundaries. However, we set also the flux corrections to zero at the boundary segments and the remaining fluxes can be computed without involving "dry" values, in analogy to the dispersion terms of the momentum equation.

The corrections to the momentum equation also require a little reworking of the temporal parts

$$\begin{aligned} \mathcal{B}^{(t)} &= \overline{r_y}^{x\,2} \{ \delta_x^2 (\overline{h}^x \delta_t u) + \delta_x \delta_y (c_v \overline{h}^y \delta_t v) \} + \text{so}, \\ \mathcal{C}^{(t)} &= \overline{r_y}^{y} \{ \delta_y \delta_x (\overline{h}^x \delta_t u) + \delta_y^2 (c_v \overline{h}^y \delta_t v) \} + \text{so}. \end{aligned} \tag{39}$$

Discretizing the third order spatial derivatives in (32) directly we find

$$\mathcal{B}^{(x)} = +r_y \delta_x^3 \eta + \text{so}, \quad \mathcal{C}^{(y)} = \delta_y^3 \eta + \text{so}, \tag{40}$$

while $\mathcal{B}^{(y)} = \mathcal{C}^{(x)} = 0$. The expressions in (40) yield contributions to the discrete momentum equations that are similar to the analytic correction terms, related to D_η, in (12). On the other hand, if we rewrite $\mathcal{B}^{(x)}$ and $\mathcal{C}^{(y)}$ by means of the leading order momentum equations, $u_t = -r_y \eta_x$ and $v_t = -\eta_y$ we arrive at the alternative forms

$$\mathcal{B}^{(x)} = -\delta_x^2 \delta_t u + \text{so}, \quad \mathcal{C}^{(y)} = -\delta_y^2 \delta_t v + \text{so}, \tag{41}$$

These expressions are similar to the ordinary dispersion terms and thus readily included by adjusting a few coefficients. Naturally, the different options for numerical corrections may be combined, as weighted averages, in the equations for both momentum and continuity. Furthermore, we may observe that the corrections terms, in all varieties, are similar to either the dispersion terms that are present in the standard Boussinesq equations or extra terms that appear in Nwogu's formulation or the optimized version of the standard formulation ($\gamma < 0$). Presently, only the combination (38) and (41) is implemented in the software. This is a good choice, but subsequent analysis will indicate that other options may work slightly better under given circumstances.

One extra remark is now timely. The inclusion of the analytical correction term for dispersion followed by the numerical counterpart may be regarded as a patchwork. Of course, the desirable strategy would be to include both kinds of corrections simultaneously and then subject the total discrete equations to an optimization process with regard to performance. However, the methodology is far from obvious, and neither are the criteria for good model performance. For instance, the analytic correction only relates to constant depth propagation, while the numeric counterparts also may take depth gradients into account.

3.5.3 Discussion of correction terms

Ignoring the the Coriolis effect, deleting the nonlinear terms and assuming constant depth, constant map factors and wave advance parallel to the $\hat{x}$ axis, we obtain the generic corrected discrete equations in the form

$$\delta_t\eta = -h\delta_x u + q_c\delta_x^2\delta_t\eta - p_c h\delta_x^3 u, \tag{42}$$

$$\delta_t u = -\delta_x\eta + (q_m - \gamma\mu^2h^2)\delta_x^3\eta + \{\mu^2(\frac{1}{3} - \gamma)h^2 + p_m\}\delta_x^2\delta_t u, \tag{43}$$

where the hats over x are omitted here and in the remainder of subsection 3.5 and

$$q_c = f_c\tfrac{\Delta t^2}{24}h, \quad p_c = \tfrac{1}{24}((1-f_c)h\Delta t^2 - \Delta x^2),$$
$$q_m = f_m\tfrac{\Delta x^2}{24}, \quad p_m = \tfrac{1}{24}(h\Delta t^2 - (1-f_m)\Delta x^2).$$

Here the factors f_c and f_m are, to some extent, arbitrary numbers. f_c=0 corresponds to (38), $f_c = 1$ to (37), and an intermediate value to a combination of the two options for flux correction. It is natural to regard f_c as being between 0 and 1, but there is no principal reason for excluding values somewhat outside this interval. The other factor f_m is 0 and 1 for (41) and (40), respectively. We note that for $f_c = f_m = 0$ the correction terms disappear when the Courant number equals unity, which is consistent with (23) and (24). We readily obtain a dispersion relation from (42) and (43) on the form

$$\tilde{\omega}^2 = \frac{h\tilde{k}^2(1 + (q_m - \gamma\mu^2h^2)\tilde{k}^2)(1 - p_c\tilde{k}^2)}{(1 + \{\mu^2h^2(\frac{1}{3} - \gamma) + p_m\}\tilde{k}^2)(1 + q_c\tilde{k}^2)}. \tag{44}$$

As mentioned in appendix A the differential equations are only stable for $\gamma < 0$. The q and p factors are generally positive and negative, respectively. If p_c and p_m could have been fixed number, while $\Delta x, \Delta t \to 0$, both the second parenthesis in the numerator and the correction part in denominator may point to instabilities for short waves. However, since p_c and p_m are dependent on the grid increments this instability is not realized

$$|p_c\tilde{k}^2| < \frac{1}{6}\left|1 - (1 - f_c)\frac{h\Delta t^2}{\Delta x^2}\right|, \quad |p_m\tilde{k}^2| < \frac{1}{6}\left|1 - f_m - \frac{h\Delta t^2}{\Delta x^2}\right|.$$

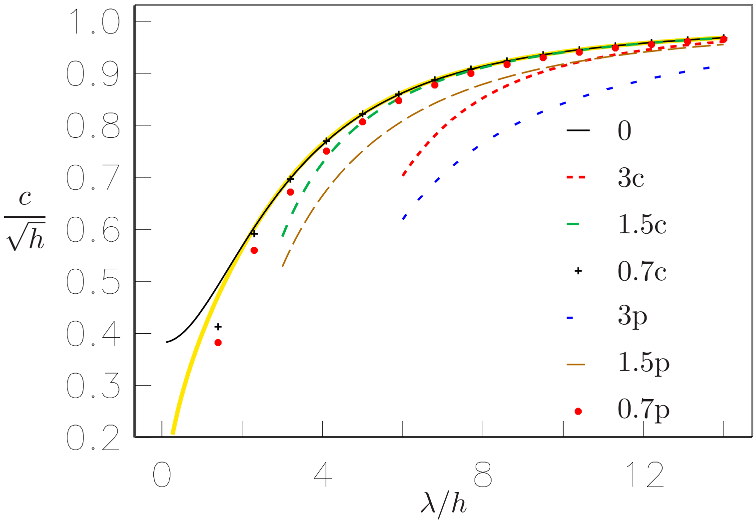

Figure 9: Phase velocities for the Boussinesq equations with $\gamma = -0.057$ and direction of wave advance $\theta = 0°$. The curves are labelled by $\Delta\hat{x}/h$ together with "c" and "p" for corrected and uncorrected numerical methods, respectively, expect for full potential theory that is depicted in bold yellow. The time step is $\Delta t = \frac{1}{2}h^{-\frac{1}{2}}\Delta\hat{x}$ and $f_c = f_m = 0$.

Hence, unless the factors f_c and f_m, or the Courant number, are exceptionally large no change of sign, that may cause instability, is possible in neither numerator nor denominator. Similar limitations will apply to the other correction terms that appear in the general case in 2HD.

Dispersion relations with and without the discrete correction terms are compared in the figures 9 and 10. The results are restricted to $f_c = f_m = 0$, while other forms of the correction term are discussed in the next subsection. We see an substantial improvement of dispersion properties, in particular for the case $\Delta x = 1.5h$ and wavelengths around $6h - 8h$. For the shortest waves, that may be resolved for each Δx, the gain is less significant, in particular regarding the group velocity. On the other hand, when the exact dispersion relation is considered (from full potential theory), the graphs indicate that results for $\Delta\hat{x} = 0.7h$ is as good as the exact optimized Boussinesq equations.

3.5.4 Relation to the FUNWAVE/COULWAVE methods

The numerical methods in both the FUNWAVE models, as well as the COULWAVE model, differ from the one presented herein with respect to the time integration method. Moreover, the FUNWAVE 1 and COULWAVE models are non-staggered in space. On the other hand, Shi et al. [40] redesigned the FUNWAVE model to include curvilinear coordinates and changed to the spatially staggered C-grid, which is the same as is used herein (and in numerous other wave models). They reported improved performance as compared to the non-staggered method in relation to noise generation. All FUNWAVE and COULWAVE models employ a temporal fourth order Adam-Bashforth-Moulton scheme with a third order Adam-Bashforth predictor step and a fourth order implicit Adam-Moulton corrector step. To achieve a simple comparison between the numerical dispersion properties of these methods and that presented herein we will

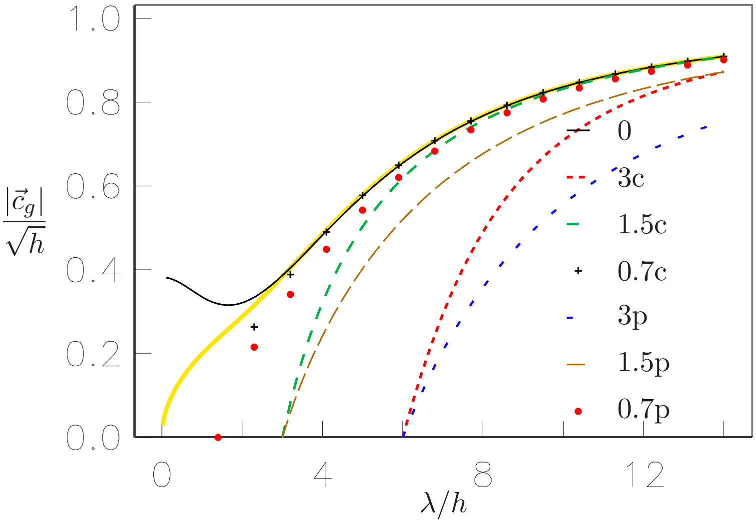

Figure 10: Group speed for the Boussinesq equations with $\gamma = -0.057$ and direction of wave advance $\theta = 0°$. The curves are labelled by $\Delta\hat{x}/h$ together with "c" and "p" for corrected and uncorrected numerical methods, respectively, expect for full potential theory that is depicted in bold yellow. The time step is $\Delta t = \frac{1}{2}h^{-\frac{1}{2}}\Delta\hat{x}$ and $f_c = f_m = 0$.

assume plane waves and exact time integration, which corresponds to $\Delta t \to 0$. However, for comparison also results with a finite Courant number, $C = \sqrt{h}\Delta t/\Delta x$ will be presented for our own method.

The spatial relationship between the FUNWAVE 2 method and the present one is swiftly established. From (28) the difference formula in [40] for the gradient terms of order ϵ^0, μ^0 immediately follows

$$\left[\frac{\partial u}{\partial x}\right]_{i+\frac{1}{2}} + O(\Delta x^4) = \left[\delta_x \overline{u}^x - \frac{\Delta x^2}{24}\delta_x^3 \overline{u}^x\right]_{i+\frac{1}{2}} = \frac{1}{24\Delta x}\{(u_{i+2} - 27u_{i+1} + 27u_i - u_{i-1})\}. \quad (45)$$

Using this expression for the leading spatial derivatives in the Nwogu's equations (simplified from (80) and (81)), while employing centered, second order differences elsewhere, we obtain a set of differential/difference equations akin to (42) and (43) with the correction alternative $f_m = 1$ and (40). Since $\Delta t \to 0$ the other factor, f_c, is aribitrary. In terms of the the discrete unknowns $\eta(t)_{i+\frac{1}{2}}$ and $u(t)_i$, where the t is kept due to the assumption of exact time integration, the equations read

$$\left[\dot{\eta} = -h\delta_x u + h\{\frac{\Delta x^2}{24} - \mu^2(\frac{1}{2}z_\alpha^2 + z_\alpha h + \frac{1}{3}h^2)\}\delta_x^3 u\right]_{i+\frac{1}{2}}, \quad (46)$$

$$\left[\dot{u} = -\delta_x \eta + \frac{\Delta x^2}{24}\delta_x^3 \eta - \mu^2(\frac{1}{2}z_\alpha^2 + z_\alpha h)\delta_x^2 \dot{u}\right]_i, \quad (47)$$

where the dots indicate temporal differentiation. When comparing these equations to (42) and (43) the δ_t in these equations must be replaced by dots because we are now considering the limit of vanishing Δt. Provided that the relation (92) between z_α and γ holds the differential equations of Nwogu and the standard formulation yield identical dispersion relations. In the discrete case, even with correction terms, this still holds and the dispersion relation of (46) and (47) is identical to (44) with $f_m = 1$ and $\Delta t \to 0$. The latter corresponds to $\tilde{\omega} \to \omega$.

Next, we derive the principal spatial discretization of FUNWAVE 1 and COULWAVE in the present context and notation. For a non-staggered grid we have the discrete unknowns $\eta(t)_i$ and $u(t)_i$. The basic differential/difference equations for the LSW equations then become

$$[\dot{\eta} = -h\delta_x \overline{u}^x]_i\,, \quad [\dot{u} = -\delta_x \overline{\eta}^x]_i\,. \tag{48}$$

We observe that the discrete quantities are divided into two uncoupled families, namely odd η nodes plus even u nodes and even η nodes plus odd u nodes. Comparing to the corresponding equations consistent with the uncorrected (16) and (17) we realize that in (48) we solve the same equation twice, with the same method, but with a doubled space increment. The non-staggered method then gives four times as large discretization errors for a comparable use of computer resources (CPU time and memory). In addition the non-staggered method is more susceptible to noise if the two families are combined by, for instance, nonlinear terms. As it is, (48) is indeed a poor scheme and amendments are needed[9]. Since the leading error in the spatial differences is now simply increased by a factor 4 compared to (28) we obtain

$$\delta_x \overline{u}^x = \frac{\partial u}{\partial x} + \frac{1}{6}\Delta x^2 \frac{\partial^3 u}{\partial x^3} + O(\Delta x^4).$$

In accordance with the preceding subsections we then obtain the corrected difference presentation

$$\left[\frac{\partial u}{\partial x}\right]_i + O(\Delta x^4) = \left[\delta_x \overline{u}^x - \frac{\Delta x^2}{6}\delta_x^3 \overline{u}^x\right]_i = \frac{1}{12\Delta x}\{8(u_{i+1} - u_{i-1}) - (u_{i+2} - u_{i-2})\}. \tag{49}$$

The leftmost expression is the one applied in [15] for internal points. However, the expression in the middle is better suited for calculation of discrete dispersion relations and we will stick to that.

For constant depth, and linear plane waves, the discrete versions of (80) and (81) now read

$$\dot{\eta} = -h\delta_x \overline{u}^x + h\{\frac{\Delta x^2}{6} - \mu^2(\frac{1}{2}z_\alpha^2 + z_\alpha h + \frac{1}{3}h^2)\}\delta_x^3 \overline{u}^x, \tag{50}$$

$$\dot{u} = -\delta_x \overline{\eta}^x + \frac{\Delta x^2}{6}\delta_x^3 \overline{\eta}^x - \mu^2(\frac{1}{2}z_\alpha^2 + z_\alpha h)\delta_x^2 \dot{u}, \tag{51}$$

where the dot indicates temporal differentiation and the common index k has been omitted. The derivation of the numerical dispersion relation is now straightforward

$$\omega^2 = \frac{h\tilde{k}^2(1 + \{\frac{\Delta x^2}{6} - \mu^2(\frac{1}{2}z_\alpha^2 + z_\alpha h + \frac{1}{3}h^2)\}\tilde{k}^2)\tilde{c}_x^2(1 + \frac{\Delta x^2}{6}\tilde{k}^2)}{1 - \mu^2(\frac{1}{2}z_\alpha^2 + z_\alpha h)\tilde{k}^2}. \tag{52}$$

It is stressed that this dispersion relation is based on exact temporal integration and it will thus apply to the FUNWAVE 1 and COULWAVE models only in the limit $\Delta t \to 0$. For finite Δt these models will yield, for instance, a small damping corresponding to an imaginary part in ω.

---

[9] The a possible reason for the choice of non-staggered grid in FUNWAVE 1 and COULWAVE may be a simpler discretization of higher order nonlinear terms.

Provided $\gamma = \frac{1}{3} + \frac{z_\alpha}{h} + \frac{1}{2}\frac{z_\alpha^2}{h^2}$, Nwogu's formulation, which is the basis of the model (50), (51) and the improved standard model are equivalent (see section A.3). Hence, we may compare the errors relative to the analytical dispersion from (52) to that of (44) with $\Delta t = 0$. To keep it simple we employ only the correction terms according to $f_m = 0$ in this comparison. As will be evident below, the deviations between the different corrected C-grid methods, including the one corresponding to FUNWAVE 2, will be much smaller than the deviation between any of them and the non-staggered method. Denoting the errors in phase and group velocity with Δc and Δc_g, respectively, we obtain the results in figure 11. For the same Δx the corrected standard model performs substantially better than the non-staggered FUNWAVE 1/COULWAVE formulation. In fact, also for the corrected models, with dispersion, the non-staggered version is similar to the staggered one with twice the grid size. Naturally, the temporal errors may change the picture somewhat, as shown below. Still, the non-staggered method must be reckoned as somewhat inferior to the the staggered methods.

In figure 12 we have compared the version of the numerical correction implemented in our "standard" model ($f_m = 0$) to the correction method that corresponds to the FUNWAVE 2 model ($f_m = 1$). The methods are rather similar, but $f_m = 1$ yields somewhat better results for the coarse grid $\Delta\hat{x} = 1.2h$, while $f_m = 0$ is a little better for the finer grid increment $\Delta\hat{x} = 0.6h$, for which the choice $f_m = 1$ overshoots the wave celerity slightly. For the finest grid, $\Delta\hat{x} = 0.3h$, both options are too good in the sense that they follow the analytic behaviour too long in relation to the deviation from full potential theory. This and preceding results of this subsection indicate that there is no point in applying a grid finer than $\Delta\hat{x} = 0.6h$, say, but it must be emphasized that the results are obtained without nonlinearity and variable depth.

In the figures 13 and 14 results are displayed for different values of the Courant number $C = \sqrt{h}\Delta t/\Delta\hat{x}$. It turns out that the value of f_c does not significantly affect the wave celerity. Therefore, this parameter is not varied in the graphs. For $C = 0.5$ the results are very similar to those for $C = 0$, which correspond to figure 12; the spatial errors still dominate. For $\Delta\hat{x} = 0.6h$ and $C = 1$ we observe that the performance with $f_m = 0$ has become slightly poorer, while the performance with f_m has improved in relation to $C = 1$ (the overshoot has nearly vanished). However, in tsunami simulations C is non-constant and presumably much less than unity in large regions. Hence, no clear ranking of the different options for the corrections terms presents itself.

3.5.5 Corrected depths

In (25) depths values at the u and v nodes were introduced as $h^{(u)}$ and $h^{(v)}$ respectively. To obtain formal fourth order accuracy in the leading balance of the discrete equations (linear hydrostatic) we cannot employ the simple mid point formulas $h^{(u)} = \overline{h}^x$ and $h^{(v)} = \overline{h}^y$. We may readily identify two methods for amendment

1. Accurate values for $h^{(u)}$ and $h^{(v)}$ may be obtained from depth functions or bathymetric databases in the first place. Inspection of the discrete equations readily reveals that the discrete depth is always invoked at a velocity node. Hence, at the cost of an extra discrete field we may employ $\{h^{(u)}_{i,j+\frac{1}{2}}\}$ and $\{h^{(v)}_{i+\frac{1}{2},j}\}$ as depth matrices instead of $\{h_{i+\frac{1}{2},j+\frac{1}{2}}\}$. Since a few extra matrices, in addition to those of the field variables, are anyway needed due to the iteration this implies only a modest relative increase in the memory requirements, while the discrete expressions are moderately simplified. For academic problems with a

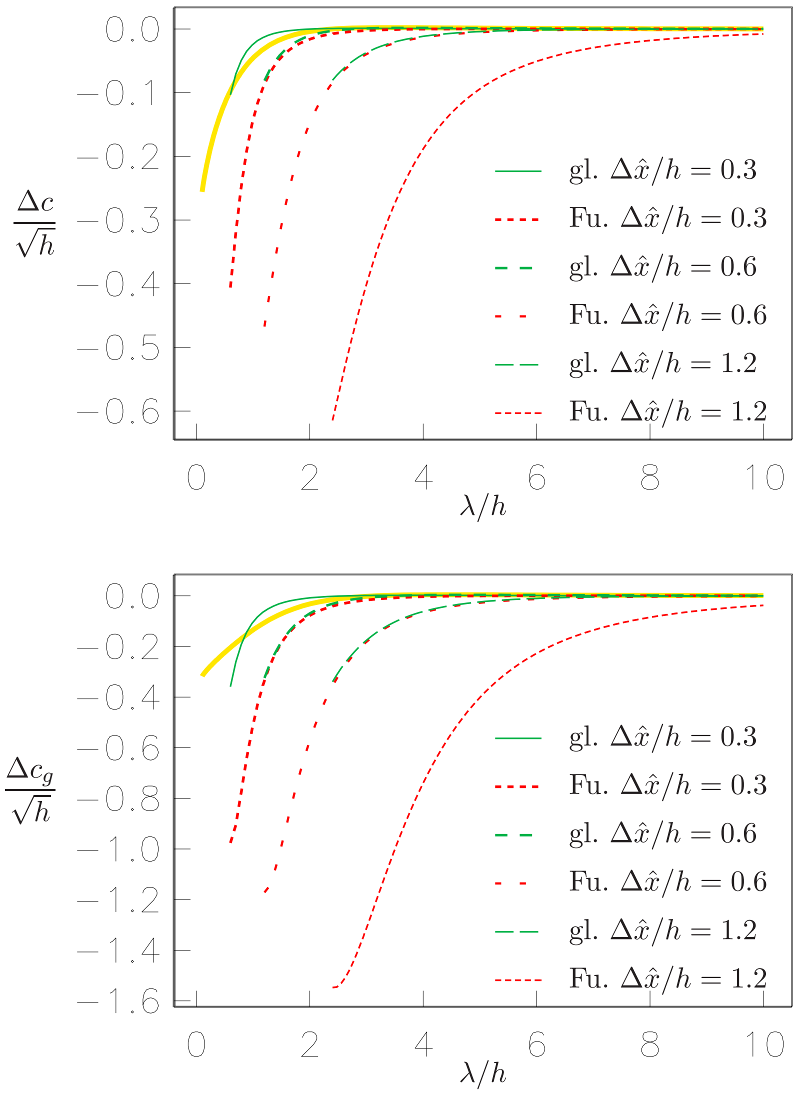

Figure 11: Numerical error in c and c_g for the present method with $f_m = 0$ (gl.) and the Funwave 1 (Fu.) method in the limit $\Delta t \rightarrow 0$. The bold yellow line marks the difference in wave celerity between full potential theory and the optimized Boussinesq equations.

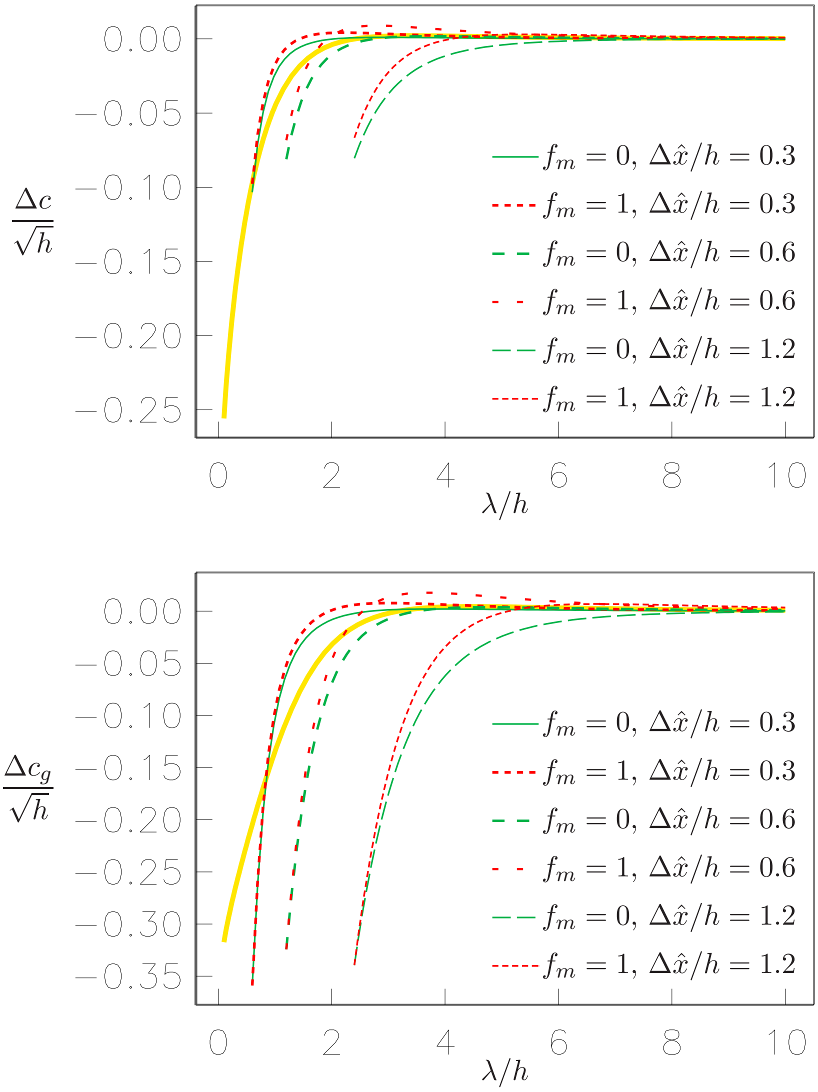

Figure 12: Numerical error in c and c_g for two different correction schemes, corresponding to $f_m = 1$ and $f_m = 0$, in the limit $\Delta t \rightarrow 0$. The bold yellow line marks the difference in wave celerity between full potential theory and the optimized Boussinesq equations.

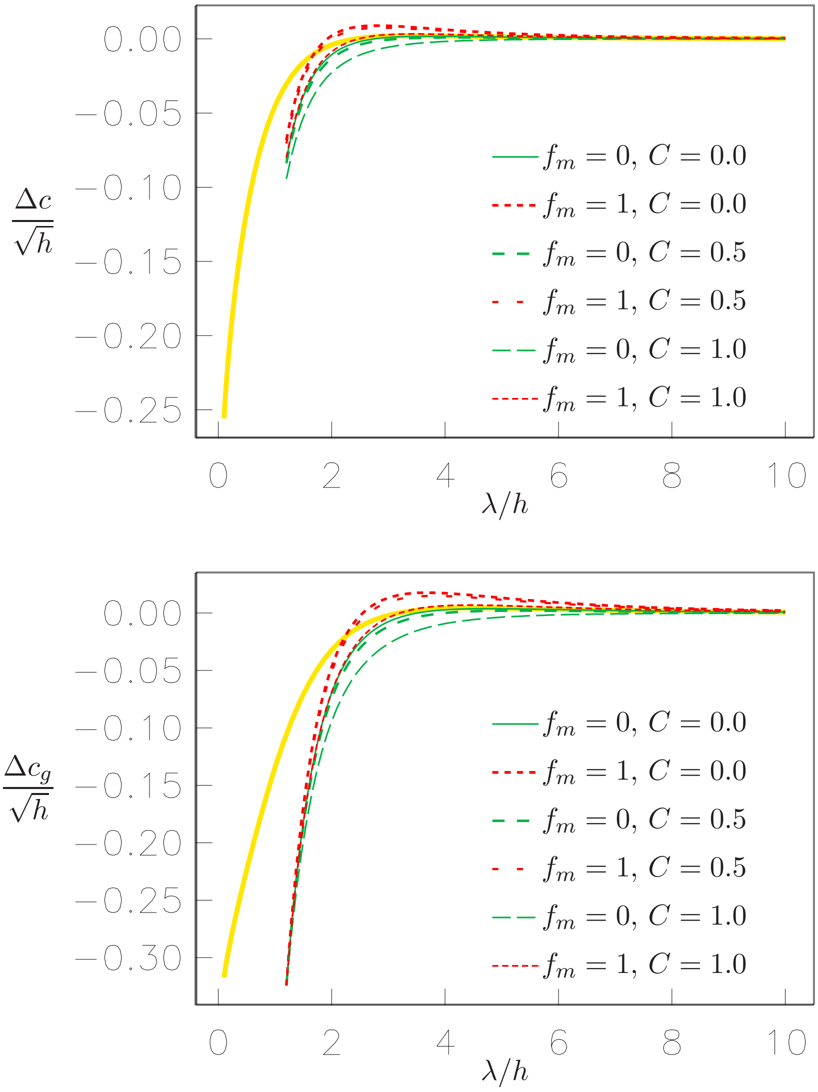

Figure 13: Dependene of numerical errors on the Courant number for $\Delta\hat{x} = 0.6$ and $f_c = 0$. The bold yellow line marks the difference in wave celerity between full potential theory and the optimized Boussinesq equations.

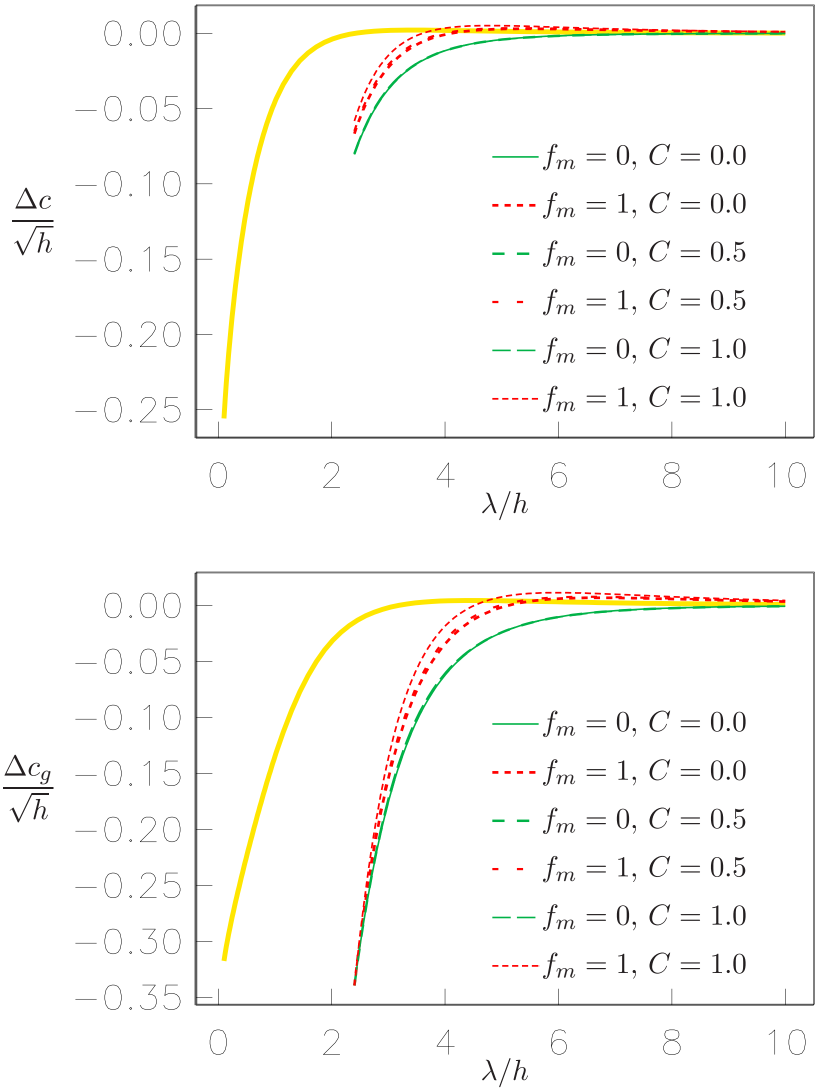

Figure 14: Dependene of numerical errors on the Courant number for $\Delta\hat{x} = 1.2$ and $f_c = 0$. The bold yellow line marks the difference in wave celerity between full potential theory and the optimized Boussinesq equations.

given smooth formula for the depth it may indeed be worthwhile employing the double depth matrix. However, for measured bathymetries the data are generally inaccurate in the first place and the gain is less certain.

2. We may keep the depth matrix defined at the semi-integral η nodes, but employ a more accurate interpolation than mid-point averaging. A four point interpolation may yield the fourth order representation

$$h_j^{(u)} = \frac{9}{16}\overline{h}^x_j - \frac{1}{16}(h_{j-\frac{3}{2}} + h_{j+\frac{3}{2}}) + O(\Delta x^4) = [\overline{h}^x - \frac{\Delta x^2}{8}\delta_x^2\overline{h}^x]_j + O(\Delta x^4), \tag{53}$$

   where the common second index is implicit and a corresponding formula applies at the v nodes. Naturally, (53) is advantageous only in the principal flux terms in the equation of continuity; elsewhere the second order formula $h^{(u)} = \overline{h}^x$ can be used without any expected loss of accuracy. At the boundaries asymmetric formulas may be employed. If $j = 0$ is a boundary, a third order relation is defined in analogy to (53)

$$h_0^{(u)} = \overline{h}^x_0 - \frac{\Delta x^2}{8}\delta_x^2 h_{\frac{1}{2}} + O(\Delta x^3), \tag{54}$$

   where we have exploited the availability of $h_{-\frac{1}{2}}$. A fourth order formula may naturally be obtained, but in a more lengthy form. Also the higher order interpolation formulas will generally be less useful for a measured bathymetry.

Both the proposed methods will work well when the depth is accurately known, such as in problems with idealized geometries. When bathymetric data, such as ETOPO 2 min. grids, are employed the application of corrected depths seems futile. On the other hand, in the example of section 5 we will observe that the numerical correction terms really improve the results even though the parts related to corrected depths are left out.

3.6 Iteration procedures

3.6.1 The continuity equation

In the nonlinear case the discrete equation of continuity (16) yields an implicit set of equations for the new surface elevations. The equation set is strongly diagonal dominant as long as $\epsilon r_y u\Delta t \ll \Delta x$ and $\epsilon v\Delta t \ll \Delta y$. This implies that the particle motion during a time step is much smaller than the grid increment. Assuming a Courant number of order unity we may also interpret the requirements as the particle velocity being much less than the phase and group velocities. Collecting all implicit terms of (16) on the left hand side we obtain

$$\frac{1}{\Delta t}\eta + \epsilon\frac{r_y}{2}\left\{\delta_x(\overline{\eta}^x u) + \delta_y(c_v\overline{\eta}^y v)\right\} = R, \tag{55}$$

where the indices are implicit and R contains all the contributions of times less than $(k+1)\Delta t$.

Due to the diagonal dominant structure a point by point method is applicable. Carrying out iteration number $p+1$ then corresponds to computing

$$\frac{1}{\Delta t}\eta^{p+1} = -\epsilon\frac{r_y}{2}\left\{\delta_x(\overline{\eta^p}^x u) + \delta_y(c_v\overline{\eta^p}^x v)\right\} + R, \tag{56}$$

where the superscripts now count iteration level and not time step. In the limit $p \to \infty$ the quantity η^p should then approach $\eta^{(k+1)}$. The rule (56) corresponds to a Jacobi iteration. Application of a Gauss-Seidel like approach is not recommended because it will violate exact volume conservation.

The error after p iterations, denoted as $\nu^p = \eta^{(k+1)} - \eta^p$, will fulfill the same equation as η^p, namely (56), with $R = 0$. To obtain an indication of the efficiency and stability of the Jacobi iteration we set map factors and velocities to constant values and assume

$$\nu^p = \hat{\nu}\beta^p e^{i(k\hat{x}+\ell y)}. \tag{57}$$

It is noted that Cartesian-like longitudinal coordinate $\hat{x}$ is used here and throughout this subsection. The homogeneous counterpart to (56) then implies

$$\beta = -i\epsilon\frac{1}{2}\Delta t(u\tilde{c}_x\tilde{k} + v\tilde{c}_y\tilde{\ell}). \tag{58}$$

A sufficient stability criterion then reads

$$|\beta| \leq \epsilon\frac{1}{2}\Delta t\left(\frac{|u|}{\Delta\hat{x}} + \frac{|v|}{\Delta y}\right) < 1. \tag{59}$$

We observe that the iteration is stable when the fluid particles cover well below a spatial grid increment in a time step. For velocities of order one tenth of the phase speed ($\epsilon = 0.1$) and wavelengths around six times the depth β becomes approximately 0.1.

We may also apply a line by line implicit method

$$\frac{1}{\Delta t}\eta^{p+\frac{1}{2}} + \epsilon\frac{r_y}{2}\delta_x(\overline{\eta^{p+\frac{1}{2}}}^x u) = -\epsilon\frac{r_y}{2}\delta_y(\overline{\eta^p}^y v) + R, \tag{60}$$

$$\frac{1}{\Delta t}\eta^{p+1} + \epsilon\frac{r_y}{2}\delta_y(\overline{\eta^{p+1}}^y v) = -\epsilon\frac{r_y}{2}\delta_x(\overline{\eta^{p+\frac{1}{2}}}^x u) + R. \tag{61}$$

We observe that each of the two half iterations involve the solution of a series of tri-diagonal equations. Substitution of constant values for the velocity and assumption of the form (57) for the error now yield

$$\beta = \frac{-\epsilon^2\Delta t^2\tilde{c}_x\tilde{c}_y\tilde{k}\tilde{\ell}uv}{4\left(1 - \frac{1}{2}i\epsilon u\tilde{c}_x\tilde{k}\right)\left(1 - \frac{1}{2}i\epsilon v\tilde{c}_y\tilde{\ell}\right)}. \tag{62}$$

Bearing in mind that this value is the result of two half-steps, while the factor in (58) arises from a single step, the line by line and Jacobi method display similar convergence rates for small amplitudes. For large amplitudes, on the other hand, the line by line iteration is markedly better and, above all, it is stable. Hence, the line by line approach is preferred, even though it is computationally more demanding.

3.6.2 The momentum equation

Due to the reciprocals of grid increments the discrete momentum equations display larger off-diagonal entries in the coefficient matrix[10] and are thus not well suited for a point-wise iteration scheme. Instead a line by line approach is modified from [27, 36]. In these references we have

---

[10] Such a matrix do of course exist in principle, but it is never explicitly assembled in the software.

equations of the Helmholtz type for either a velocity potential or the velocity components. For all equation-sets we then do alternate implicit sweeps in the x and y directions. In the present case we alternate by implicit sweeps along the x axis for the x component and sweeps along the y axis for the y component. In comparison to [36] we do only half the number of sweeps, without any degradation of the convergence in the linear case, as shown below. The iteration is very similar to the one used in [2].

In relation to the dispersion terms it is simplest to solve (17), and the corresponding y component, in terms of local accelerations rather than velocities. When velocities and surface elevations are computed up to, and including, $t = k\Delta t$ we thus seek values for

$$[\dot{u} \equiv \delta_t u]^{(k)}_{i,j+\frac{1}{2}}, \quad [\dot{v} \equiv \delta_t v]^{(k)}_{i+\frac{1}{2},j}.$$

Advancing from iteration level p to $p+1$ we first solve the sequence of tridiagonal equations given by

$$\begin{aligned} \dot{u}^{p+1} + \epsilon \hat{T}_x \quad = \quad & R_x + \tfrac{\Delta t}{2} f_u \overline{\dot{v}^p}^{xyt} \\ & + \left(\tfrac{\mu^2}{2} \overline{h}^x + \tfrac{I_k}{24} \Delta t^2 \right) (\overline{r_y}^x)^2 \delta_x \{ \delta_x (\overline{h}^x \dot{u}^{p+1}) + \delta_y (c_v \overline{h}^y \dot{v}^p) \} \\ & - \left(\mu^2 (\tfrac{1}{6} + \gamma)(\overline{h}^x)^2 (\overline{r_y}^x)^2 + \tfrac{I_k}{24} \Delta x^2 \right) \delta_x^2 \dot{u}^{p+1} \\ & - \mu^2 (\tfrac{1}{6} + \gamma)(\overline{h}^x)^2 (\overline{r_y}^x)^2 \delta_x \delta_y (c_v \dot{v}^p), \end{aligned} \tag{63}$$

where R_x contains all explicit contributions, $I_k = 1$ corresponds to the corrected numerical method, with $f_c = f_m = 0$, and

$$\hat{T}_x = \frac{1}{2} \Delta t \{ \overline{r_y}^x \delta_x \{ (\overline{u}^x \overline{\dot{u}^{p+1}}^x) \} + \overline{(\overline{v}^x \delta_y \dot{u}^p + \overline{\dot{v}^p}^x \delta_y u)}^y \}. \tag{64}$$

The velocities in this expression are the ones evaluated at $t = (k - \frac{1}{2})\Delta t$. Then we substitute $\dot{u}^{p+1}$ for $\dot{u}$ in the y component and solve a corresponding sequence of tri-diagonal equations for $\dot{v}^{p+1}$.

To simplify the matters we analyze the cases $\epsilon \neq 0,\ \mu = 0$ and $\epsilon = 0,\ \mu \neq 0$ separately. In the first case we assume constants values for v and u, but not[11] for $\delta_x \dot{u}$, in the x-component of the momentum equation. For the deviation from the exact discrete solution and the value after p iterations we write $\nu^p = \dot{u}^{(k)} - \dot{u}^p$. Again, we invoke the expression (57) and obtain

$$\beta = \frac{-\frac{i\epsilon\Delta t}{2} \tilde{c}_y \tilde{\ell} v}{1 + \frac{i\epsilon\Delta t}{2} \tilde{c}_x \tilde{k} u},$$

which implies

$$|\beta| \leq \frac{\epsilon \Delta t}{2\Delta y} |v|.$$

Performance and stability is similar to the corresponding properties of the point-wise iteration for the equation of continuity. A corresponding behavior is naturally found for the y-component.

---

[11] In principle an inconsistent assumption, but such simplifications are still commonly used in assessments and analysis of methods.

For $\epsilon = 0$, $\mu \neq 0$ the iterations on the two components of the momentum equations are coupled. As before we analyze equations with constant coefficients, which may be obtained by assuming constant depth ($h = 1$) and constant map factors. Again introducing the deviations

$$\nu^p = \dot{u}^{(k)} - \dot{u}^p, \quad \zeta^p = \dot{v}^{(k)} - \dot{v}^p,$$

we find the equations

$$\begin{aligned}
&[\nu - \{(\tfrac{1}{3} - \gamma)\mu^2 + \tfrac{I_k}{24}(\Delta t^2 - \Delta x^2)\}\delta_x^2 \nu]^{p+1} + [-\{(\tfrac{1}{3} - \gamma)\mu^2 + \tfrac{I_k}{24}\Delta t^2\}\delta_x\delta_y\zeta - \tfrac{\Delta t}{2} f \overline{\zeta}^{xy}]^p = 0, \\
&[\zeta - \{(\tfrac{1}{3} - \gamma)\mu^2 + \tfrac{I_k}{24}(\Delta t^2 - \Delta y^2)\}\delta_y^2 \zeta]^{p+1} + [-\{(\tfrac{1}{3} - \gamma)\mu^2 + \tfrac{I_k}{24}\Delta t^2\}\delta_x\delta_y\nu + \tfrac{\Delta t}{2} \overline{\nu}^{xy}]^{p+1} = 0.
\end{aligned}$$

Now we separate variables according to

$$\begin{pmatrix} \nu^p \\ \zeta^p \end{pmatrix} = \begin{pmatrix} \hat{\nu} \\ \hat{\zeta} \end{pmatrix} \beta^p e^{i(k\hat{x} + \ell y)},$$

and find that β may attain the values 0 and

$$\beta = \frac{\{(\tfrac{1}{3} - \gamma)\mu^2 + \tfrac{I_k}{24}\Delta t^2\}^2 \tilde{k}^2 \tilde{\ell}^2 - \tfrac{\Delta t^2}{4} f^2 \tilde{c}_x^2 \tilde{c}_y^2}{\left(1 + \{(\tfrac{1}{3} - \gamma)\mu^2 + \tfrac{I_k}{24}(\Delta t^2 - \Delta x^2)\}\tilde{k}^2\right)\left(1 + \{(\tfrac{1}{3} - \gamma)\mu^2 + \tfrac{I_k}{24}(\Delta t^2 - \Delta y^2)\}\tilde{\ell}^2\right)}. \tag{65}$$

A closer investigation of the equations for ν^p and ζ^p reveals that the occurrence of $\beta = 0$ is linked to the fact that no start value for ν^p is involved since ν^0 do not appear in any of the equations. The start value for $\dot{v}$ may be the values from the previous time step yielding $\zeta^0 = \hat{\zeta} = O(\Delta t)$. This gives

$$\hat{\nu} = \frac{1 + \{(\tfrac{1}{3} - \gamma)\mu^2 + \tfrac{I_k}{24}(\Delta t^2 - \Delta y^2)\}\tilde{\ell}^2}{\{(\tfrac{1}{3} - \gamma)\mu^2 + \tfrac{I_k}{24}\Delta t^2\}\tilde{k}\tilde{\ell} + \tfrac{\Delta t}{2} f \tilde{c}_x \tilde{c}_y}\hat{\zeta}.$$

For long waves $\hat{\nu}$ may be large. However, this is not a real problem since the first ν value to appear, namely $\nu_1 = \beta\hat{\nu}$, still becomes small.

The iteration is always stable for $f = 0$ and stable provided $f\Delta t < \frac{1}{2}$ otherwise. For long wave components we observe a very fast convergence, but the presence of shorter components slow down the convergence. Then, a remedy may be the inclusion of a shift, such as is used in [36]. However, in the present context it is much more difficult to find the useful employment of the shift than in the formulation of the reference. Hence, we omit this topic herein.

3.7 Possible instabilities from bottom gradients

A sequence of Boussinesq type equations were studied by [41] with respect to instabilities due to variable depth. The standard formulation, which corresponds to the one used herein with $\gamma = f = 0$, was invariably stable. All other investigated formulations displayed linear instabilities. Among these potentially unstable formulations was that of Nwogu which is given by (80) and (81) without the nonlinearities and the ad-hoc terms. However, we emphasis that Nwogu's formulation was among the better ones with respect to instability and that it should be applicable to a variety of cases where no such stability problem is likely to occur.

Hence, the basic method herein, without corrected dispersion and numerics, it is already demonstrated to be stable by the reference [41]. Still, we need to investigate the stability properties when non-zero γ and numerical correction terms, such as $\mathcal{A}$ and $\mathcal{B}$, are included.

Details on the procedure of the stability analysis are given in [41], and we will recall only some key points below. For linear equations and wave advance parallel to the x-axis there exist solutions on the form

$$\eta(x,t) = \hat{\eta}(x)e^{i\omega t}, \quad u(x,t) = \hat{u}(x)e^{i\omega t}. \tag{66}$$

The quantity ω may be real or complex and will generally be found from an eigenvalue problem. In the linearized Boussinesq equations the introduction of (66) will simply correspond to $\partial u/\partial t \to i\omega\hat{u}$ etc. For the discrete equations ω is replaced by $\tilde{\omega} = 2\sin(\frac{1}{2}\omega\Delta t)/\Delta t$, in the same manner as in the dispersion relation (19) etc.

We assume wave advance parallel to the x-axis, $\epsilon = 0$, uniform map factors, and introduce once again the Cartesian longitudinal coordinate $\hat{x}$. Omitting the hat over the x we obtain the discrete continuity equation

$$[i\tilde{\omega}\hat{\eta} = -\delta_x(\overline{h}^x\hat{u} + \hat{\mathcal{A}})]_{j+1/2}, \tag{67}$$

where the common temporal factor is removed and the corresponding linear discrete momentum equation

$$[i\tilde{\omega}\hat{u} = -\delta_x\hat{\eta} - \gamma\mu^2\delta_x^3\hat{\eta} + i\tilde{\omega}\frac{\mu^2}{2}\overline{h}^x\delta_x^2(\overline{h}^x\hat{u}) - i\tilde{\omega}\mu^2(\overline{h}^x)^2(\frac{1}{6}+\gamma)\delta_x^2\hat{u} + \hat{\mathcal{B}}]_j. \tag{68}$$

Next, the surface elevation is eliminated by substituting the right hand side expression in equation (67) into (68). Spelling out the expressions for the correction terms ($f_m = f_c = 0$), we find a single equation for the velocity profile

$$\begin{aligned}&(1+\gamma\mu^2\delta_x^2)\left(\delta_x^2(\overline{h}^x\hat{u}) + \tfrac{I_k}{24}\delta_x^2[(\Delta t^2\overline{h}^x - \Delta x^2)\delta_x^2(\overline{h}^x\hat{u})]\right) + \\ &\tilde{\omega}^2\left(\hat{u} - \tfrac{\mu^2}{2}\overline{h}^x\delta_x^2(\overline{h}^x\hat{u}) + \mu^2(\tfrac{1}{6}+\gamma)(\overline{h}^x)^2\delta_x^2\hat{u} - \tfrac{1}{24}[\Delta t^2\delta_x^2(\overline{h}^x\hat{u}) - \Delta x^2\delta_x^2\hat{u}]\right) = 0,\end{aligned} \tag{69}$$

where I_k is as defined below (63). When applied in closed basins of variable depth with symmetric no-flux conditions for $\hat{u}$ at the side walls, we obtain a generalized eigenvalue problem on the form

$$(\mathbb{A} + \tilde{\omega}^2\mathbb{B})\mathbf{u} = 0, \tag{70}$$

where $\mathbb{A}$ and $\mathbb{B}$ are banded coefficient matrices and $\mathbf{u}$ is the velocity eigenvector containing the nodal values of $\hat{u}$. The method for solving (70) numerically is given in [41].

We then investigate a few simple types of basins. One such geometry is the step-shelf, which is a basin with one part of constant unitary depth and one part of constant depth h_m between 0 and 1, separated with one grid point only. Another is the spike, which is one grid point of depth h_m, and otherwise unitary depth. More details on these depth configurations are given in [41].

In the chosen configurations we systematically scan through combinations of Δx and h_{min}, the minimum depth, searching for the occurrence of complex $\tilde{\omega}$. When complex $\tilde{\omega}$ are found, the unstable modes are inserted into an numerical model, integrated in the time domain, to validate that the complex frequency is correct and that exponential growth is actually taking place. The eigenvalue method is also validated by insertion of the reconstructed solution from (66) in the time dependent equation and computation of the residuals.

In [41], no unstable modes were found for the standard formulation without correction terms ($I_k = \gamma = 0$). Introduction of the numerical correction terms only ($I_k = 1$), does not lead to discovery of any unstable modes. By also including the dispersion optimisation terms $\gamma = -0.057$, we find unstable modes for the step-shelf (figure 15), but not for the spike geometry.

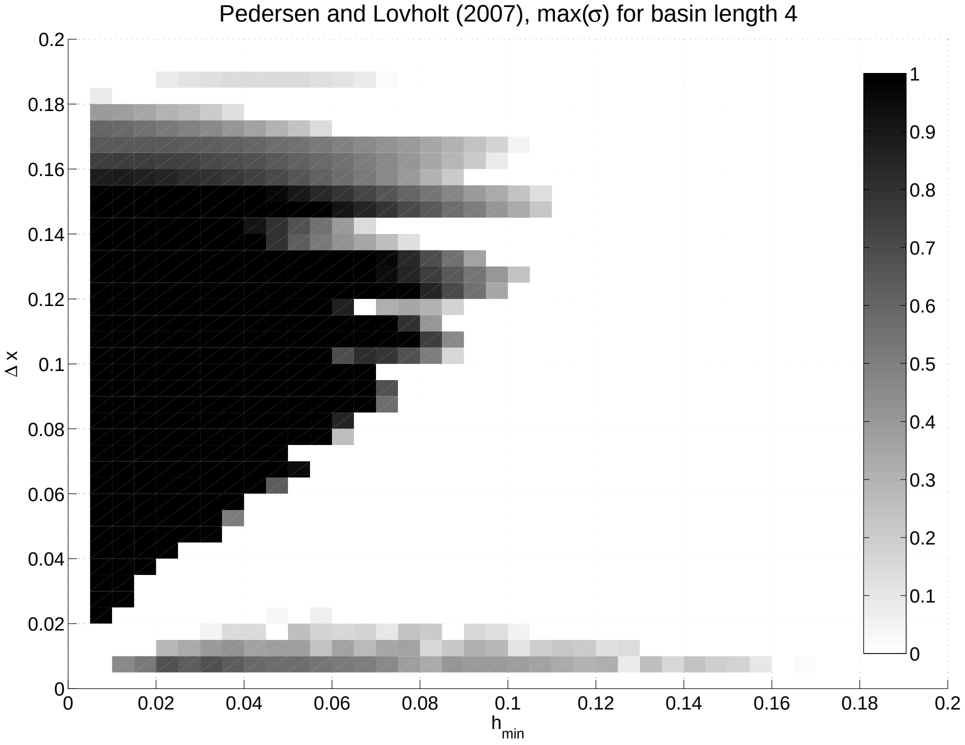

Figure 15: Stability limits for the optimized set in a step shelf geometry. The colour-bar indicates the growth rates for the unstable modes (complex values in ω).

Setting $I_k = 0$ and and keeping the optimisation terms we find no change the stability limits. Hence, the unstable modes are related to the γ term alone, and not to the combination of optimization and numerical correction terms. The unstable modes are related to very steep depth gradients as shown in figure 15. The stability limits are comparable to the ones found for the Nwogu formulation [23], i.e. they occur for small values of Δx and h_{min}. Such small values may of course be encountered in discretization of real bathymetries, but this is presumably rare.

3.8 Conventions for enumeration and coding

The momentum equations are written in a generic manner for to sweeps in either the x or y direction. Denoting the implicit direction by s, the other direction by n and the corresponding velocity components by U and V, respectively, we enumerate a computational molecule as shown in figure 16. All fields are stored as one-dimensional arrays and increments in the s and

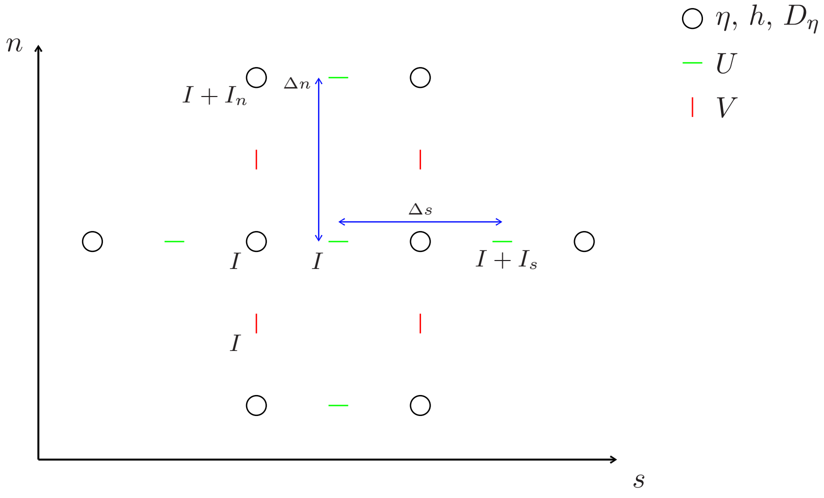

Figure 16: Computational molecule centered at point I in generic enumeration as explained in the text.

	I_s	I_n	γ_s	γ_n	κ_1	κ_2	$\hat{f}$	Δs	Δn
$s = x\ (\psi)$	1	$n+2$	$\frac{1}{c_\phi}$	1	1	c_ϕ	$-f$	Δx	Δy
$s = y\ (\phi)$	$n+2$	1	1	$\frac{1}{c_\phi}$	c_ϕ	1	f	Δy	Δx

Table 1: Values of coefficients for sweeps in x and y directions.

n directions are defined as I_n and I_s, respectively.

$$\begin{aligned}\frac{\partial U}{\partial t} + \epsilon\left(\gamma_s U \frac{\partial U}{\partial s} + \gamma_n V \frac{\partial U}{\partial n}\right) \quad = \quad & -\gamma_s \frac{\partial \eta}{\partial s} + \hat{f} V - \gamma \mu^2 h^2 \gamma_s \frac{\partial D_\eta}{\partial s} \\ & + \left(\frac{\mu^2}{2} h + \frac{I_k \Delta t^2}{24}\right) \gamma_s \frac{\partial}{\partial s} \left[\frac{1}{c_\phi} \frac{\partial}{\partial s} \left(\kappa_1 h \frac{\partial U}{\partial t}\right) + \frac{1}{c_\phi} \frac{\partial}{\partial n} \left(\kappa_2 h \frac{\partial V}{\partial t}\right)\right] \\ & - \left(\mu^2 (\tfrac{1}{6} + \gamma) h^2 \gamma_s + \frac{I_k \Delta s^2}{24} \kappa_2\right) \frac{\partial}{\partial s} \left[\frac{1}{c_\phi} \frac{\partial}{\partial s} \left(\kappa_1 \frac{\partial U}{\partial t}\right)\right]. \\ & - \mu^2 (\tfrac{1}{6} + \gamma) h^2 \gamma_s \frac{\partial}{\partial s} \left[\frac{1}{c_\phi} \frac{\partial}{\partial n} \left(\kappa_2 \frac{\partial V}{\partial t}\right)\right].\end{aligned} \qquad (71)$$

The coefficient I_k is unity if numerical corrections are included, 0 otherwise, while the other coefficients are defined in table 1. A corresponding convention is suited for implicit sweeps in the equation of continuity.

4 Test problems

In the present section we employ a scaling with h_0 as both the vertical and the horizontal scaling factor. This scaling is discussed at the end of section 2.3.

4.1 Numerical errors in an asymptotic wave-front

A classic problem in wave theory is that of evolution from an initially confined surface elevation (the Poisson-Cauchy problem). In finite depth one of the features of the solution is an asymptotic wave front, described by an Airy function, that slowly stretches and attenuates. The standard solution procedure is the Fourier transform, which can be applied also in the discrete case with a cut-off wave number equal to $\pi/\Delta\hat{x}$. However, the front is governed only by the leading dispersion in (23) and this suggest a short-cut. Since the asymptotic behavior at the front is shared by all equations (discrete and non-discrete) that are consistent with (23) we may solve the linear KdV equation

$$\frac{\partial \eta}{\partial t} + c_0 \frac{\partial \eta}{\partial x} + c_0 \beta \frac{\partial^3 \eta}{\partial x^3} = 0, \tag{72}$$

where $c_0 = \sqrt{h}$. The asymptotic solution may then be regarded as a similarity solution

$$\eta = A(t)F(\zeta), \quad \zeta = \sigma(t)^{-1}(x - c_0 t),$$

that leads to

$$\sigma^3 (c_0 \beta A)^{-1} \frac{\mathrm{d}A}{\mathrm{d}t} F - (c_0\beta)^{-1} \sigma \frac{\mathrm{d}\sigma}{\mathrm{d}t}(x - c_0 t)F' - F''' = 0.$$

An equation with only the composite quantity ζ as free variable is obtained by demanding

$$\sigma^3 (c_0 \beta A)^{-1} \frac{\mathrm{d}A}{\mathrm{d}t} = 1, \quad (c_0\beta)^{-1} \sigma \frac{\mathrm{d}\sigma}{\mathrm{d}t}(x - c_0 t) = \zeta.$$

Naturally, we could have multiplied the right hand sides by any constants, without affecting the final solution. The above relations yield $A = A_0 t^{-\frac{1}{3}}$, $\sigma = (3\beta c_0 t)^{\frac{1}{3}}$ and the differentiated Airy's equation

$$(F'' + \zeta F)' = 0.$$

In terms of the initial volume, V, the solution may then written

$$\eta \sim \frac{\frac{1}{2}V}{(\beta c_0 t)^{\frac{1}{3}}} \mathrm{Ai}\left(\frac{x - c_0 t}{(\beta c_0 t)^{\frac{1}{3}}} \right).$$

Denoting the analytical and numerical amplitudes with A_a and A_n, respectively, we then obtain the ratio

$$\frac{A_n}{A_a} = \left(\frac{\beta_a}{\beta_n}\right)^{\frac{1}{3}} \approx 1 - \frac{1}{12}\left(\frac{\hat{\Delta x}^2}{h^2}\cos^4\theta + \frac{\Delta y^2}{h^2}\sin^4\theta - \frac{\Delta t^2}{h}\right),$$

where we have introduced the angle, θ for direction of wave advance. For the example at the end of section (3.4) we now find that the computed wave front will be reduced by roughly 3%.

4.2 Eigenoscillations in basins

From the numerical dispersion relations we may find exact linear solutions for *discrete* eigenoscillations in rectangular basins. From these solutions we may extract initial conditions for simulations. The numerical model should then reproduce the eigenoscillation exactly, save for errors owing to finite precision arithmetics, round-off errors in the initial conditions and incomplete convergence of the iterative solvers involved. The latter error source is absent in 1HD cases where all equations actually are solved by direct methods. Still, effects of finite arithmetics may accumulate to yield a final error that is enlarged by a decimal power or two compared to the precision of single floating point numbers.

Two sets of test are performed. Since inclusion of the rotational effects disables simple solutions for the eigenvalue problem the Coriolis term is omitted.

- 1HD oscillations where the motion is confined to either of the grid directions. It is controlled that the results are independent of the basin width (direction transverse to the motion). In these cases the correction terms $\mathcal{A}$ and either $\mathcal{B}$ or $\mathcal{C}$ are retained.
- 2 HD oscillations where the numerical correction terms are omitted.

The simulations of eigenoscillations is a check on the computer code. On the other hand they provide no information on the performance of the numerical technique, as such, that goes beyond what is already inherent in dispersion relations and the analysis of the iteration scheme for the momentum equation.

We assume a rectangular basin of width $L = n\Delta\hat{x}$ and width $B = m\Delta y$. Modes are characterized by double indices, N and M, and expressed according to

$$\begin{aligned} \eta &= A\cos\omega_{N,M}t\cos k_N\hat{x}\cos\ell_M y, \\ u &= U\sin\omega_{N,M}t\sin k_N\hat{x}\cos\ell_M y, \\ v &= V\sin\omega_{N,M}t\cos k_N\hat{x}\sin\ell_M y, \end{aligned} \tag{73}$$

where $k_N = N\pi/L$, $\ell_M = M\pi/B$ and $\omega_{N,M}$, k_N, and ℓ_N fulfill the discrete dispersion relation. For the 1HD cases we have either $V = M = 0$ or $U = N = 0$.

For the 1HD case with numerical correction terms according to $f_m = fc = 0$ (see section 3.5.3) we have the amplitude relation

$$U = \frac{\tilde{\omega}_N A}{h\tilde{k}_N(1 - p\tilde{k}_N^2)}, \quad p = \frac{1}{24}(h\Delta t^2 - \Delta\hat{x}^2).$$

The 2HD case without numerical corrections yield the relation

$$\begin{pmatrix} U \\ V \end{pmatrix} = \begin{pmatrix} \tilde{k} \\ \tilde{\ell} \end{pmatrix} \tilde{\omega}A\left(1 - \frac{\mu^2}{3}h\tilde{\omega}^2 - \frac{\mu^4}{3}\frac{\gamma h^4(\tilde{k}^2 + \tilde{\ell}^2)^2}{1 + (\frac{1}{3} - \gamma)\mu^2 h^2(\tilde{k}^2 + \tilde{\ell}^2)}\right),$$

where the indices are omitted for brevity.

For the 1HD case and the parameters $A = 1$, $L = 8$, $h = 1$, $n = 11$, $\Delta t = 0.48727..$ we find $\omega_1 = 0.71752....$ After $t = 10.2..$, which is somewhat longer than 1 period, the errors in η are less than 10^{-13} and 10^{-6} for single and double floating point precision, respectively. This is valid for both directions and the results are independent on the transverse extension of the basin.

The 2HD case is somewhat more difficult to interpret since extra errors may arise from the iteration procedure. Initializing with the accelerations from time $(k-1)\Delta t$ the relative error before the first iteration on the accelerations at $k\Delta t$ is roughly $\omega\Delta t$. After p double sweeps we then are left with the relative error $\varepsilon = \omega\Delta t\beta^p$, where β is found from (65) inserted $f = 0$, $k = k_{N,M}$ and $\ell = \ell_{N,M}$. The number of iterations, p, is then selected as to give ε less than 10^{-8} and 10^{-16} for single and double precision, respectively. For most real problems such numbers of iterations are naturally unnecessary high. Some numerical examples are given in table 2. They are consistent with the 1HD tests above and strongly sugest that the parts of the model used in these applications are correctly coded.

L	B	n	m	β	t_m	$p(s)$	$\delta_m(s)$	$p(d)$	$\delta_m(d)$
2	2	11	8	0.238	2.6	12	$3.0 \cdot 10^{-7}$	25	$0.8 \cdot 10^{-14}$
5	4	11	8	0.025	6.4	5	$3.0 \cdot 10^{-7}$	10	$1.1 \cdot 10^{-14}$
8	6	11	8	0.005	10.2	4	$3.3 \cdot 10^{-7}$	7	$0.8 \cdot 10^{-14}$

Table 2: Maximum error in η, δ_m, for eigenoscillations during the time $0 < t < t_\mathrm{m}$. Double (64 bit) and single (32 bit) precision results are marked with (d) and (s) respectively. For all cases $M = N = 1$.

4.3 Propagation of solitary waves

An obvious test for any dispersive and nonlinear wave model is propagation and preservation (shape, height) of the solitary wave. All to often the simulation of permanent form waves, such as the solitary wave or the Stokes wave, is omitted from the test programs of wave models. This is in particular severe for models with damping, such as most Navier-Stokes solvers, since the computation of permanent waveforms may reveal the significance of artificial dissipation. The present model inherits no systematic damping and in constant depth and with no rotation, which is ignored throughout this subsection, the standard formulation ($\gamma = 0$) shares the solitary wave solution with the formulations of [27, 28]. In this subsection we employ the scaling with the depth as sole length scale. Hence, the dimensionless depth is unity and for a wave parallel to the x-axis we write

$$\epsilon\eta = Y(x - ct), \quad \epsilon u = U(x - ct),$$

to obtain

$$\begin{aligned} &Y = U(c-U)^{-1}, \\ &\tfrac{\mu^2}{6}c(U')^2 = -\tfrac{1}{6}U^3 + \tfrac{1}{2}cU^2 + U + c\log(1 - U/c), \\ &c^2 = (1+A)^2\{(1+A)\log(1+A) - A\}\{\tfrac{1}{3}A^3 + \tfrac{1}{2}A^2\}^{-1} = 1 + A + O(A^2), \end{aligned} \tag{74}$$

where A is the maximum value of Y. It is important to employ a solution that is fully consistent with the model equations and not, for instance, the solitary wave solution of the KdV equation. For plane waves the present method becomes similar to that in [28], where the concept of discrete solitary waves is investigated. In short, the discrete medium possesses solitary wave solutions, but the shape and, to a smaller extent, the speed are different from the corresponding properties of the analytical solution. Starting with (74) as initial condition we then expect the numerical solution to reshape slightly into a new permanent form.

In figure 17 the results for a series of simulations with $A = A_0 = 0.2$ and different $\Delta x = \Delta t$ is summarized. At intervals the maximum surface elevation $a(t)$ is calculated as the maximum of an interpolating cubic spline. As expected $a(t)$ approach a steady value, slightly different from A_0. The deviation from A_0 vanish with decreasing Δx. It is also observed that the modified surface profile, after $t = 200$, approximate the analytical profile, with $A = a(200)$, closely.

In figure 18 the numerical correction terms are tested for the evolution of a solitary wave with $A_0 = 0.2$ and $C = \Delta t/\Delta x = \frac{1}{2}$. The correction is moderately efficient. The limited success is due to the fact that for the shape of a solitary wave both dispersive and nonlinear effects are equally important, and the latter is still only represented with second order accuracy in the grid increments.

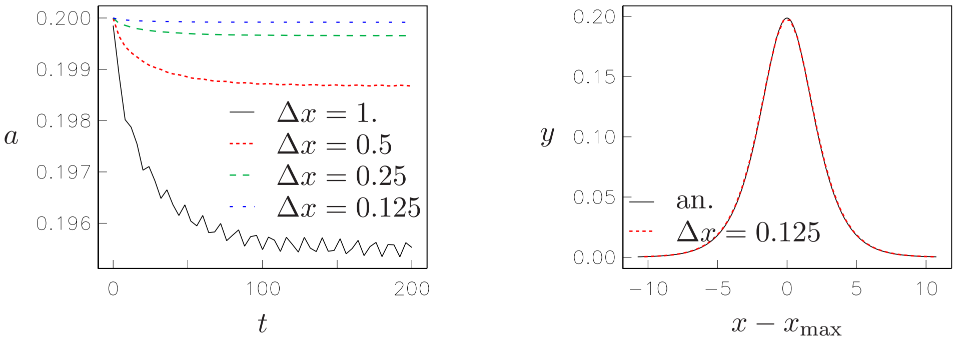

Figure 17: Left: evolution of $a(t) \equiv \eta_{\max}$. Right: comparison with analytical solitary wave shape, with amplitude $A = a(t)$, after $t = 200$ for $\Delta x = 0.125$.

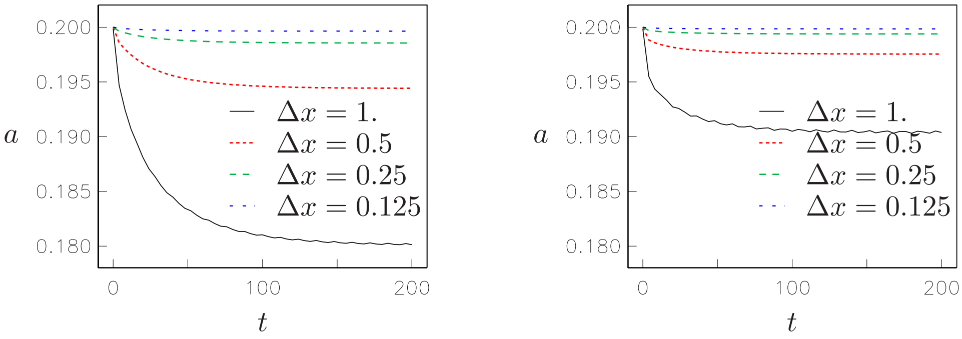

Figure 18: Evolution of $a(t) \equiv \eta_{\max}$ for Courant number $C = \frac{1}{2}$. Left: uncorrected method. Right: corrected method.

4.4 Propagation into an abyss; comparison with pre-existing models

In this section we invoke a simple test bathymetry, consisting of two uniform depth regions, with non-dimensional depths 1 and h_r, respectively, joined by a smooth slope

$$h(x) = \begin{cases} 1 & \text{if } x < x_a, \\ 1 + \frac{(h_r-1)}{2}\left(1 - \cos\left(\frac{\pi(x-x_a)}{\ell}\right)\right) & \text{if } x_a < x < x_a + \ell, \\ h_r & \text{if } x > x_a + \ell. \end{cases} \tag{75}$$

Varying the parameters h_r and ℓ we may produce cases that are more or less challenging concerning the effects of bottom gradients and wave dispersion. Generally, the length x_r should be half the wavelength, at least.

The wave propagation is started from rest with an initial elevation in the shape of half a bump adjacent to the left boundary.

$$\eta(x,0) = \begin{cases} 2A\cos^2\left(\frac{\pi x}{\lambda}\right) & \text{if } 0 < x < \frac{1}{2}\lambda, \\ 0 & \text{if } x > x_r. \end{cases} \tag{76}$$

In linear shallow water theory this will give rise to a wave of length λ and amplitude A. Naturally, the effect of dispersion will increase with decreasing λ.

For wave propagation it is not trivial to define the optimal error norm between two solutions. In a mathematical context the standard choice is some quadratic integrated norm, such as L_2. However, for long term wave propagation this may be quite inappropriate, due to accumulated errors in the phase. In fact, according to the L_2 norm two solutions of similar amplitude and shape, but large phase errors, may be more different than either of the solutions and the trivial zero field. Still, for even slightly complex wave patterns alternatives like maximum amplitude deviations are even less satisfactory. In the present investigation we study the evolution of an initial pulse over a rather short propagation distance, including a sloping region. The solution will generally consist of a leading pulse, that in constant depth would approach an asymptote given by the Airy function, and a small residual wave train that may be qualitatively different for the various models. Deviations in both should contribute to a defined error. In this case the L_2 norm is probably a sensible choice, at least in want of a better alternative.

When a discrete quantity, γ_j, is defined on a grid, x_j $(j = 1..n)$, the L_2 norm is defined as

$$\mathrm{L}_2(\gamma) = \sqrt{\sum_{j=1}^{n} \Delta x_j (\gamma_j)^2}, \tag{77}$$

where the increments, Δx_j, must be adequately defined, for instance as $\Delta x_j = \frac{1}{2}(x_{j+1} - x_{j-1})$[12]. At the boundaries special care must be exercised concerning proper calculation of the contribution to the norm. Normally, we will report normalized deviations between the different solutions with emphasis on differences in the propagation properties. In these cases the boundary contributions may as well be left out.

We need to compute the deviation between discrete quantities, γ and κ, that are defined on different grids. Interpolation is then employed to calculate values $\hat{\kappa}$, of the latter, on the

---

[12] For uniform grids we naturally employ $\Delta x_j = \Delta x$, but for methods with a variable grid, such as the boundary integral model, we need the more general expression.

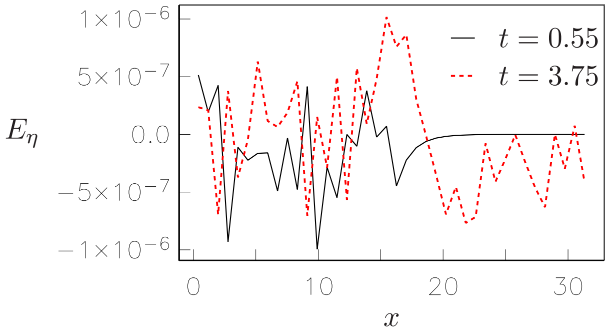

Figure 19: Difference between present and pre-existing model for the standard formulation ($\gamma = 0$). The parameters are $A = 0.2$, $\lambda = 12$, $\ell = 10$, $h_r = 2$, $\Delta x = 0.793$ and $\Delta t = 0.526$.

grid associated with γ. In case two solutions of the boundary integral method (see below) are compared we use spline interpolation that is consistent with the method itself. Otherwise, piecewise linear interpolation is invoked. The normalized deviation is then defined as

$$D(\gamma, \kappa) = \frac{\mathrm{L}_2(\gamma - \hat{\kappa})}{\mathrm{L}_2(\gamma)}. \tag{78}$$

When this procedure is employed to solutions from the same model, but with different grids, it is expressed as $D(\Delta x_1, \Delta x_2)$. It must be noted that while D is sensible as a measure of differences between converged solutions, it may become dominated by interpolation errors when applied as a measure of difference between numerical solutions obtained with different resolutions or grids. The use of $D(\Delta x_1, \Delta x_2)$ is then mainly to assure that errors of both numerics and interpolation are small enough to allow for a proper comparison of the outcome of solving different sets of *equations*.

This case is simulated by a selection of pre-existing models [33]. Among these are 1HD standard model, also used in [8], and a model for the Nwogu formulation. During the work with the present report a minor error in the Nwogu model of [33] has been discovered. Hence, all presented data are produced in new simulations using the correct models. A particular script has been devised as to “clone” old simulations of 1HD models with the model presented herein. Parameters, initial conditions and bathymetry are extracted automatically and used to set up a 2HD simulation in a basin, aligned parallel to the x-axis, with only one row of internal points. This is done to assure consistency and provide an efficient way to produce a large number of comparisons in a variety cases. However, below we will only show a few results obtained with linear simulations.

For the standard model ($\gamma = 0$) the old and new formulations are mathematically equivalent for a plane wave with direction of wave advance parallel to one of the axes. As shown in figure 19 the differences in surface elevation, E_η, are of order 10^{-6}, or smaller, which according to our experience is typical for accumulated round-off errors for this kind of models with 32-bits arithmetics.

For the optimized models, the present model with $\gamma = -0.057$ and Nwogu's with $z_\alpha = -0.531h$, exact agreement is not to be expected. Most importantly, the two models are not identical for variable depth. Besides, a small discrepancy is also introduced through the treatment of the initial conditions.

A more demanding case with a shorter initial wave elevation ($\lambda = 3$) and a steeper bottom gradient ($\ell = 2$) is depicted in figure 20. From the right panels we observe that the pre-existing and current standard formulations are virtually identical, while the performances of the current optimized model and the Nwogu model are similar. The optimized formulations are superior to the standard formulations for this case, in particular near the first trough, but they display a marked deviation from full potential theory at the front due to the large depth gradient. In the left panels the solution, at different times, and the accuracy of the potential model are shown.

4.5 Diffraction of solitary waves by a vertical cylinder

Complex geometries are represented by staircase boundaries in the present method. Such boundaries are common in ocean modeling and are known to perform fairly well for linear equations under certain conditions. However, the authors have experienced spurious effects linked to staircase boundaries even in very simple settings. A vertical impermeable wall in constant depth may act as a wave guide with non-physical trapping [25]. In shallow water combined with coarse resolution the linear solution is prone to severe noise [30, 35, 18]. When non-linearity is added in near-coast regions we may experience model breakdown. An obvious cause is the present absence of a run-up/withdrawal facility that would have removed or added grid cells and prevented inclusion of dry cells in the computational domain. However, the combination of under-resolution, non-linearity and irregular boundaries may also produce model breakdown independent of occurrence of dry cells (results not shown). A crucial question is then whether or not a staircase boundary may perform well at all for non-linear and dispersive simulations. Below, we will show that in finite depth it may.

Our test example is diffraction of waves from a circular and vertical cylinder. For periodic incident waves this is an important problem in ocean engineering. However, much of the research have been performed with cylinders of small diameter in deep or intermediate water. Moreover, the steady state solutions, that are the ones in focus, depend heavily on the use of radiation conditions. These features make diffraction of periodic waves ill suited for testing and validation of a Boussinesq solver. Hence, instead we employ large diameters and incident solitary waves.

We employ two different cylinder radii, $r = 5$ and $r = 10$, and 4 different resolutions corresponding approximately to $\Delta x = 1, \frac{1}{2}, \frac{1}{4}, \frac{1}{8}$, respectively. The cylinders are placed in the center-line of channels of width $B = 2r + 20$ with $x = x_s$ as the along-channel position. The incident solitary wave has amplitude $A = 0.15$ ($h = 1$) and the position of the initial peak is[13] $\lambda_{\frac{1}{2}} = -\ln(0.25 \cdot 10^{-3})/\sqrt{3A} = 12.4$. Accordingly the position of the center of the cylinder is $x_s = 2.1\lambda_{\frac{1}{2}} + r$. The initial setup is shown in figure 21.

Closeups for $r = 10$ are shown in figure 22, for the two coarsest and the finest resolution. We clearly see some grid dependence in the results. On the other hand, in view of the ragged appearance of the cylinder even the coarse grids produce surprisingly smooth solutions. The marks are time series locations situated at lines aligned at angles 60°, 135° and 150° relative to the positive x-direction. In addition to the angle the points are recognized by the distance, s, from the circumference of the cylinder. Time series are shown in figures 23 and 24 for $r = 10$ and $r = 5$, respectively. The results clearly point to convergence as the resolution is increased. However, for $\theta = 60°$ and $r = 5$, in particular, we observe a marked grid dependence, even in the leading wave, for the two coarsest resolutions. Still, as a whole the results are definitely

---

[13] This assures that at the distance $\lambda_{\frac{1}{2}}$ from the peak the wave height is reduced to $\approx 10^{-3}A$.

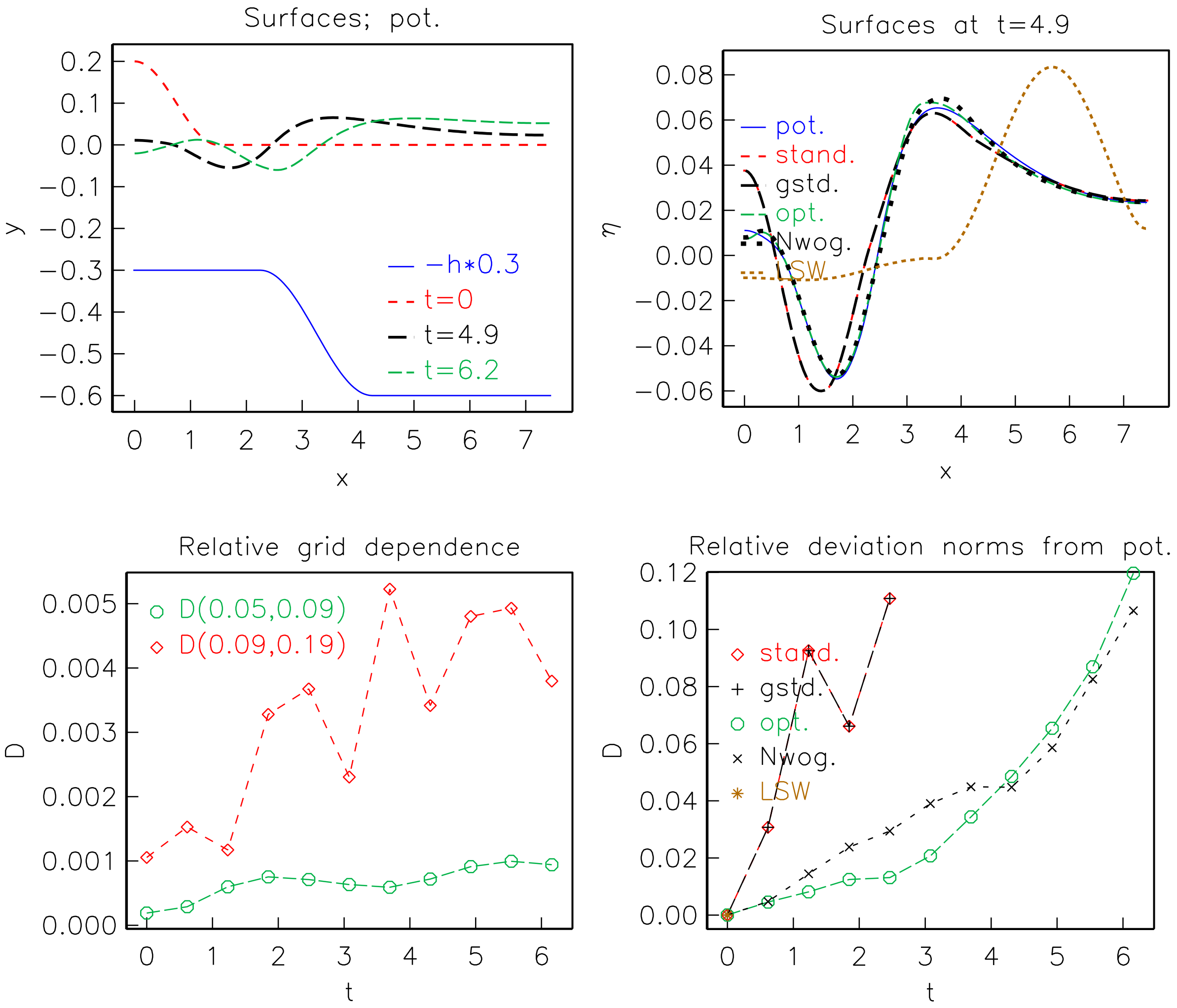

Figure 20: Comparison of linear Boussinesq and full potential models for $\boldsymbol{A = 0.2,\ \lambda = 3.0,\ \ell = 2,\ h_r = 2,\ x_r = 2.3,\ x_{\max} = 7.4,\ \Delta x = 0.05}$ (stand.). Upper left panel: surfaces at given times and the bottom. Upper right panel: comparison of different solvers at $t = 4.9$. Lower left panel: convergence of potential model; evolution of relative errors. Lower right panel: difference between other models and the potential theory. The LSW solution rapidly grows beyond the depicted window. Explanation of legends:
stand.: pre-existing standard formulation. gstd.: current standard formulation. opt.: current optimized formulation ($\gamma = -0.057$). Nwog.: Nwogus formulation. LSW: shallow water equations.

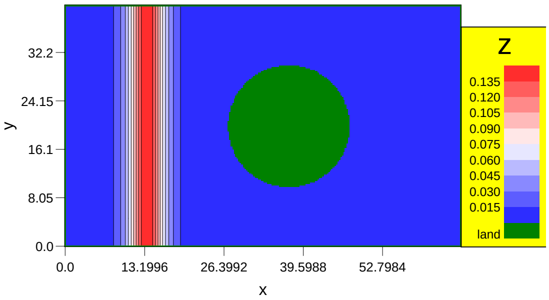

Figure 21: Initial condition for $r = 10$.

encouraging. In this test the depth is unity; a staircase boundary in shallow water, with poorly resolved incident waves, would be a different story altogether.

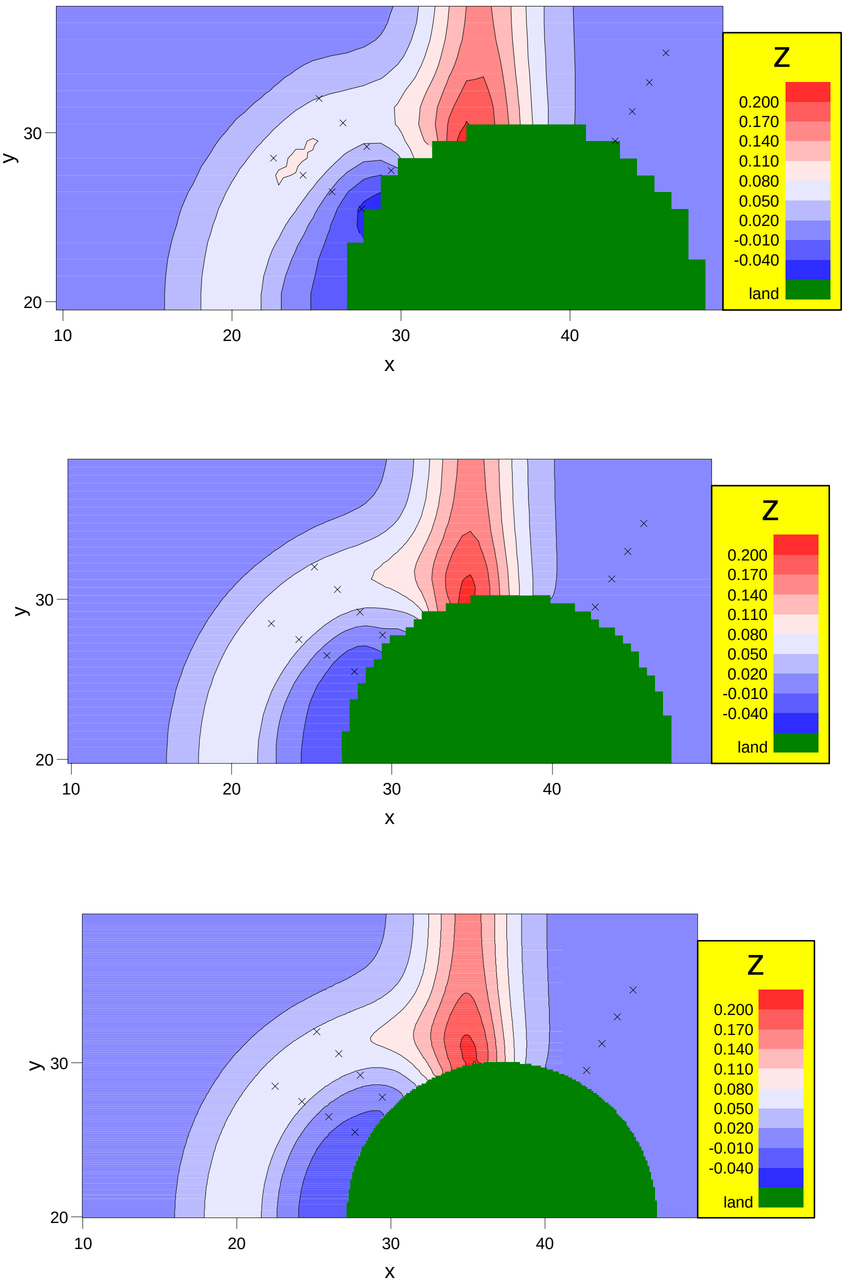

Figure 22: Contour plots of the solution after $t = 20$ for $r = 10$ and Δx equal to 1.01 , 0.50 and 0.13, respectively. Locations for time series are marked by symbols.

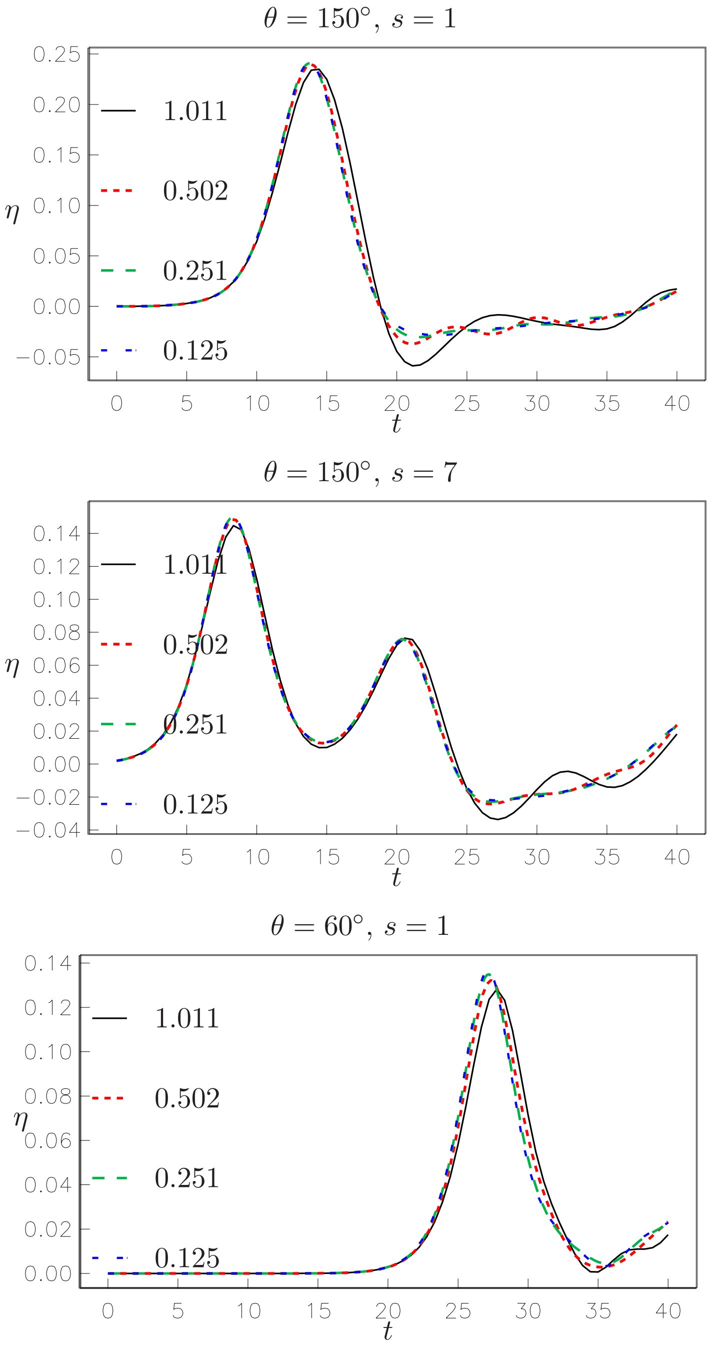

Figure 23: Time series for $a = 0.15$ and $r = 10$. The panels are marked according to the text and the curves are marked by Δx.

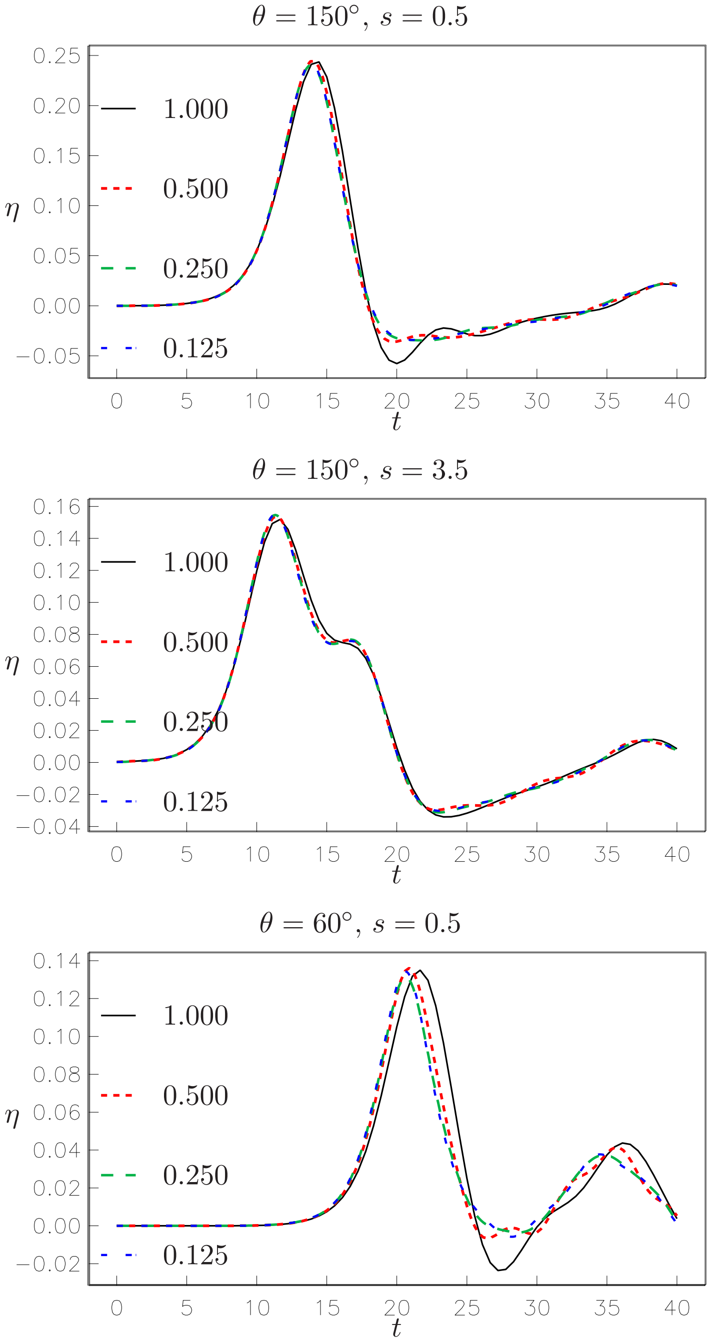

Figure 24: Time series for $a = 0.15$ and $r = 5$. The panels are marked according to the text and the curves are marked by Δx.

5 Case study example: trans-oceanic propagation

Trans-oceanic tsunamis are presumably rare in the Atlantic Ocean. The only known historical event that may be classified as such is the tsunami that followed the 1755 Lisbon earthquake. A pre-historic candidate is the Storegga tsunami. However, geological evidence of runup from this event on the coasts of America and Greenland is still not confirmed. The much debated tsunami from the Cumbre Vieja Volcano on the La Palma in the Canary Islands is clearly a potential candidate. Since the sensational claims by Ward and day (2001) [43] of a major flank collapse followed by an ocean wide tsunami disaster, other authors have questioned their results. Herein, we will not discuss neither the probability nor the consequences of a tsunami from Cumbre Vieja, but use a given, disastrous scenario for testing the present model concerning oceanic propagation of mildly dispersive tsunamis. A more complete description of the physical background and motivation for the present case study are found in [7] and [42].

The computations are carried out in four stages.

(i) First, the SAGE multi-material model for slide dynamics and wave generation is used for the first five minutes in a local bathymetry obtained by interpolation applied to ETOPO 2. Then a Boussinesq model is used for $5\,\mathrm{min} < t < 10\,\mathrm{min}$ in a particularly smooth and adapted bathymetry. All simulations for the first ten minutes are performed in a Cartesian grid and without Coriolis effects. We will not go into detail on this first phase, but focus on large scale propagation.

(ii) Surface elevation and velocities are extracted from the phase (i) and used as initial conditions at $t = 10\,\mathrm{min}$ for Boussinesq simulations, with and without nonlinearity and optimised dispersion. The computations are then continued well beyond 45 min in a regional domain which spans from 27.6°W, 21.7°N to 11.6°W, 36.0°N and includes a maximum depth of 5771 m. The depth matrix is constructed from the ETOPO 2 database, but the data are interpolated to grids with resolution $1'$ and $0.5'$. Besides, a particularly adapted threshold depth is invoked for each of the Canary Islands. For the $2'$, $1'$ and $0.5'$ grids we employ $\Delta t = 15\,\mathrm{s}$, $\Delta t = 7.7\,\mathrm{s}$, and $\Delta t = 3.9\,\mathrm{s}$, respectively. The total number of cells in the finest grid amounts to 3.3 millions.

(iii) With the surface elevation and velocities from, unless otherwise is indicated, the linear[14] regional model at $t = 45\,\mathrm{min}$ as initial conditions we employ the model with $\epsilon = 0$ (linear mode) in a large domain covering a significant part of the Atlantic Ocean (90°W, 10°S to 0°W, 60°N). Here, the ETOPO 2 grid is used without modification or we sample it to a coarser $4'$ grid. The computational domain, depicted in figure 28, includes 5.6 million cells in the $2'$ grid. From $t = 45\,\mathrm{min}$ the leading waves spend another 6 h, say, until they reach the American continent. With a time step equal to 12.7 s , relating to the maximum depth of 8637 m, this time span corresponds to 1846 time steps. For this phase we also perform plane simulations in the transects shown in figure 28, for which the $2'$ grid, as well as initial conditions, are interpolated.

(iv) The results from the trans-oceanic simulation are used for initiation of a small number of regional studies at different continents. These computations will not be addressed here, but are left for [42].

---

[14] Preferably the nonlinear results should have been used, but this is of no consequence for the assessment of the model performance for the ocean crossing.

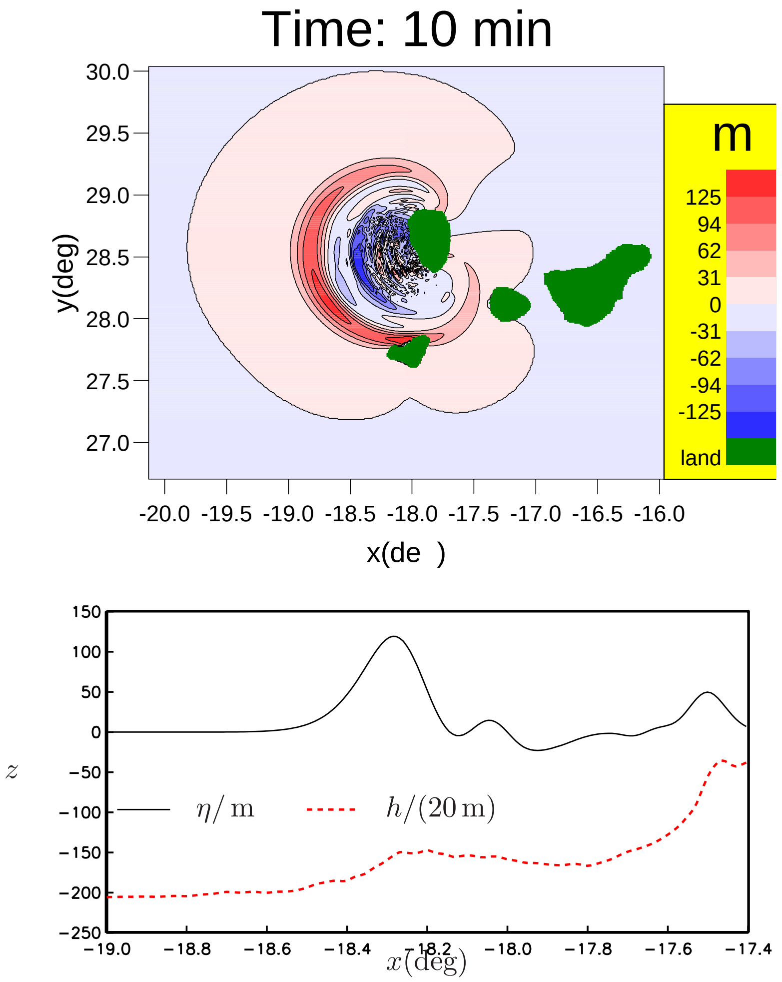

Figure 25: The La Palma tsunami after $t = 10\,\mathrm{min}$. Upper panel: contour graph of the surface elevation. Lower panel: southern transect. The surface elevation and the depth are scaled differently in the lower panel.

The transects mentioned in point (iii) are also used for comparison of 2HD results in both the regional and global simulations.

5.1 Regional simulations

The surface from the phase (i) simulation is depicted in figure 25. We observe that the waves already have entered the deep ocean, while the amplitudes are still quite impressive, well above $120\,\mathrm{m}$, and yield a wave-height to depth ratio of roughly 0.03 for the leading crest. This ratio corresponds to a weakly nonlinear wave, but the amplitude attenuates rapidly due to radial dilution of energy and frequency dispersion.

After $t = 45\,\mathrm{min}$, in phase (ii), we obtain the wave field depicted in the figures 27. In the figure we observe a series of waves spreading outward from the source region with a preferred directionality to the West. From the figure 26 we infer that the accumulated nonlinear effects for $10\,\mathrm{min} < t < 45\,\mathrm{min}$ are weak and that there are only small differences between the results for[15] $\Delta\psi = \Delta\phi = 2'$ and $\Delta\psi = \Delta\phi = 0.5'$ (0.4 m for southern transect, 0.1 m for the two others). The number of iterations is varied between 1 and 4. For the East-West transect there is very little difference, as the wave advance is nearly parallel to the x axis, but for the southern transect (figure 26, lower panel) we observe errors when only one iteration is used. However, the difference between 2 and 4 iterations is small (0.4 cm for height of leading crest) and 2 iterations are hence employed for the global simulation (phase iii).

The numerical correction terms does not improve the regional simulations significantly. As observed below, this is quite different for the global propagation phase.

5.2 Trans-Atlantic wave propagation

In the trans-ocean propagation (phase iii) we focus on long term dispersion effects. Without the correction terms, but with the remaining terms kept in the computations[16] the CPU time is close to 5 h in serial run on a two years old AMD desktop. The dispersion optimisation term add another 10 min, while the numerical correction terms are included at an extra expense of 50 min. Certainly there is room for much larger computations, in particular if parallel computing is employed. However, to assess the performance of the model relative to sensitivity regarding resolution it will suffice to include 2HD simulations with a $4'$ resolution combined with a more complete transect (1HD) grid refinement study in a transect. This transect, at 28° N, is the middle one in figure 28. The northern and southern transects displayed in the figure are used for error analysis in the 2HD simulations only.

To give an idea of the evolution of the wave system a few surface profiles, at 28° N, from the 2HD simulation, with $\gamma = 0$, are shown in figure 29. As time increases we observe a reduction of wave heights, partly due to radial spreading and partly to frequency dispersion, stretching of the leading crest and that the trailing waves eventually become higher than the leading one. For more details and explanation we refer to [42]. From the figure we also observe that there are marked deviations between the $2'$ grid (with correction), and the $4'$ grid without correction. These differences increase with the distance from the start of the wave train and become particularly evident when interference is important. With correction the $4'$ grid yields very good agreement with the $2'$ grid nearly throughout the part of the wave train that is displayed. Even further back the deviations will be larger and also more influenced by diffraction effects from islands and continents that presumably are strongly grid dependent. The difference between the corrected $2'$ and $4'$ grids also appears to be larger at some of the peaks. To investigate this further we compute the maxima by spline interpolation. Local maxima below 0.5 m and maxima closer than 0.5° to other maxima are ignored. In the latter case, if several maxima are clustered, which may happen for fine grids, the highest one is selected. Figure 30, and table 3 confirm that there are noticeable differences in the maxima also for the corrected simulations. Wave peaks at the other transects are shown in figure 31. For the northern transect the waves reach the American continental shelf already at roughly 57.2° W. Hence, an earlier time is selected for this transect; when the waves enter the shelf a $4'$ grid, in particular, becomes too coarse to give any meaningful results. Again the positive effect of the correction terms is apparent for the southern transect, while both $4'$ grids are good for the first few peaks in the northern transect. The evolution of the leading crest is very regular, while there are fluctuations in the

---

[15] $\Delta\psi$ and $\Delta\phi$ are the non-scaled counterparts to Δx and Δy, respectively, according to (7).

[16] The discrete nonlinear terms are computed, but the contributions are multiplied with zero. This is done to avoid dry cells at the shore and to avoid problems with heavily under-resolved waves in shallow regions.

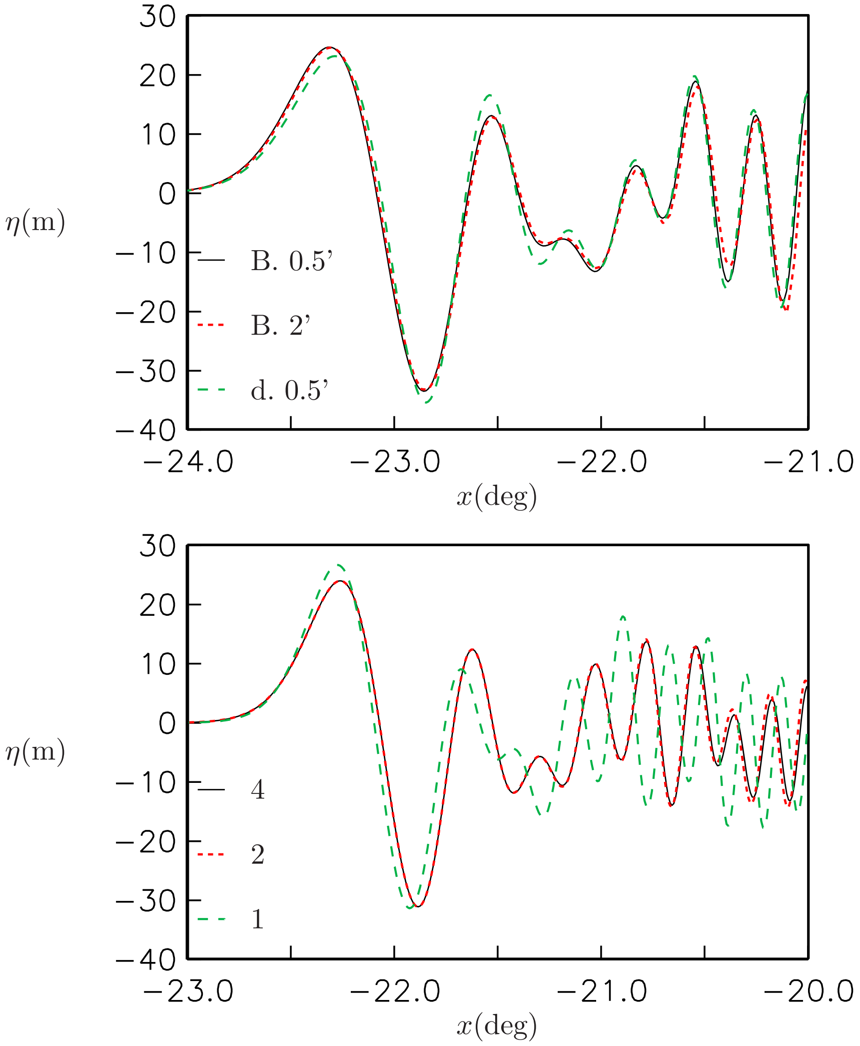

Figure 26: Upper panel: east-west transect after $t = 45$ min; Boussinesq results (B.), for $2'$ and $0.5'$ grid and linear dispersive results (d.).
Lower panel: southern transect after $t = 45$ min; Boussinesq results marked by the number of iterations.
All results inthis figure are obtained with optimized dispersion, in the lowe panel also numerical corrections are used.

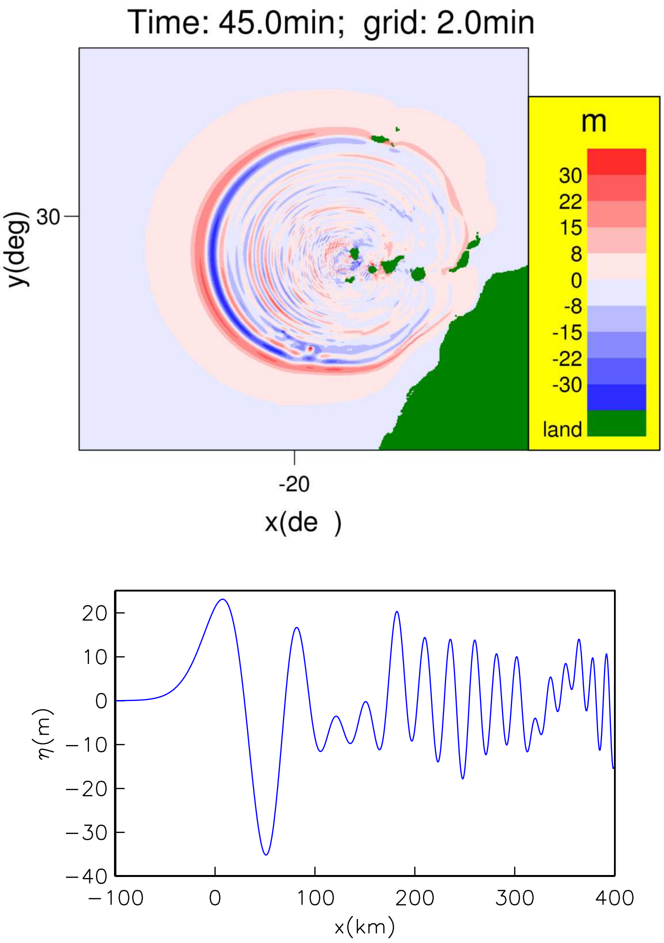

Figure 27: The La Palma tsunami after 45 min. Upper panel: contour graph of the surface elevation. Lower panel: transect at 28° latitude, with a redefined origin close to the leading crest.

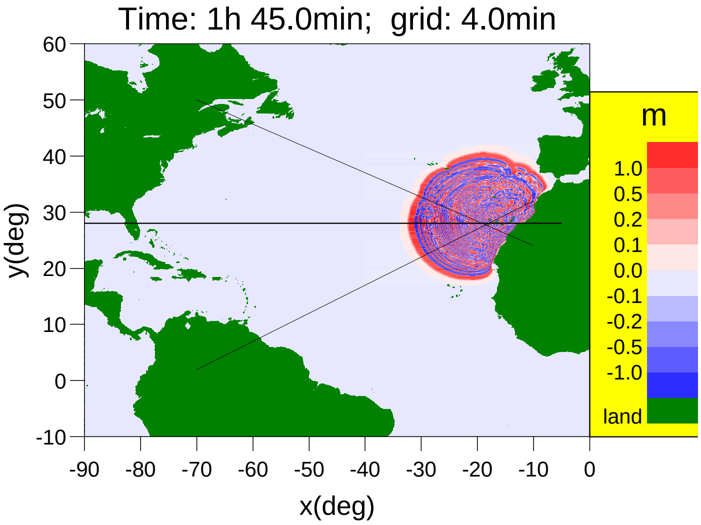

Figure 28: The three transects used for sensitivity studies.

grid	1	2	3	4	5	6	7
$2'$(c)	1.79	0.66	1.57	3.30	5.53	3.58	1.94
$4'$(c)	1.80	0.65	1.56	3.00	5.27	3.76	1.91
$2'$	1.77	0.70	1.46	3.14	5.36	3.61	1.91
$4'$	1.71	0.81	1.17	2.43	4.55	3.78	0.99

Table 3: Surface maxima, in sequence from the front of the wave train, in 28°N transect after 6h 15.0min. The rows are marked by grid increments and an additional (c) if they correspond to a simulation with correction terms.

deviations between the different solutions for the subsequent crests. Using the corrected $2'$ simulation as reference we obtain the differences in figure 32. We observe that the $4'$ results start out with a common error due to interpolation errors in the initial condition. Then the deviation from the reference solution diminishes, presumably due to increasing length of the leading crest. The corrected $4'$ solution rapidly becomes more accurate than the uncorrected $2'$ solution. The final heights ($t = 6\,\text{h}\ 45\,\text{min}$) of the corrected and uncorrected $2'$ simulations are 1.586 m and 1.564 m, respectively. Since the corrected $2'$ and $4'$ solutions agree very closely for the first two crests (figure 29 and table 3), we may assume that they describe the front of the wave system accurately. This points to an error less than 1.5% for the leading crest of the uncorrected solution with $2'$ resolution. We may also estimate this error through the assumption that the wave height for the uncorrected solution is approximately $H_{\Delta\psi} = H_0 + b\Delta\psi^2$, where H_0 corresponds to the analytical value. The $4'$ grid with $I_k = 0$ yields a leading peak height equal to 1.509 m. From $H_{2'}$ and $H_{4'}$ we then find $H_0 = 1.582\,\text{m}$ which is fairly consistent with the previous error estimate of 1.5%.

An illustration of the overall importance of nonlinearity and optimised dispersion is given

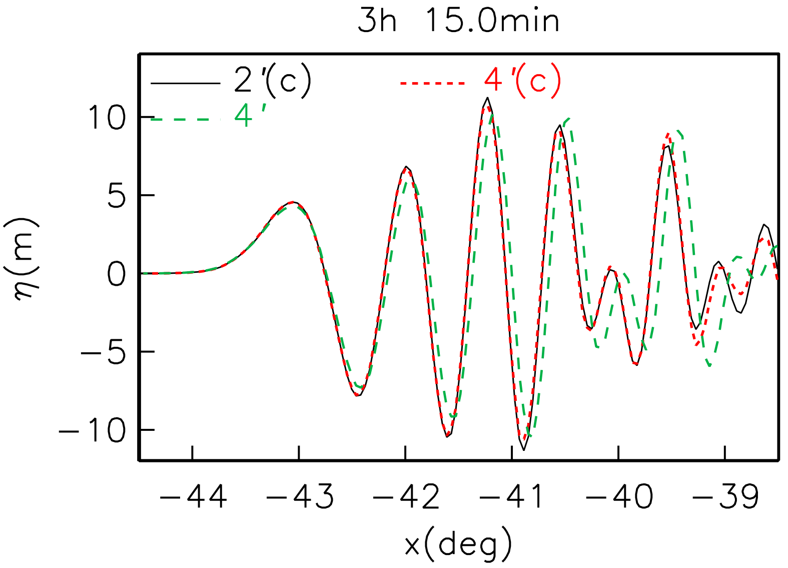

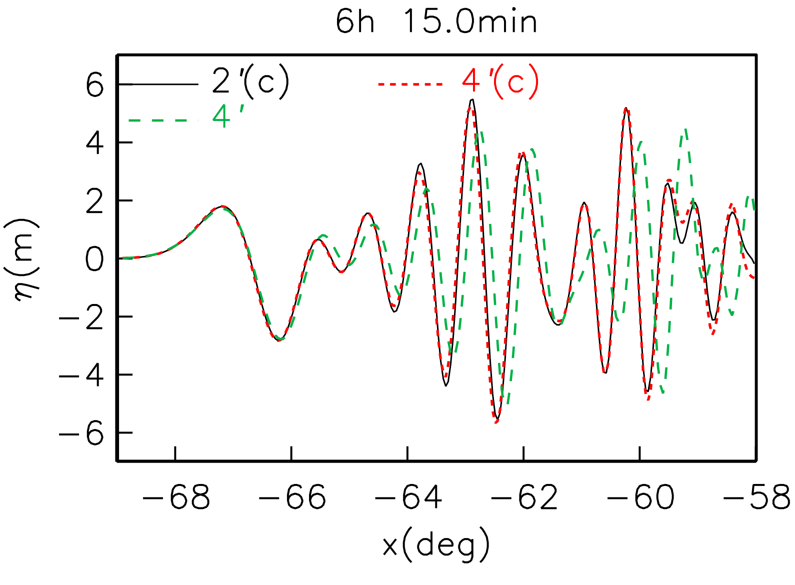

Figure 29: Surface profiles at 28° N. The curves are marked by grid increments and an additional (c) if they correspond to a simulation with numerical correction terms. At this latidue one longitudinal degree corresponds to 98.3 km.

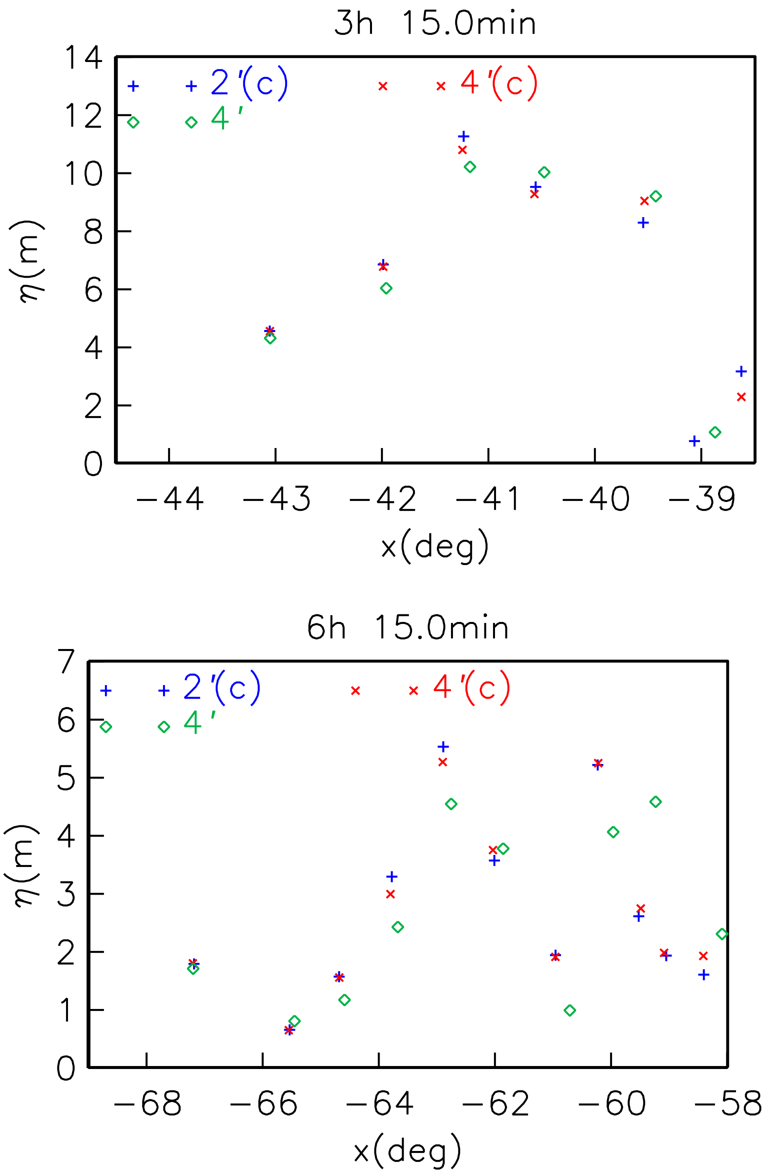

Figure 30: Surface maxima at 28° N. The curves are marked by grid increments and an additional (c) if they correspond to a simulation with correction terms.

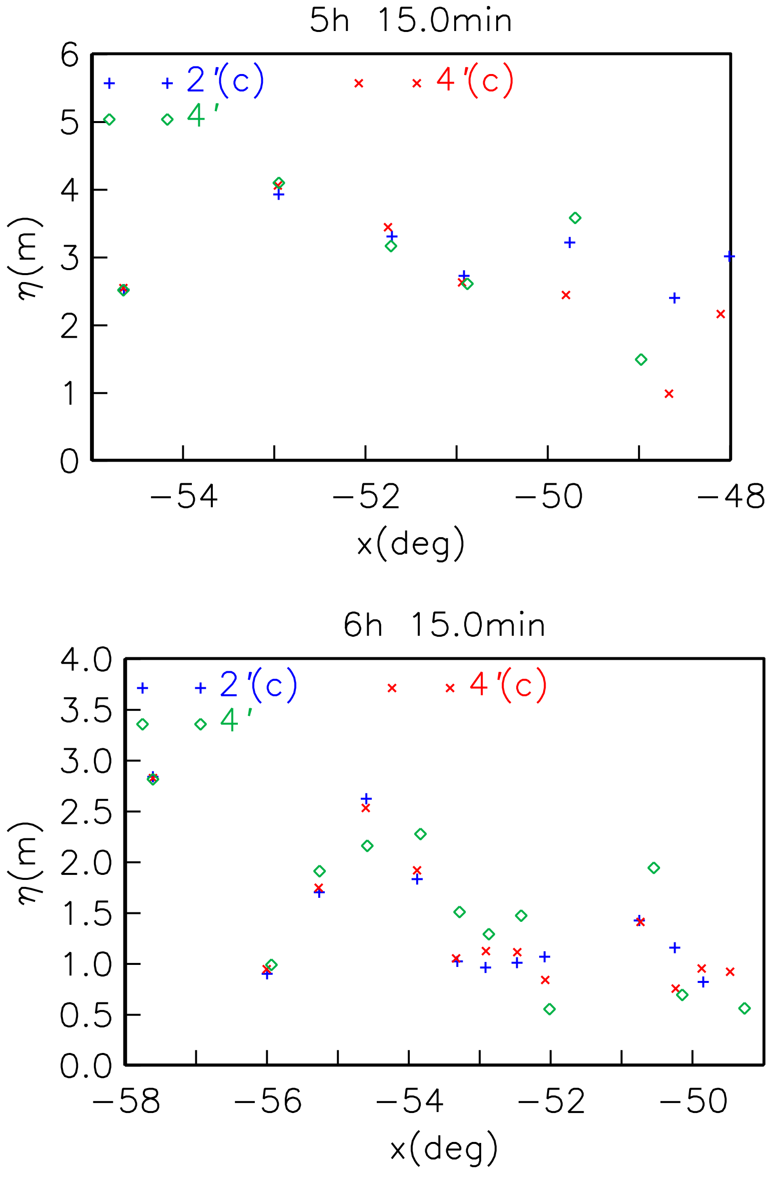

Figure 31: Surface maxima at northern (upper panel) and southern (lower panel) transects. The curves are marked by grid increments and an additional (c) if they correspond to a simulation with correction terms.

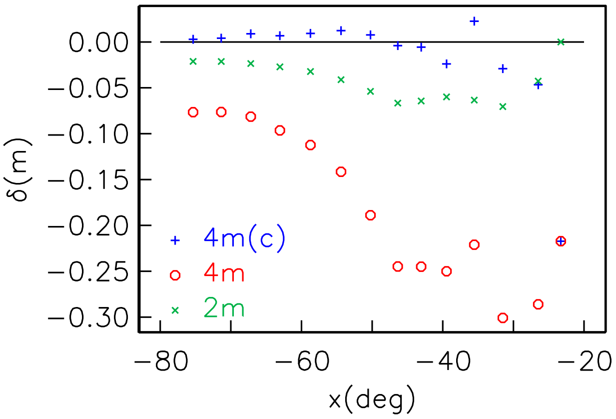

Figure 32: Convergence of 2HD model; deviations from the simulation with a $2'$ grid and numerical correction terms. The quantity δ is the difference in the height of the leading crest and the numbers in the legend are grid increments in minutes.

Models	1	2	3	4	5	6	7
Bouss(o)+disp(o)	1.88	0.83	1.35	3.55	5.52	3.75	1.59
Bouss+disp	1.88	0.83	1.31	3.44	5.47	3.94	1.37
disp+disp	1.77	0.78	1.24	3.35	5.50	4.06	1.57

Table 4: Surface maxima, in sequence from the front of the wave train, in transect after 6h 15.0min. The rows are marked by combination of models used in regional and global simulations. The (o) indicates that the optimal value of γ is used, otherwise $\gamma = 0$.

in figure 33 and table 4. Omission of nonlinearity in the regional simulation will alter the wave height by typically $5 - 8\%$ when the waves have nearly crosed the Atlantic ocean. The effect of dispersion optimisation is much smaller, but increases toward the rear of the wave train.

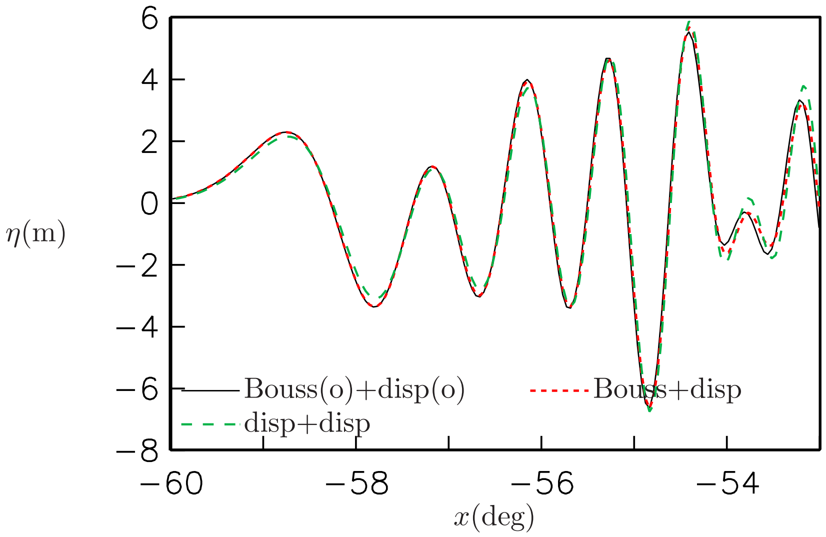

Figure 33: Results for various model combinations at 28°N transect at $t = 6\,\mathrm{h}\ 15\,\mathrm{min}$. The two parts of the curve legend correspond to phase (ii) and (iii), respectively. "Bouss" and "disp" denotes Boussinesq and linear dispersive equations, respectively, while the "(o)" indicates optimized dispersion. All simulations are performed on a $2'$ grid without numerical corrections.

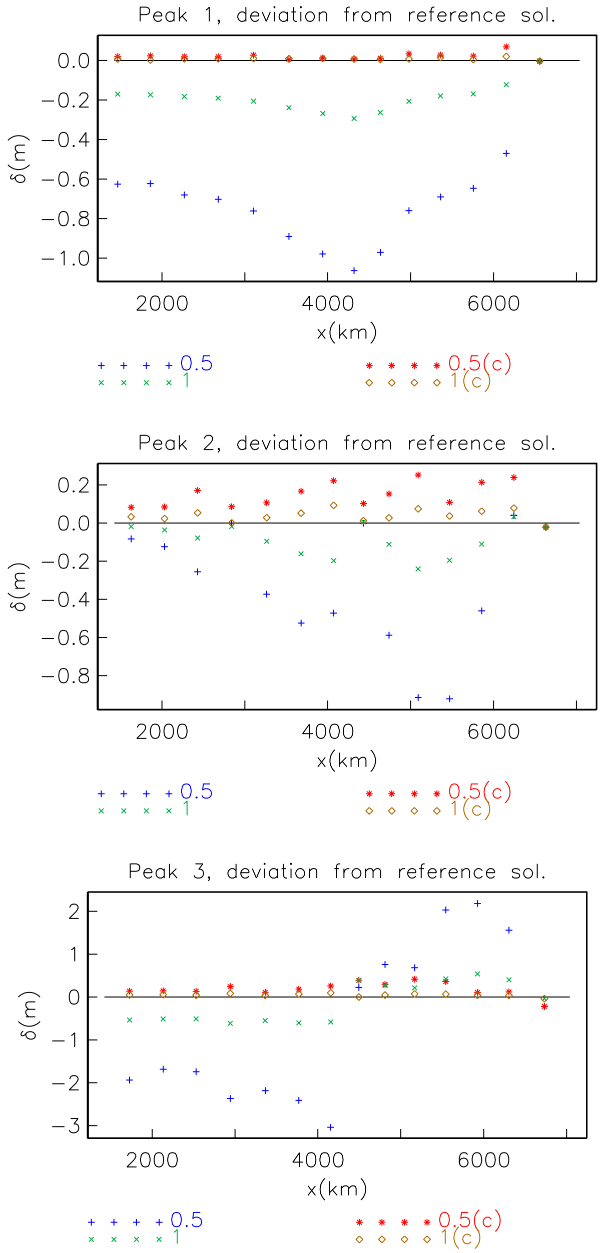

Figure 34: Differences in peak height in plane simulations. The curves are identified by the grid factor F_g and an 'c' when correction terms are used.

5.3 Transect simulations in 1HD

Even though the 2HD simulations provide a reasonably good basis for estimation of accuracy it is useful to pursue the grid refinement further in 1HD transect simulations which allow a wider span in grid resolution. Then the transect at 28° N is used. Plane simulations, such as these, are most conveniently performed with Cartesian coordinates. The origin is selected at 90° W and we define a reference grid corresponding to $2'$, which yields $\Delta x_r^* = 3.3\,\text{km}$, and a refinement factor $F_g = \Delta x^*/\Delta x_r^*$. This factor ranges from 8 (finest grids) to 0.5 (corresponding to $4'$). The corrected simulation with $F_g = 8$ is chosen as reference and deviations in peak heights are displayed in figure 34. The minimum separation distance is now set to 1 km. The first peak is very well reproduced by $F_g = 1$ when the correction terms are retained, while also the corrected method with $F_g = 0.5$ yields good agreements with the reference solution. The uncorrected simulations yield larger errors. Clearly, the deviations are larger for the second and third peak, but the corrected method still performs well with $F_g = 1$ and $F_g = 0.5$. In relative terms $F_g = 1$, without corrections, and $F_g = 0.5$, with corrections, yield more comparable errors for the following crests than the first one. We note that in 1HD simulations we have no radial spreading and the leading crests become much higher (finally around 8 m, 10 m and 11 m, respectively). This must be kept in mind with relation to interpretation of the errors.

The depth related corrections have been left out in all simulations. Still, we obtain a good effect of the numerical correction terms even for grids with $4'$ spatial increments. This suggest that the correction terms are useful also in realistic simulations with digitised bathymetries.

6 Remarks

The analysis, tests and applications in this report demonstrate that the proposed model, including mathematical formulation, numerical algorithm and implementation in computer code, works correctly and efficiently, within its limitations. In its present form it is an adaptation and extension of an preceding numerical technique. The motivation is long distance propagation of weakly dispersive tsunamis. For this purpose the model is very well suited. It is also very useful for weakly nonlinear and dispersive propagation of waves in other contexts where a neutrally stable method, also in relation to nonlinearity, is required. However, while we believe that concerning the documentation and validation this report is comparable, at least, to most other treatises of its kind, our model still lacks a number of the features found in, for instance, the FUNWAVE/COULWAVE models. Some of the features in question may be included later, while others may never be included. It is anyhow important that the model stays comparatively simple and efficient. Some lacking features, that *may* be included in the future, can be identifies as

- A runup model.
- Inclusion of breaking waves.
- Put the model in a framework for large scale parallel computing and combination with other types of tsunami models.
- More general and flexible inclusion of tsunami sources.

- Full nonlinearity, such as in FUNWAVE/COULWAVE. This feature may enhance the performance of the method in some coastal engineering applications. On the other hand, the gain is small in other applications [13, 34, 24].

A Long wave equations

We employ a typical depth d and a wavelength L as vertical and horizontal length scales, respectively. The choice of L, in particular, is ambiguous and it may also correspond to other lengths than that of a wave. Identifying the time scale $t_c = L/\sqrt{gd}$, where g is the acceleration of gravity, and the dimensionless amplitude, ϵ, we define $\epsilon L/t_c$, $\epsilon d/t_c$ and ϵd, respectively, as scales for horizontal velocity, vertical velocity and surface elevation. Whereas the extraction of the amplitude factor, ϵ, is convenient for classification and description of long wave models, it will generally make results from computations less transparent. Hence, we will in graphs modify the scaling in a way that corresponds to putting $\epsilon = 1$ instead of invoking some amplitude measure.

Different long wave equations can be obtained through perturbation expansions in $\mu \equiv d/L$ and ϵ and may then be classified according to which orders of these parameters that are retained in the equations. Omission of all μ terms yields the nonlinear shallow water (NLSW) equations, while retaining second order in μ yields Boussinesq type equations that are available in a series of varieties [38, 44, 22]. Long wave theory prescribes a simple vertical structure of the field variables. In NLSW theory the horizontal velocity is vertically uniform and the pressure hydrostatic. Therefore, the vertical coordinate, z, vanishes from the equations. When $O(\mu^2)$ terms are retained there are vertical variations in the horizontal velocity. Still, the explicit appearance of z is removed from the continuity and momentum equations by integration. Hence, in this form they are often referred to as "depth integrated equations". The spatial dimension of the partial differential equations is then reduced by one. Furthermore, the nonlinear free surface appear only through nonlinear coefficients. These features make long wave formulations well suited for numerical solution. Regardless of the mathematical reduction of dimension, we will still refer to problems as two- or three dimensional according to the physical configuration.

The order of a long wave equation is reflected in the dispersion characteristics. According to full potential theory the dispersion relation of a linear, sinusoidal wave reads (depth: $h = 1$)

$$c^2 = \frac{1}{k\mu}\tanh(\mu k) = 1 - \frac{1}{3}(\mu k)^2 + \frac{2}{15}(\mu k)^4 + ..., \qquad (79)$$

where c is the phase speed and k is the wave number. Shallow water theory only reproduces the first term on the right hand, while traditional Boussinesq equations yield the first two. However, as we will see below, different formulations valid to $O(\mu^2)$ give different dispersion properties. They may even reproduce the $O(\mu^4)$ term in (79) correctly or display an extended validity range.

A.1 Boussinesq theory

During the last fifteen years fully nonlinear Boussinesq type equations with improved dispersion properties have been put to work in computer models. Following [10] we write a set of fully nonlinear Boussinesq equations on the form

$$\eta_t = -\nabla \cdot \left[(h+\epsilon\eta)(\mathbf{v}+\mu^2\mathbf{M})\right] + O(\mu^4), \tag{80}$$

$$\mathbf{v}_t + \frac{\epsilon}{2}\nabla(\mathbf{v}^2) = -\nabla\eta - \mu^2\left[\frac{1}{2}z_\alpha^2\nabla\nabla\cdot\mathbf{v}_t + z_\alpha\nabla\nabla\cdot(h\mathbf{v}_t)\right] \tag{81}$$
$$+\epsilon\mu^2\nabla(D_1+\epsilon D_2+\epsilon^2 D_3) + O(\mu^4) + \mathbf{N} + \mathbf{E},$$

with

$$\begin{aligned}
\mathbf{M} &= \left[\frac{1}{2}z_\alpha^2 - \frac{1}{6}(h^2-\epsilon h\eta+\epsilon^2\eta^2)\right]\nabla\nabla\cdot\mathbf{v} + \left[z_\alpha + \frac{1}{2}(h-\epsilon\eta)\right]\nabla\nabla\cdot(h\mathbf{v}),\\
D_1 &= \eta\nabla\cdot(h\mathbf{v}_t) - \frac{1}{2}z_\alpha^2\mathbf{v}\cdot\nabla\nabla\mathbf{v} - z_\alpha\mathbf{v}\cdot\nabla\nabla\cdot(h\mathbf{v}) - \frac{1}{2}(\nabla\cdot(h\mathbf{v}))^2,\\
D_2 &= \frac{1}{2}\eta^2\nabla\cdot\mathbf{v}_t + \eta\mathbf{v}\nabla\nabla\cdot(h\mathbf{v}) - \eta\nabla\cdot(h\mathbf{v})\nabla\cdot\mathbf{v},\\
D_3 &= \frac{1}{2}\eta^2\left[\mathbf{v}\cdot\nabla\nabla\cdot\mathbf{v} - (\nabla\cdot\mathbf{v})^2\right],
\end{aligned}$$

and where the index t denotes temporal differentiation, h is the equilibrium depth, η is the surface elevation, $\mathbf{v}$ is the horizontal velocity evaluated at $z = z_\alpha$ and ∇ is the horizontal component of the gradient operator. The heuristic terms $\mathbf{N}$ and $\mathbf{E}$ in the momentum equation (81) represent bottom drag and artificial diffusion, respectively. This particular form of the leading dispersion ($\epsilon^0\mu^2$) term was discussed and tested by [23], while additional nonlinearity was added by [6].

A similar formulation, with the velocity potential as primary unknown instead of the velocity, is found in [4]. Applying transformations and deletion of various higher order terms to the set (80) and (81) we may reproduce a number of other Boussinesq type equations from the literature [23, 6, 14]. As pointed out in the reference [6] weakly nonlinear versions, in the sense that some or all $O(\epsilon\mu^2)$ terms are omitted, may sometimes yield nonzero volume flux at the shoreline of a sloping beach. This should in particular be avoided for runup simulations.

When h is constant and $\epsilon \to 0$ Boussinesq equations on the form (80,81) yield c^2 as a rational function of $\mu^2 k^2$

$$c^2 = h\frac{1-\alpha\mu^2h^2k^2}{1+\beta\mu^2h^2k^2}, \tag{82}$$

where $\beta = -\frac{z_\alpha}{h} - \frac{z_\alpha^2}{2h^2}$ and $\alpha = \frac{1}{3} - \beta$. The latter identity assures that we always reproduce the $O((kh)^2)$ term in (79), regardless of the value of z_α. For $z_\alpha = (\sqrt{1/5}-1)h$ the expression (82) reproduces the first three terms in the expansion (79), while $z_\alpha = -0.531h$ yields a particularly favourable dispersion relation over an extended range of wave numbers. (see figures 35 and 36). With $z_\alpha = (\sqrt{1/3}-1)h$ the velocity $\mathbf{v}$ differs from the depth depth averaged velocity ($\overline{\mathbf{v}}$) by $O(\epsilon\mu^2)$, only. If we then delete all $O(\epsilon\mu^2)$ terms in (80) and (81) we retrieve the traditional Boussinesq equations for constant depth. These possess a dispersion relation that is clearly inferior to the optimal version of (80,81) (figure 35).

A.2 Standard and “mild-slope” Boussinesq equations

In general, the form of the volume flux in (80) implies[17] $\overline{\mathbf{v}} = \mathbf{v} + \mu^2\mathbf{M}$. Differentiating this relation with respect to time, inserting the resulting expression for $\mathbf{v}_t$ in (81), and invoking

---

[17] To reproduce $\overline{\mathbf{v}}$ from $\mathbf{v}$ in non-constant depth we would have to employ a time dependent z_α.

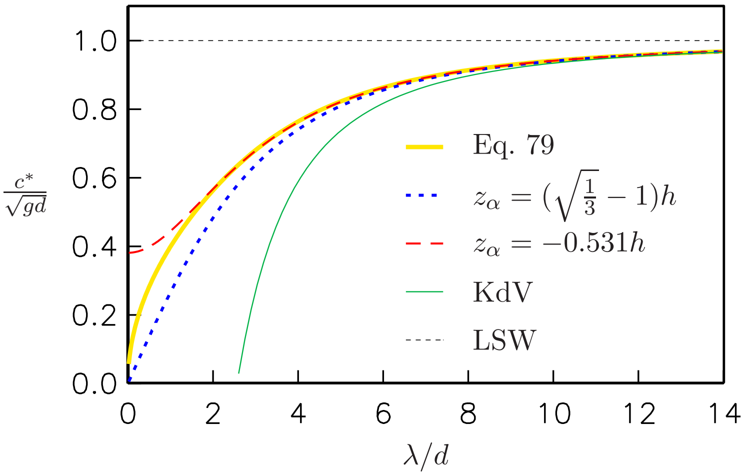

Figure 35: The phase speed as function of wavelength for long wave equations compared to that of the fully inviscid set. The curve for the Korteweg-deVries (KdV) equation is included for comparison.

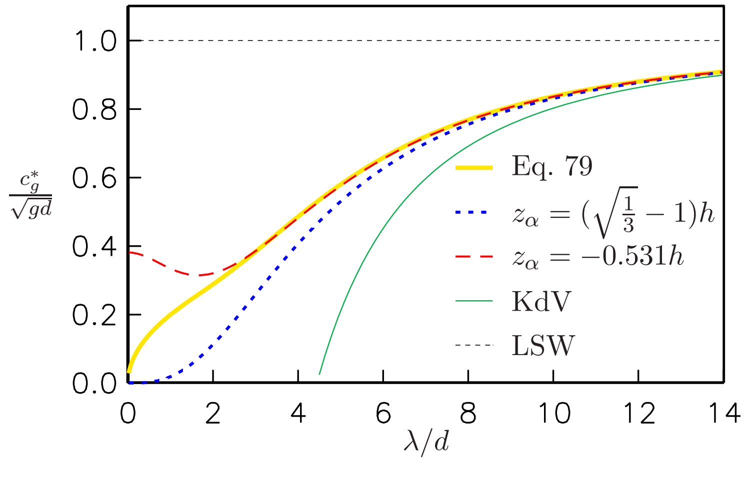

Figure 36: The group velocity as function of wavelength for long wave equations compared to that of the fully inviscid set. The curve for the Korteweg-deVries (KdV) equation is included for comparison.

$\mathbf{v} = \overline{\mathbf{v}} + O(\mu^2)$ in nonlinear and dispersive terms we obtain the standard Boussinesq equations that inherit errors of order $\epsilon\mu^2, \mu^4$

$$\frac{\partial \eta}{\partial t} = -\nabla \cdot ((h + \epsilon\eta)\overline{\mathbf{v}}), \tag{83}$$

$$\frac{\partial \overline{\mathbf{v}}}{\partial t} + \epsilon \overline{\mathbf{v}} \cdot \nabla \overline{\mathbf{v}} = -\nabla \eta + \frac{\mu^2}{2} h \nabla\nabla \cdot (h \frac{\partial \overline{\mathbf{v}}}{\partial t}) - \frac{\mu^2}{6} h^2 \nabla^2 \frac{\partial \overline{\mathbf{v}}}{\partial t} + O(\mu^4, \mu^2\epsilon) + \mathbf{N} + \mathbf{E}. \tag{84}$$

If we delete **N** and **E** we may invoke the depth averaged velocity potential and the standard Boussinesq equations take on the form [26, 17]

$$\frac{\partial \eta}{\partial t} = -\nabla \cdot \left[(h + \epsilon\eta)\nabla\phi + \mu^2 G_2\right] + O(\mu^4, \mu^2\epsilon), \tag{85}$$

$$\frac{\partial \phi}{\partial t} + \frac{1}{2}\epsilon(\nabla\phi)^2 + \eta + \mu^2 G_1 = O(\mu^4, \mu^2\epsilon). \tag{86}$$

The terms G_1 and G_2 are dispersion terms that may be written according to

$$G_1 = -\frac{1}{2} h \nabla \cdot \nabla (h \frac{\partial \phi}{\partial t}) + \frac{1}{6} h^2 \nabla^2 \frac{\partial \phi}{\partial t}, \tag{87}$$

$$G_2 = h \left(\frac{1}{6} \frac{\partial \eta}{\partial t} - \frac{1}{3} \nabla h \cdot \nabla \phi \right) \nabla h. \tag{88}$$

It must be emphasized that the sets (83,84) and (85,86) are far from equivalent, unless the depth is constant. The relation between the velocity and potential then reads

$$\overline{\mathbf{v}} = \nabla \phi, \tag{89}$$

and the formulations share the same curve in figure 35. However, in case of variable depth the relation between $\overline{\mathbf{v}}$ and ϕ is much more complex and the appearance of depth gradients in (85) and (86) is both inconvenient and prone to instabilities that are pursued in an ongoing parallel investigation. Assuming a mild bottom variation we may delete depth gradients in the dispersion terms and employ the simpler relations

$$G_1 = -\frac{1}{3} h^2 \nabla^2 \frac{\partial \phi}{\partial t}, \quad G_2 = 0. \tag{90}$$

In view of the approximations implicit in (90) it is now consistent to employ the relation (89) also for non-constant depth.

Subsequently we will refer to the set (83) and (84) as the standard Boussinesq equations, while (85) and (86) with (90) will be denoted as “mild” or “mild-slope” Boussinesq equations. The latter formulation is, maybe, the simplest Boussinesq equation that can be employed for propagation of nonlinear and weakly dispersive waves.

A.3 The standard formulation with improved dispersion properties

As an alternative to procedure in section A.1 we may employ a simple idea proposed by Madsen and co-workers in a series of papers [22] to obtain improved dispersion properties. Starting with the standard formulation, (83) and (84), we simply add an extra term of order $\mu^4, \epsilon\mu^2$ to the latter equation. This term is of the form $\mu^2 G$, where

$$G = -h^2\gamma\nabla^2(\frac{\partial\overline{\mathbf{v}}}{\partial t} + \nabla\eta) = O(\mu^4, \epsilon\mu^2)$$

where the last identity follows from the leading order balance of the momentum equation. The modified momentum equation then becomes

$$\begin{array}{rcl} \frac{\partial\overline{\mathbf{v}}}{\partial t} + \epsilon\overline{\mathbf{v}}\cdot\nabla\overline{\mathbf{v}} & = & -\nabla\eta - \gamma\mu^2h^2\nabla^2\nabla\eta + \frac{\mu^2}{2}h\nabla\nabla\cdot(h\frac{\partial\overline{\mathbf{v}}}{\partial t}) \\ & & -\mu^2(\frac{1}{6}+\gamma)h^2\nabla^2\frac{\partial\overline{\mathbf{v}}}{\partial t} + O(\mu^4,\mu^2\epsilon) + \mathbf{N} + \mathbf{E}. \end{array} \tag{91}$$

The factor γ may be used to optimize the dispersion properties, in analogy to z_α. We again obtain a dispersion relation of the form (82) with $\alpha = \gamma$. Hence, we have dispersion properties identical to those of (80,81) when

$$\gamma = \frac{1}{3} + \frac{z_\alpha}{h} + \frac{1}{2}\frac{z_\alpha^2}{h^2} \tag{92}$$

The optimal value $z_\alpha = -0.531h$ then corresponds to $\gamma = -0.057$. Naturally, the common dispersion relation must imply that also the differential equations are equivalent. This is demonstrated most simply by starting with (80). We insert constant depth, omit nonlinearities, employ (92) and make the identification

$$\overline{\mathbf{v}} = \mathbf{v} + \mu^2h^2\gamma\nabla\nabla\cdot\mathbf{v}. \tag{93}$$

This immediately reproduces the continuity equation for the depth averaged velocity. We make the same assumptions in (81), delete the ad-hoc terms, invokes the above relation, and arrive at

$$\frac{\partial\overline{\mathbf{v}}}{\partial t} = -\nabla\eta + \mu^2h^2(\frac{1}{3}-\gamma)\nabla\nabla\cdot\frac{\partial\mathbf{v}}{\partial t}.$$

From this momentum equation we readily obtain an expression for $\gamma\mu^2h^2\nabla\nabla^2\eta$ in terms of $\overline{\mathbf{v}}$ and $\mathbf{v}$. When this expression is subtracted from the right hand side of the above momentum equation we may use (93) once more to eliminate $\mathbf{v}$ and obtain a result that is identical to (91) without variable depth, nonlinearities and ad-hoc terms.

Compared to the standard formulation without the dispersion term, third order derivatives of η have appeared. In some numerical methods this, combined with nonlinear terms, may lead to an increased sensitivity with respect to noise production. Extra caution is also needed for application of boundary conditions. We observe that also the Boussinesq equations in section A.1 correspondingly display higher order derivatives in the equation of continuity. In addition, this formulation involves third order derivatives of the depth. On the other hand, when higher order numerical schemes are applied higher order differences is bound to show up anyhow. Hence, it is quite open which version of the improved Boussinesq equations that is favourable from a numerical point of view. However, the improved standard formulation is somewhat simpler. We note that (91) still inherits errors of order $\mu^2\epsilon$, that are not present in (81).

A.4 Potential formulations with improved dispersion properties

Staying with a mild-slope approximation the formulation of [4] corresponds to

$$G_1 = \left(\frac{1}{2}z_\alpha^2 + z_\alpha h\right)\nabla^2\frac{\partial\phi}{\partial t}, \tag{94}$$

$$G_2 = -h\left(\frac{1}{6}h^2 - \frac{1}{2}(z_\alpha+h)^2\right)\nabla^3\phi, \tag{95}$$

where ϕ now is the value of the potential at vertical location z_α. With these dispersion terms we reproduce (82). The cost is the appearance of a fourth derivative of the potential in the continuity equation.

An alternative is to stick with the depth averaged potential and rewrite the dispersion term G_1 by means of $\partial\phi/\partial t + \eta = O(\mu^2, \epsilon)$:

$$G_1 = \gamma h^2 \nabla^2 \eta - (\frac{1}{3} - \gamma) h^2 \nabla^2 \frac{\partial \phi}{\partial t}, \quad G_2 = 0. \tag{96}$$

Here γ has the same role as in (91).

One might be tempted to combine the potential at z_α with a modification like (96) of the dispersion term of the momentum equation. The dispersion relation would then take on the form

$$c^2 = h \frac{1 - \alpha\mu^2 h^2 k^2 + \kappa \mu^4 h^4 k^4}{1 + \beta \mu^2 h^2 k^2}, \tag{97}$$

where we still have $\alpha = \frac{1}{3} - \beta$. Unfortunately, (97) is an unsound expression. If $\kappa < 0$ the numerator becomes negative for large k with resulting instability. On the other hand, if $\kappa > 0$ $c \to \infty$ as $k \to \infty$ which is another undesirable property.

A.5 Shallow water equations

Deletion of all $O(\mu^2)$ terms simplifies (80,81) to the NLSW equations. The pressure gradient in the momentum equation then becomes $\nabla\eta$, corresponding to hydrostatic pressure. As a consequence the horizontal velocity becomes independent of z. The NLSW equations lack the important effect of wave dispersion and may lead to erroneous results for long term propagation, even if the waves are long compared to the depth[38]. However, they are still a quite reasonable option for surf zone dynamics and are, by far, the most commonly used framework for runup calculations, as well as tsunami and storm surge models.

If the NLSW equations are linearized to yield the LSW equations, we may eliminate the velocity to obtain the standard wave equation

$$\eta_{tt} - \nabla \cdot (h \nabla \eta) = 0. \tag{98}$$

References

[1] M. B. Abott, H. M. Petersen, and O. Skovgaard. On the numerical modelling of short waves in shallow water. *J. Hyd. Res.*, 16(3):173–203, 1978.

[2] S. Beji and K. Nadaoka. A formal derivation and numerical modelling of the improved boussinesq equations for varying depth. *Ocean Engng*, 23:691–704, 1996.

[3] X. Cai, G. Pedersen, and H. P. Langtangen. A parallel multi-subdomain strategy for solving the Boussinesq water wave equations. *Advances in Water Resources*, 28(3):215–233, 2005.

[4] Y. Chen and P. L.-F. Liu. Modified Boussinesq equations and associated parabolic models for water wave propagation. *J. Fluid Mech.*, 288:351–381, 1995.

[5] Cornell University Web page by Phil L.-F. Liu.
URL: *http://ceeserver.cee.cornell.edu/pll%2Dgroup/tsunamis.htm.*

[6] Wei G., Kirby J. T., Grilli S. T., and Subramanya R. A fully nonlinear boussinesq model for surface waves. part 1. highly nonlinear unsteady waves. *J. Fluid Mech.*, 294:71–92, 1995.

[7] G. Gisler, R Weaver, and Gittings M. Sage calculations of the tsunami threat from La Palma. *Sci. Tsunami Hazards*, 24:288–301, 2006.

[8] B. Gjevik, G. Pedersen, E. Dybesland, C. B. C. Harbitz, P. M. A. Miranda, M. A. Baptista, L. Mendes-Victor, P. Heinrich, R. Roche, and M. Guesmia. Modeling tsunamis from earthquake sources near Gorringe Bank southwest of Portugal. *J. Geophys. Res.*, 102(C13):927–949, 1997.

[9] S. Glimsdal, G. Pedersen, and H. P. Langtangen. An investigation of domain decomposition methods for one-dimensional dispersive long wave equations. *Advances in Water Resources*, 27(11):1111–1133, 2005.

[10] S.-H. Hsiao, P. L.-F. Liu, and Y. Chen. Nonlinear water waves propagating over a permeable bed. *Phil. Trans. R. Soc. Lond. A*, 458:1291–1322, 2002.

[11] F. Imamura. Review of tsunami simulation with a finite difference method. In H. Yeh, C. E. Synolakis, and P. L.-F. Liu, editors, *Long-wave runup models*, pages 25–42. World Scientific Publishing Co., 1996.

[12] F. Imamura. *Simulation of wave-packet propagation along sloping beach by TUNAMI-code*, pages 231–241. Long-wave runup models. World Scientific, 1996.

[13] A. Jensen, G. Pedersen, and D. J. Wood. An experimental study of wave run-up at a steep beach. *J. Fluid. Mech.*, 486:161–188, 2003.

[14] A. B. Kennedy, Q. Chen, J. T. Kirby, and R. A. Dalrymple. Boussinesq modeling of wave transformation, breaking, and run-up. Part I: 1D. *J. Waterw., Port, Coast., Ocean Engrg.*, 126(1):39–47, 2000.

[15] J. T. Kirby. Funwave software download page, 1998.
URL: *http://chinacat.coastal.udel.edu.*

[16] J. T. Kirby, G. Wei, , Q. Chen, A. B. Kennedy, and R. A. Dalrymple. Fully nonlinear Boussinesq wave model documentation and user's manual. Research Report CACR-98-06, Center for applied Coastal research, Department of Civil Engineering, University of Delaware, Newark, DE 19716, September 1998.
URL: *http://chinacat.coastal.udel.edu.*

[17] H. P. Langtangen and G. Pedersen. Computational models for weakly dispersive nonlinear water waves. *Comp. Meth. Appl. Mech. Engrg.*, 160:337–358, 1998.

[18] H. P. Langtangen and G. Pedersen. Propagation of large destructive waves. *International Journal of Applied Mechanics and Engineering*, 7(1):187–204, 2002.

[19] D. K. Lilly. Numerical solutions for the shape-preserving two-dimensional thermal convection element. *J. Atmospheric Sciences*, 21:83–98, 1964.

[20] P. J. Lynett and P. L.-F. Liu. Coulwave model page, 2004.
URL: *http://ceprofs.tamu.edu/plynett/COULWAVE/default.htm.*

[21] P. J. Lynett, T.-R. Wu, and P. L.-F. Liu. Modeling wave runup with depth-integrated equations. *Coast. Eng.*, 46:89–107, 2002.

[22] P. A. Madsen and H. A. Schäffer. A review of Boussinesq-type equations for surface gravity waves. volume 5 of *Advances in Coastal and Ocean Engineering*, pages 1–95. World Scientific Publishing Co., Singapore, 1999.

[23] O. Nwogu. Alternative form of Boussinesq equations for nearshore wave propagation. *J. Waterw., Port, Coast., Ocean Engrg.*, 119(6):618–638, 1993.

[24] G. Pedersen. World Scientific Publishing.

[25] G. Pedersen. On the effects of irregular boundaries in finite difference models. *Int. J. Num. Meth. Fluids*, 6:497–505, 1986.

[26] G. Pedersen. On the numerical solution of the Boussinesq equations. Preprint series in applied mathematics, Dept. of Mathematics, University of Oslo, 1988.

[27] G. Pedersen. Three-dimensional wave patterns generated by moving disturbances at transcritical speeds. *J. Fluid Mech.*, 196:39–63, 1988.

[28] G. Pedersen. Finite difference representations of nonlinear waves. *Int. Journal num. meth. in fluids*, 13:671–690, 1991.

[29] G. Pedersen. Nonlinear modulations of solitary waves. *J. Fluid Mech.*, 267(83-108), 1994.

[30] G. Pedersen. Grid effects on tsunamis in nearshore regions. Preprint Series in Applied Mathematics, ISBN 82-553-0952-7 1, Dept. of Mathematics, University of Oslo, March 1995.

[31] G. Pedersen. Refraction of solitons and wave jumps. In B. Gjevik, J. Grue, and J. E. Weber, editors, *Waves and Nonlinear Processes in Hydrodynamics.*, pages 139–150. Kluwer Academic Publishers., 1996.

[32] G. Pedersen. Energy conservation and physical optics for discrete long wave equations. *Wave Motion*, 37:81–100, 2003.

[33] G. Pedersen. Variable depth and the validity of Boussinesq-type models. Preprint Series in Applied Mathematics In preparation, Dept. of Mathematics, University of Oslo, Norway, 2005.

[34] G. Pedersen and B. Gjevik. Run-up of solitary waves. *J. Fluid Mech.*, 135:283–299, 1983.

[35] G. Pedersen and H. P. Langtangen. An analytical approach to tsunami modeling. In B. Massinon and P. Heinrich, editors, *International Conference on Tsunamis; Paris 1998*, pages 342–353. CEA/UNESCO., 1999.

[36] G. Pedersen and O. B. Rygg. Numerical solution of the three dimensional Boussinesq equations for dispersive surface waves. Preprint series in applied mathematics, Dept. of Mathematics, University of Oslo, 1987.

[37] D. H. Peregrine. Long waves on a beach. *J. Fluid Mech.*, 77:417–431, 1967.

[38] D. H. Peregrine. Equations for water waves and the approximation behind them. In R. E. Meyer, editor, *Waves on beaches*, pages 357–412. Academic Press, New York, 1972.

[39] O. B. Rygg. Nonlinear refraction-diffraction of surface waves in intermediate and shallow water. *Coastal Engineering*, 12:191–211, 1988.

[40] F. Shi, R. A. Dalrymple, J. T. Kirby, Q. Chen, and A. Kennedy. A fully nonlinear boussinesq model in generalized curvilinear coordinates. *Coastal Engineering*, 42:337–358, 2001.

[41] F. Løvholt and G. Pedersen. Instabilities of Boussinesq models in non-uniform depth. 2007. Submitted.

[42] F. Løvholt, G. Pedersen, and G. Gisler. Modeling of a potential landslide generated tsunami at la palma island. 2007. Submitted.

[43] S. N. Ward. Landslide tsunami. *J. Geophys. Res.*, 6:11,201–11,215, 2001.

[44] T. Y. Wu. Long waves in ocean and coastal waters. *Proc. ASCE, J. Eng. Mech. Div.*, 107:501–522, 1981.

[45] S. B. Yoon. Propagation of distant tsunamis over slowly varying topography. *Journal of Geophysical Research-Oceans*, 107, 2002.

[46] S. B. Yoon, C. H. Lim, and J. Choi. Dispersion-correction finite difference model for simulation of transoceanic tsunamis. *Terr. Atmos. Ocean Sci.*, 18(1):31–53, 2007.

[47] J.A. Zelt and F. Raichlen. A Lagrangian model for wave-induced harbour oscillations. *J. Fluid Mech.*, 213:203–225, 1990.